Preparation and Characterization of Structurally Stable Polycrystalline $La_{0.7}Ca_{0.3}MnO_3$ and $La_{0.7}Ca_{0.3}(Mn_{(1-x)}Fe_x)O_3$ Samples

BY

JERRY J. BROWER

A thesis submitted in partial fulfillment of the requirements of Kingston University for the Degree of Doctor of Philosophy

KINGSTON UNIVERSITY
GRAND VALLEY STATE UNIVERSITY

NOVEMBER 2006

Preparation and Characterization of Structurally Stable Polycrystalline $La_{0.7}Ca_{0.3}MnO_3$ and $La_{0.7}Ca_{0.3}(Mn_{(1-x)}Fe_x)O_3$ Samples

Abstract

A new procedure in the preparation of polycrystalline, structurally sound, doped manganites was developed. This method is called "flashing." Using the new preparation technique, several batches of samples of $La_{0.7}Ca_{0.3}MnO_3$ and $La_{0.7}Ca_{0.3}(Mn_{(1-x)}Fe_x)O_3$ (with x = 0.05 and 0.07) were produced under different pelletizing pressures and annealing conditions.

In the case of the Ca doped manganites, electrical resistivity as a function of temperature measurements, with and without an applied magnetic field of 350 mT, show a negative magnetoresistive effect, and a practically field-independent metal-insulator transition that depends upon heat treatment and annealing conditions. Similar measurements in Ca and Fe doped manganites reveal the same behavior with relatively large resistivity values and lower transition temperatures that depend on Fe concentration.

Maximal values for electrical resistivity in Fe doped samples are at least one order of magnitude higher compared to the maximal values for Ca doped specimens. X-ray diffraction, electrical resistivity, and electron-microscope analyses indicate a correlation between grain size, annealing environment, conductivity, and magneto-resistance. Magnetic susceptibility measurements indicate that the metal-insulator transition occurs approximately at the Curie temperature in all the cases studied.

Table of Contents

Acknowledgements

In February of 1997, when I was seeking an institution through which I could pursue the Ph.D. degree, Dean Douglas Kindschi of the Science and Mathematics Division of Grand Valley State University (Allendale and Grand Rapids, Michigan, U.S.A.) informed me of our university's association with Kingston University and recommended that I make my inquires there. My first contact with Kingston University was with Dr. David Briers who greeted me most cordially and relieved my apprehensions about embarking on such an endeavor at my stage of life (50+ years). I wish to thank Dean Kindschi and Dr. Briers for providing the direction and encouragement to begin my association with Kingston University.

Navigating the administrative matters was made so much easier with the ready advice and assistance of Matthew Stephens, Diana Watts and especially, Kay Ballard who was always there with a rapid response to my very many questions. To these fine people who keep the machinery operating, I give a very sincere thanks.

Prof. Peter Foot's agreeable, mature and perspicacious nature was a steady hand throughout the past eight years of my work through Kingston University. Prof. Foot's sense of humor and comfortable demeanor carry through his e-mail and I thank him for his help and many enjoyable communications.

Mr. Bill Edwards did an incredible amount of work with the samples that I sent to him for analysis. One of my most memorable, enjoyable and educational experiences at Kingston University was the day that I spent working with Mr. Edwards. The products of his labors are quite simply the finest examples of a master craftsman. A very many thanks to 'Bill' for his efforts on my behalf.

Director of Studies is the title Dr. Vincent Montgomery has on my official paperwork, but 'Vincent's' work with me went well beyond his official duties. Our on-site visits were a recreation. Dr. Montgomery's help with computer issues and his knowledge of the mechanical processes with the equipment in the research lab enabled me to focus the direction, methods and course of my research. Every step of the way, our e-mail communications constantly kept the research on track and solved innumerable problems as they arose. A 'thank you' only begins to express my gratitude for Dr. Montgomery's exceptional guidance.

Nearly every single day for the past eight years, Dr. Javier Estrada has been not only my on-site advisor, but friend and colleague as well. Countless hours were spent over the past eight years, working through every single detail of my research. Every session of laboratory work, every bit of data and every word of this thesis has been a cooperative effort with Dr. Estrada. Words cannot express my gratitude for his tireless efforts and I will continue to show my thanks to Javier for all he has done for me.

Dr. Javier Estrada, Dr. Vincent Montgomery and Prof. Peter Foot have been with me through some unanticipated and very difficult times during my work on this project. I must give them a special thanks for their consideration, kindness and understanding during those times.

To all the fine people with whom I have had contact regarding my research project, and throughout my association with Kingston University, I thank you all, very much.

Jerry J. Brower

Chapter 1 Introduction

1.1 Introduction

Many centuries ago, electrostatic and magnetostatic effects were observed by ordinary people from several different cultures. Since the 16th century, electric and magnetic phenomena were systematically studied by William Gilbert (1540 – 1603), Stephen Gray (1666 – 1736), Charles Dufay (1698 – 1739), Benjamin Franklin (1706 – 1790), Charles Augustin Coulomb (1726 – 1806), Michael Faraday (1791 – 1867), and many other scientists.[1]

Today, we know that when a conducting material is placed within an electric field, electric charges in that material will be forced to move in the same general direction of the field. The electric charges crossing an infinitesimal cross-sectional area, perpendicular to the direction of the electric field per unit time per unit area, is defined as the electric current density **j**. This current density depends upon the type of material, the strength of the electric field, and the number of charge carriers available per unit volume.

The characteristics of a material that inhibit the transport of charge carriers within the material is generally referred to as the material's electrical resistivity (ρ). The inverse of ρ is the electrical conductivity (σ). Materials exhibiting large electrical resistivity are called insulators and those with small resistivity are called conductors.

In general, a magnetic field will alter the characteristics of a material in such a way that the material's resistivity will decrease, causing an increase in charge transport by the electric field. This phenomenon is known as magnetoresistance and was first

observed by William Thomson (Lord Kelvin) in 1857. Kelvin noticed that, independent of the type of material and the strength of the applied field, the decrease in electrical resistance was relatively small (no more than 5%).[2]

In this research project, using our experience in the preparation and characterization of a well known "high temperature" superconductor ($Y_1Ba_2Cu_3O_{7-\delta}$), an improved method for the preparation of structurally sound colossal magnetoresistive manganite samples of $La_{0.7}Ca_{0.3}MnO_3$, with different average grain sizes, was developed. The effect of air vs. oxygen annealing in the preparation of the samples was also examined. A second objective of this investigation was to study the effect of the strong magnetic moment ion Fe^{+3}, and the grain size in the magnetoresistance of an iron doped manganite ($La_{0.7}Ca_{0.3}$ $(Mn_{(1-x)}Fe_x)O_3$), when subjected to a "weak" magnetic field of the order of 500 mT. All the prepared samples were characterized by x-ray diffraction, electron-microscopy, electrical resistivity measurements and, in some cases, magnetic susceptibility. Our final objective was to interpret the experimental results in the light of the accepted explanations for colossal magnetoresistance (CMR) in manganites.

1.2 Historical Overview - Superconductivity

In 1908, Kamerlingh Onnes, working at the university of Leyden, was able to liquefy helium. The boiling point of He at atmospheric pressure is 4.2 K. This new research tool allowed him to study the conductivity of metals at very low temperatures. It was postulated at that time that the resistivity of a metal decreases linearly with decreasing temperature until it reaches a finite value called residual resistivity.[3]

This finite value was assumed to depend on the purity of the metal. In 1911, Kamerlingh Onnes, experimenting with mercury - then the purest available element - found a very sharp drop in its resistance at about 4.2 K. Below this temperature value, the resistance of Hg is practically zero. Onnes called this almost sudden disappearance of electrical resistance, superconductivity. A year later, he discovered that a strong enough applied magnetic field destroyed superconductivity. The plot by Kamerlingh Onnes of electrical resistance versus absolute temperature is shown below (fig. 1-1).

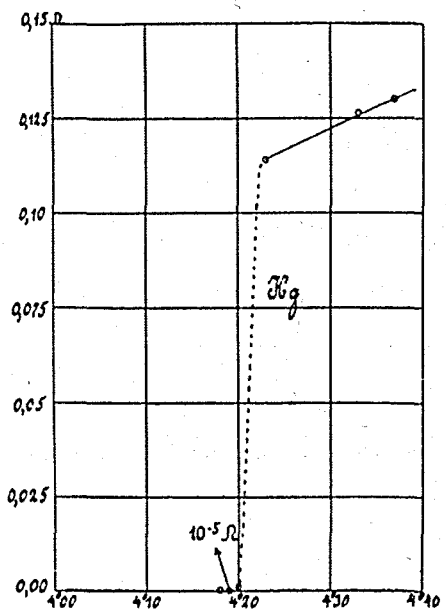

Figure 1-1. Resistance in ohms of a specimen of mercury versus absolute temperature, by Kamerlingh Onnes (photocopy of original).[4]

For the discovery of superconductivity and liquefying helium, Onnes received the 1913 Nobel Prize in Physics.[5] After the discovery of superconductivity in mercury, this phenomenon was observed at different transition temperatures in other elements

and in some alloys. In other words, above a critical temperature (T_c), a normal resistive state (normal state) is observed; below certain transition temperature T_c, super-conductivity is achieved (superconducting state).

In 1933 Walther Meissner and Robert Ochsenfeld found that when superconductors in their normal state were cooled below their critical temperatures, in the presence of a magnetic field, the magnetic field was expelled from their interior. This phenomenon is called the Meissner Effect and illustrates the perfect diamagnetic nature of the superconducting state.[6] Thus, superconductivity is characterized by zero electrical resistance and diamagnetic behavior.

Soon after this discovery, the London brothers proposed a phenomenological equation to describe the Meissner effect.[5] The so-called London equation is based on a postulate that modifies ohm's law for the normal state of a metal ($\mathbf{j} = \sigma\mathbf{E}$). According to this postulate, for a simply connected (in the topological sense) material (in the superconducting state, the current density **j** is directly proportional to the magnetic vector potential **A**, as expressed in the SI system, by the equation

$$\mathbf{j} = -\left(\frac{1}{\mu_0 \lambda_L^2}\right)\mathbf{A} \qquad (1.1)$$

where μ_0 is the permeability of free space and λ_L is a constant with units of length that depends on the particular type of superconductor. This equation is known as the London equation, and uses the Coulomb gauge $\nabla \cdot \mathbf{A} = 0$.

The following shows how equation 1.1 predicts the Meissner effect. The curl of **j** is given by

$$\nabla \mathrm{x}\, \mathbf{j} = -\left(\frac{1}{\mu_0 \lambda_L^2}\right) \nabla \mathrm{x}\, \mathbf{A} = -\left(\frac{1}{\mu_0 \lambda_L^2}\right) \mathbf{B} \qquad (1.2)^*$$

According to one of Maxwell's equations for the static case, $\nabla \mathrm{x}\, \mathbf{B} = \mu_0 \mathbf{j}$ (Ampère's law). From these equations, it follows that the curl of $\nabla \mathrm{x}\, \mathbf{B}$ is given by:

$$\nabla \mathrm{x}\, (\nabla \mathrm{x}\, \mathbf{B}) = \nabla(\nabla \cdot \mathbf{B}) - \nabla^2 \mathbf{B} = \mu_0 \nabla \mathrm{x}\, \mathbf{j} = -\left(\frac{1}{\lambda_L^2}\right) \mathbf{B} \qquad (1.3)$$

Since in classical electrodynamic theory magnetic monopoles do not exist, $\nabla \cdot \mathbf{B} = 0$. Thus, equation 1.3 is reduced to

$$\nabla^2 \mathbf{B} = \left(\frac{1}{\lambda_L^2}\right) \mathbf{B} \qquad (1.4)$$

Except for the trivial solution $\mathbf{B} = 0$, this equation does not allow a uniform field inside a bulk superconductor. For example, in the case of a semi-infinite superconductor on the positive side of the x-axis, a solution to eq. 1.4 is

$$\mathbf{B}(x) = \mathbf{B}(0)\, e^{-\left(\frac{x}{\lambda_L}\right)} \qquad (1.5)$$

Therefore, an applied magnetic field parallel to the superconductor boundary decreases exponentially inside the superconductor. Except for this exponentially decaying penetration of the magnetic field, **B** inside the superconductor is zero. This is the Meissner effect. The constant λ_L is known as the London penetration depth.[4]

*Although vectors **B** and **H** are normally called the magnetic flux density and the magnetic field intensity, respectively, in this thesis we will represent an external magnetic field by **B**, and the macroscopic magnetic field intensity in the presence of matter by **H** (see Appendix B in Solid State Physics by J. R. Hook, and H. E. Hall [1]).

The first microscopic theory of superconductivity was proposed in 1957 by John Bardeen, Leon Cooper, and Robert Schrieffer, and is known as the "BCS" theory. A simplified conceptual description of this theory is based on the coupling of pairs of electrons with a lower energy than two individual electrons, called Cooper pairs, after Leon Cooper who showed how interaction between electrons can lead to the formation of electron pairs composed of opposite momenta and spin.[7]

Imagine an electron drifting in a metal at T = 0 K (no lattice vibrations). This electron produces a momentary and local perturbation of the crystal. After the electron has passed by, the crystal not only returns to its original state, but oscillates around its rest position. A phonon is created. This phonon or lattice vibration affects a second conduction electron lowering its energy. The second electron creates a phonon that interacts with the first electron and so on. This passing back and forth of phonons couples the two electrons together and brings them into a lower energy state. These Cooper pairs move cooperatively through the crystal.

Thus, the scattering of electrons is eliminated and zero resistance is observed. The superconducting state is an ordered state of conduction electrons.[3] Not all materials can become superconductors and even with those that can, small thermal vibrations in the lattice will break up the electron pairing. This is why the superconducting phenomenon is only observed at very low temperatures where lattice vibrations are minimized.

Brian D. Josephson predicted in 1962, and it was later verified, the existence of a tunneling current between two superconductors separated by a thin insulating barrier, where the current is carried by these paired electrons (the Josephson effect).[8]

By 1986 Georg Bednorz and Karl Müller found superconductivity in an oxide of lanthanum, barium and copper at a temperature of 30 Kelvin and began what is now called the era of high-temperature superconductivity. More recently, higher critical temperatures have been reached. For example, a transition temperature of 125 K was achieved in $Tl_2Ba_2Ca_2Cu_3O_{10}$ by Stuart S. Parkin and coworkers.[9]

During the 20th century, and parallel to the study of superconductivity, several scientists were interested in magnetoresistance. A few years after the discovery of "high temperature superconductivity" in 1986, colossal magnetoresistance (CMR) was observed in a manganite. Several high temperature superconductors and manganites have similar crystalline structures based on a cubic lattice called perovskite.

1.3 Historical Overview - Magnetoresistance

The first report on the electric and magnetic properties of a manganite was published in 1950 by Harry Jonker and J.H. van Santen.[10,11] They observed a transition from a paramagnetic insulating to a ferromagnetic conducting phase, below room temperature, in $La_{1-x}Ca_xMnO_3$ for x values between 0.2 and 0.4. It was soon after this report when Clarence Zener, Junjuri Kanamori, John Goodenough and other scientists proposed the fundamental theory used today to explain the magnetoresistive behavior of manganites.[12] In 1969, Allen Morrish, Clark Searle and co-workers at the University of Manitoba measured magnetoresistance effects in a single crystal of $La_{0.69}Pb_{0.31}MnO_3$.[11]

In 1988 Albert Fert in France and Peter Grünberg in Germany, independently, discovered that alternating layers (1 to a few nanometers) of copper and cobalt or iron

and chromium produced increases in resistance of more than 50% after a magnetic field was applied and then removed. This effect was called Giant Magneto-Resistance (GMR).[13]

In 1993 there were reports from Siemens in Germany and Bell Labs in New Jersey, that certain manganese oxides showed a huge change in resistivity when a magnetic field was applied. The effect in these materials—the manganese perovskites—was so large in comparison to GMR, that it was called Colossal magneto-resistance (CMR).[14]

The work done by Von Helmolt and his group in 1994 found a large drop in electrical resistivity in a thin film of the mixed valence manganite $La_{0.67}Ba_{0.33}MnO_3$ near its para-ferromagnetic transition temperature. Based on this work, Jin, et al observed an even greater resistivity drop in a bulk polycrystalline sample of $La_{0.60}Y_{0.07}Ca_{0.33}MnO_3$.[15]

Some of the new and exciting ideas in the application of CMR in electronic devices take advantage of the ability of manganites to change their electrical resistance when exposed to magnetic fields. Stronger signals, smaller, faster, and less expensive sensors for magnetic fields, non-volatile memory systems and isolation mechanisms are expected to come from the development of CMR devices. CMR devices could be compatible with integrated CMOS (ICs) and made part of the circuitry and read-heads for hard disk drives that would produce larger signals and smaller storage bits.[13] The prospects of integrating CMR devices promises reduced size, lower manufacturing costs, greater efficiency and stimulates research to understand this new frontier.

1.4 Objective of this Research Project

A common problem for researchers using pelletized samples of $La_{0.7}Ca_{0.3}MnO_3$, is the disintegration of the material within a few days. The disintegration of the sample clearly indicates rapid changes in structure and brings into question the validity of data acquired from the samples. Long-term structural stability is absolutely necessary and therefore the first objective of this research project was to develop an improved method for the preparation of structurally sound samples of $La_{0.7}Ca_{0.3}MnO_3$. This was accomplished by modifying the techniques, and using the experience acquired in the preparation and characterization of high temperature superconductors ($Y_1Ba_2Cu_3O_{7-\delta}$).

The development of the process for producing structurally sound pellet samples reveals changes in the grain size from heat treatment, and density changes due to varying pelletizing forces used to form the pellets. This research investigates their effects on the magneto-resistive characteristics of the manganite samples.

Since the ionic radii of Fe^{+3} and Mn^{+3} are almost identical, it is possible to bypass lattice effects in the partial substitution of Mn by Fe. Previous experiments in this kind of doping show that there is practically no appreciable change in the lattice parameters of the crystalline structures of $La_{0.7}Ca_{0.3}MnO_3$, and $La_{0.7}Ca_{0.3}$ $(Mn_{(1-x)}Fe_x)$ O_3, up to $x = 0.12$.[16] Also, the insulator-metallic transition is lost if more than 10% of the Mn is substituted by Fe. Therefore, an objective of this research is to study the effect of the strong magnetic moment ion Fe^{+3} on the magnetoresistance of $La_{0.7}Ca_{0.3}$ $(Mn_{(1-x)}Fe_x)O_3$, when a "weak" magnetic field of the order of 400 mT is applied.

It is well known that the oxygen content in some high T_c superconductors is critical to obtain high transition temperatures. This research project investigates the effects that air and oxygen annealing have on the magnetoresistive properties of the doped manganite samples prepared using the newly developed pellet preparation methods.

Chapters 5 and 6 address each of the aforementioned considerations in detail. Finally, using the data acquired in these investigations, the experimental results are interpreted and compared with the currently accepted explanations for Colossal Magneto Resistance (CMR).

References

1. Sheldon L. Glashow, From Alchemy to Quarks, Brooks/Cole Publishing Company, Inc., 1994.

2. Neil Mathur, and Rhian-Marie Thomas, New Scientist, May 2, 1998.

3. Rolf E. Hummel, Electronic Properties of Materials, Springer-Verlag, 1985.

4. Charles Kittel, Introduction to Solid State Physics, John Wiley & Sons, Inc., seventh edition, 1996.

5. C. P. Poole, T. Datta, and H. A. Farach, Copper Oxide Superconductors, John Wiley & Sons, 1998.

6. C. A. Rose-Innes, and E. H. Rhoderick, Introduction to Superconductivity, Pergamon International Library, second edition, 1978.

7. B.S. Chandrasekhar, Why Things Are The Way They Are, Cambridge University Press, 1998.

8. Tinkham, Physics Today, 22 – 23, March 1986.

9. F. J. Adrian, and D. O. Cowan, C&EN, 24 – 41, December 21, 1992.J.

10. G. H. Jonker, J. H. van Santen, Physica **16**, 337 (1950); J. H. van Santen, G. H. Jonker, Physica **16**, 599 (1950).

11. N. Mathur, and P. Littlewood, Physics Today, 25 – 30, January 2003.

12. C. Zener, Phys. Rev. **81**, 440 (1951).

13. J. Daughton, and Jerry Granley, The Industrial Physicist, 22 – 24, June 1999.

14. S.-H. Jin, T. H. Tiefel, M. Mccormack, R. A. Fastnacht, R. Ramesh, L. H. Chen, Science **264**, 413 (1994).

15. M. R. Ibarra, and J. M. De Teresa, Journal of Magnetism and Magnetic Materials, 177 – 181 (1998) 846 – 849.

16. J. R. Sun, J. H. Rao, B. G. Shen, and H. K. Wong, Appl. Phys. Lett. **73**, 2998, 1998.

Chapter 2 General Characteristics of Manganites

2.1 Introduction

This chapter presents the current working theory of CMR in manganite crystal structures as summarized from a survey of the literature. A description of the magnetic properties of solids is convenient for understanding the following sections and is, therefore, presented first.

2.2 Magnetic Properties of Solids

According to Faraday's law, in any material, an applied magnetic field that changes with time induces an electromotive force (emf) that accelerates electrons in the material. The direction of the resulting current is such that it opposes the change in the field (Lenz's law). This phenomenon is known as diamagnetism.

In a material in which some of the atoms possess a permanent magnetic dipole moment, the applied magnetic field produces a torque that tries to align the magnetic moments in the direction of the field. This is called paramagnetism, and is normally stronger than the diamagnetic effect. The strength of the magnetic effect on the material is quantified by the magnetic susceptibility χ defined by equation 2.1, where **M** represents the magnetic moment per unit volume, and **H** is the macroscopic magnetic field intensity within the specimen.

$$\mathbf{M} = \chi \mathbf{H} \tag{2.1}$$

In the International System (SI), the units for both magnetization (**M**) and magnetic field intensity (**H**) are Am^{-1}. Therefore, the magnetic susceptivity (χ) is unitless.

The magnetic susceptibility is negative, very small, and nearly temperature independent for diamagnetic materials. It is positive, temperature dependent, and also small for paramagnets. For example, χ of ice has a typical value of -8.1×10^{-6}, and χ of $CuSO_4$ at room temperature is 3.8×10^{-4}.[1] Alternative definitions of magnetization, frequently used, refer to magnetic moment per unit mass or per mole. The corresponding SI units are Am^2kg^{-1} and Am^2mol^{-1}, respectively.

In order to describe a solid from the magnetic point of view it is necessary to specify the strength and the direction of the magnetic moment at each lattice site. Magnetic dipole moments arise in atoms because of the orbital and the spin angular momenta of the electrons. The theory used in this chapter is a quasi-classical approach to magnetism and the magnetic properties of materials. Some of these concepts are discussed in the paragraphs below.

2.2.1 Energy and Space Quantization

An understanding of the properties of a one-electron atom is very helpful in analyzing many-electron atoms. The quantization of energy of hydrogen-like atoms (hydrogen and its two isotopes deuterium and tritium, singly ionized helium, doubly ionized lithium, etc.) appears naturally as a solution to the time independent Schrödinger equation with a coulomb potential energy for the nucleus-electron system. In a first approximation calculation, the nucleus is considered as a point charge at rest at the origin of an inertial frame of reference. The possible energies for the bound states of the electron are given by equation 2.2.

$$E_n = - \frac{m_e e^4 Z^2}{8\varepsilon_0^2 h^2 n^2} = - \frac{2.180 \times 10^{-18} Z^2}{n^2} \quad J \qquad (2.2)$$

In this equation n is a positive integer (n = 1, 2, 3, 4, ...), m_e is the rest mass of the electron, e is the magnitude of its electric charge, Z is the atomic number of the atom (the number of protons in the nucleus), ε_0 is the permittivity constant of free space, and h is Planck's constant. This equation is normally written in terms of electron-volts instead of joules (equation 2.3). [2]

$$E_n = - \frac{13.607\, Z^2}{n^2} \quad eV \qquad (2.3)$$

By considering the electron-nucleus pair as a binary system and their motion around their common center of mass, a correction to the previous equations can be obtained. In this case, the reduced mass of the electron- nucleus system μ ($\mu = \frac{m_e M}{m_e + M}$, where M represents the mass of the nucleus) should replace m_e in equation 2.2. Since $m_e << M$, μ is approximately equal to m_e and this correction is small even for the H atom. Also, it is possible to introduce a relativistic correction, important only in the case of large values of Z and small values of n.[2]

In quantum mechanics, as in classical mechanics, a particle moving under a central force has an angular momentum that is a constant of motion. Experimental and theoretical considerations show that the angular momentum **l** of a bound electron is quantized and its magnitude is given by

$$l^2 = l(l+1)\hbar^2 \qquad (2.4)$$

where l = 0, 1, 2, ..., n-1, and $\hbar$ is Planck's constant divided by 2π.

For each value of the quantum number n, specifying an energy level, there are n distinct values of angular momentum. Customarily, the different values of l (0, 1, 2,....) are labeled by the letters s, p, d, f, g, h, ..., respectively. In addition to the quantization of the magnitude of the angular momentum, its direction is restricted. This directional restriction is known as space quantization. It means that, with respect to a given direction (normally a z-axis), **l** makes only certain angles such that its z-component l_z is quantized and given by

$$l_z = m_l \hbar \tag{2.5}$$

where $m_l = 0, \pm1, \pm2, \pm3, \ldots\ldots, \pm l$. See figure 2.1.

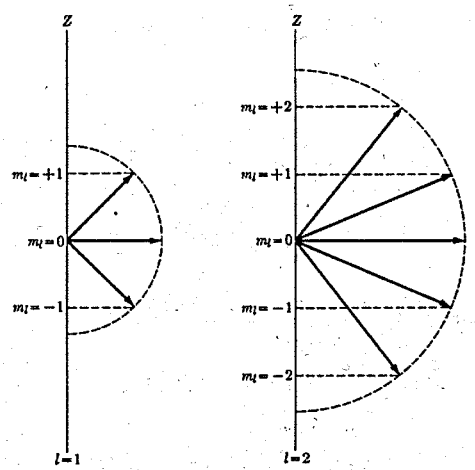

Figure 2.1 Illustration of space quantization for the cases $l = 1$ and $l = 2$. (Adapted from M. Alonso, and E. Finn, University Physics, volume III – Quantum and Statistical Physics).[2]

In quantum mechanics we can only know the magnitude of the angular momentum and one of its components, and our knowledge of the other two components is limited by the uncertainty relation

$$\Delta l_x \, \Delta l_y \geq \tfrac{1}{2} \hbar \, l_z \tag{2.6}$$

Thus, it is impossible to precisely determine the direction of the angular momentum **l**.

When relativistic corrections are omitted, each energy state of a hydrogen-like atom corresponding to a particular value of the quantum number n, contains n angular momentum states, all with the same energy (eq. 2.3). These states are labeled ns, np, nd, nf, etc.

If a first order relativistic correction is introduced, the allowed energy values are

$$E = E_n + \Delta E \tag{2.7}$$

where ΔE depends on the values of the quantum numbers n and l, and is given by

$$\Delta E = \left(\frac{|E_n| Z^2\alpha^2}{n}\right)\left(\frac{3}{4n} - \frac{1}{l+½}\right) \tag{2.8}$$

In this equation, α is called the fine structure constant and its value is

$$\alpha = \frac{e^2}{4\pi\varepsilon_0\hbar c} = \frac{1}{137} \tag{2.9}$$

where c is the speed of light in vacuum. Equations 2.7 and 2.8 show how energy levels with the same value of n, but different value of *l*, do not have exactly the same energy E.

Space quantization is evident in experiments like the Zeeman Effect. In this experiment, when a sufficiently strong magnetic field is applied to one-electron atoms, each energy level splits into $2l+1$ sublevels. The spacings between these sublevels are the same for all atoms and energy levels, and depends only on the strength of the applied magnetic field.

2.2.2 The Magnetic moment of an Atom

There is a correlation between the electronic structure of the atom and its magnetic moment. The magnetic moment of an atom depends upon the orbital motion of the electron and its spin angular momentum. First, the orbital magnetic dipole moment of the electron will be discussed.

A flat current-carrying loop produces a magnetic field similar to the one produced by a bar magnet. Thus, like a bar magnet, a current-carrying loop is said to be a magnetic dipole. [3]

If the electric current in a flat loop is i and its vector area is **A** (a vector perpendicular to the loop such that its magnitude is equal to the area of the loop, and directed so that the current is seen moving clockwise when looking along the direction of the vector), the magnetic dipole moment $\boldsymbol{\mu}$ associated with the current in a flat loop, is defined by equation 2.10.

$$\boldsymbol{\mu} = i\mathbf{A} \tag{2.10}$$

A bound electron in its motion around the nucleus produces a magnetic field just as a current in a loop does. Thus, there is an orbital magnetic dipole moment associated with a bound electron that can be expressed in terms of its angular momentum **l**. An expression for the orbital magnetic dipole moment of the electron $\mathbf{M}_l$, valid in quantum mechanics, is traditionally obtained using classical mechanics and assuming that the electron is in a circular orbit. In this case, the orbital motion of the electron corresponds to a small current, given in terms of the period T of the orbit, by

$$i = \frac{e}{T} = \frac{ev}{2\pi r} \tag{2.11}$$

Then, the magnitude of $\mathbf{M}_l$ is

$$M_l = iA = \tfrac{1}{2}\, evr \qquad (2.12)$$

where e is the magnitude of the electronic charge, v its speed, and r the radius of the assumed circular orbit. Since the angular momentum of the electron ($\mathbf{l} = \mathbf{r} \times m_e\mathbf{v}$) has a magnitude $l = rm_ev$, and the electric charge of the electron is negative, the vector form of equation 2.12 can be written in terms of $\mathbf{l}$ as

$$\mathbf{M}_l = -\tfrac{1}{2}\,\frac{e\mathbf{l}}{m_e} \qquad (2.13)$$

These vectors are represented in figure 2.2.

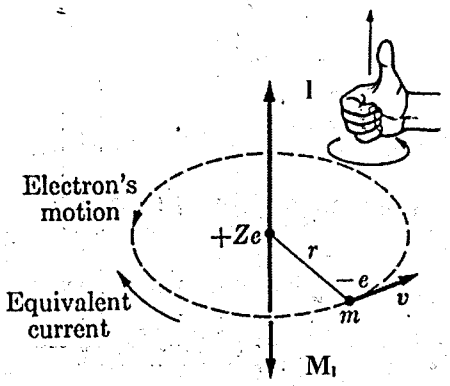

Figure 2.2. Representation of the orbital angular momentum $\mathbf{l}$ and the corresponding orbital magnetic dipole moment $\mathbf{M}_l$ of a bound atomic electron. (Adapted from M. Alonso, and E. Finn, University Physics, volume III – Quantum and Statistical Physics).[2]

The z-component of $\mathbf{M}_l$ (M_{lz}) is also quantized and given by equation 2.14

$$M_{lz} = -\tfrac{1}{2}\left(\frac{el_z}{m_e}\right) = -\left(\frac{e\hbar}{2m_e}\right)m_l = -\mu_B\, m_l \qquad (2.14)$$

where the quantity $\left(\dfrac{e\hbar}{2m_e}\right)$ is called the Bohr magneton μ_B, and its value is

$\mu_B = 9.2732 \times 10^{-24} JT^{-1}$. A one-electron atom placed in an external magnetic field * acquires an extra energy E_B and experiences a torque τ, given by equations 2.15 and 2.16, respectively.

$$E_B = - \mathbf{M_l} \cdot \mathbf{B} = \left(\frac{e}{2m_e}\right)\mathbf{l} \cdot \mathbf{B} = \left(\frac{e}{2m_e}\right) l_z B = \left(\frac{e\hbar}{2m_e}\right) m_l B = \mu_B m_l B \qquad (2.15)$$

$$\tau = \mathbf{M_l} \times \mathbf{B} = -\left(\frac{e}{2m_e}\right)\mathbf{l} \times \mathbf{B} \qquad (2.16)$$

Equation 2.15 illustrates how each energy level spits into equally spaced m_l levels, depending on the magnetic field.

Besides the orbital angular momentum of the electron, its spin also contributes to the magnetic moment of the atom. Free or bound electrons have an intrinsic angular momentum called spin (**s**). This is a quantum-mechanical property with no analog in classical mechanics. The idea of the electron spin was first proposed in 1926 by G. Uhlenbeck and S. Goudsmit to explain certain features of the spectrum of hydrogen like atoms.[2] The existence of the electron spin is supported by a large accumulation of experimental evidence. One of these experiments is the Stern-Gerlach experiment in which a beam of hydrogen-like atoms, in their ground state, splits into two beams when passed through a non-uniform magnetic field. Each beam corresponds to one of the two possible values of the spin (spin-up or spin-down). Because the electron is a charged particle, its spin angular momentum should produce an intrinsic or spin magnetic dipole moment $\mathbf{M_s}$. If we assume that the electron is a rotating charged body, the relationship

*Although the vectors **B** and **H** are normally called the magnetic flux density and the magnetic field intensity, respectively, in this thesis we will represent an external magnetic field by **B**, and the macroscopic magnetic field intensity in the presence of matter by **H** (see Appendix B in Solid State Physics by J. R. Hook, and H. E. Hall [1]).

between $\mathbf{M}_s$ and $\mathbf{s}$ should be the same as the one between $\mathbf{M}_l$ and $\mathbf{l}$, $\mathbf{M}_l = -\frac{1}{2}\frac{e\mathbf{l}}{m_e}$.

This is not the case. In agreement with experiments,

$$\mathbf{M}_s = -g_s(\tfrac{1}{2})\left(\frac{e}{m_e}\right)\mathbf{s} \tag{2.17}$$

where g_s is called the gyromagnetic ratio of the electron. Its experimental value is very close to 2 ($g_s = 2.0024$).[2]

The total angular momentum $\mathbf{j}$ of a bound electron is the sum of its orbital and spin angular momenta, i.e.

$$\mathbf{j} = \mathbf{l} + \mathbf{s} \tag{2.18}$$

and the corresponding total magnetic dipole moments is

$$\mathbf{M} = \mathbf{M}_l + \mathbf{M}_s = -\tfrac{1}{2}\left(\frac{e}{m_e}\right)(\mathbf{l} + g_s\mathbf{s}) \tag{2.19}$$

As with the orbital angular momentum, the spin orbital momentum is also quantized. The magnitude of $\mathbf{s}$ and its z-component are given by equations 2.20 and 2.21, respectively.

$$\mathbf{s}^2 = s(s+1)\hbar^2 \tag{2.20}$$

$$s_z = m_s\hbar \tag{2.21}$$

with $s = \tfrac{1}{2}$, and $m_s = \pm\tfrac{1}{2}$. The two possible orientations of $\mathbf{s}$ are shown in figure 2.3.

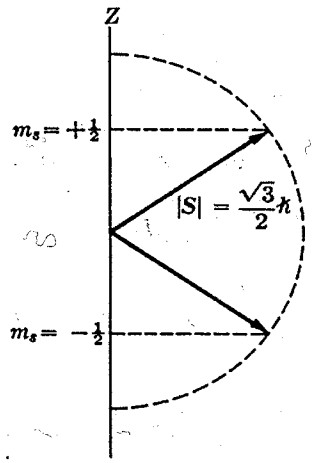

Figure 2.3. The two possible orientations of the spin angular momentum of the electron. (Adapted from M. Alonso, and E. Finn, University Physics, volume III – Quantum and Statistical Physics).[2]

Although **s** is never directed along the z-axis, its two possible orientations are called spin up ↑ and spin down ↓ .

2.2.3 Spin-Orbital Interaction

In a hydrogen-like atom, the motion of the positive nucleus relative to the electron creates a magnetic field **B** parallel to the orbital angular momentum **l** that interacts with the electron's spin magnetic moment $\mathbf{M}_s$. Since $\mathbf{M}_s$ is proportional to **s**, this interaction is proportional to the dot product $\mathbf{s} \cdot \mathbf{l}$ and is called the spin-orbit interaction. It is responsible for the separation of the energy levels in pairs called doublets (except in the case $\mathbf{l} = 0$ or "s-levels"). Indeed, the problem of explaining these doublets first gave rise to the idea of an electron spin with two possible orientations. The two yellow lines in the emission spectrum of sodium is a well known example.[2]

For atoms with more than one electron, in addition to the coulomb potential energy associated with each electron and the nucleus, it is necessary to include the

energies of the interactions between the electrons. In this case, an exact solution of the Schrödinger equation is impossible. The desire to understand the observed values of the quantized energy levels, the electronic configuration, the magnetic properties, and other characteristics of many-electron atoms is the origin of several fundamental ideas like Pauli's exclusion principle, Hund's rules and the L-S or Russell-Saunders coupling. These ideas will be discussed next.

The energy state of an atom depends on the orbital quantum numbers (n,*l*,and m_l) and the spin quantum number m_s. The distribution of atomic electrons among the allowed energy levels gives the electronic configuration of the atom. According to Pauli's exclusion principle no two electrons in an atom may have the same quantum numbers. In addition to many experimental facts, this principle explains the periodic physical and chemical behavior of the elements.[2]

The total angular momentum **J** of an atom, is the sum of the total orbital angular momentum **L** and the total spin angular momentum **S**. **L** is the vector sum of the angular momenta of the electrons ($\Sigma_i \mathbf{l}_i$), and **S** is the vector sum of all the spin angular momenta ($\Sigma_i \mathbf{s}_i$). Thus,

$$\mathbf{J} = \mathbf{L} + \mathbf{S} \tag{2.22}$$

Because of the possible different orientations of the orbital and spin angular momenta of the atomic electrons ($\mathbf{l}_i$ and $\mathbf{s}_i$, respectively) for a given electronic configuration, it is possible to have different values of the quantum number J associated with the total angular momentum **J**. Each value of J corresponds to a different energy of the atom. The total angular momentum of an atom determines its magnetic properties and the

probability of electronic transitions in radiative processes. One method to find the allowed values of J for a given atomic configuration is called the L-S or Russell – Saunders coupling after the two astronomers who first used it in the study of atomic spectra emitted by stars.[4]

In this scheme, the magnitude of J is given by the quantum number J according to the expression

$$\mathbf{J}^2 = J(J+1)\hbar^2 \tag{2.23}$$

The z-component of **J** is determined by the quantum number M according to

$$J_z = M\hbar \qquad \text{where } M = \pm J, \pm (J-1), \ldots\ldots \tag{2.24}$$

Similarly, quantum numbers associated with **L** and **S** (L, M_L, S, and M_S) are given by equations (2.25) and (2.26):

$$\mathbf{L}^2 = L(L+1)\hbar^2, \qquad L_z = M_L\hbar, \qquad M_L = \pm L, \pm (L-1), \ldots \tag{2.25}$$

$$\mathbf{S}^2 = S(S+1)\hbar^2, \qquad S_z = M_S\hbar, \qquad M_S = \pm S, \pm(S-1), \ldots. \tag{2.26}$$

Once the values of **L** and **S** are found, we can find the value of **J**. The possible values of the quantum number J are

$$J = L+S, L+S-1, \ldots\ldots, |L-S|. \tag{2.27}$$

The state of an atom is characterized by the quantum numbers L, S, and J. States with the same values of L and S but different values of J form a multiplet and have practically the same energy. The different values of J corresponding to a set of values L and S is called the multiplicity and is given by 2S+1. The spectroscopic notation uses symbols S, P, D, F, ….. , corresponding to the possible values of L (0, 1, 2, 3, 4, …), respectively. A superscript to the left of the symbol indicates the multiplicity and a subscript to the right indicates the value of J. For example, if the value of the total angular momentum L is 2, the corresponding spectroscopic notation is $^{2S+1}D_J$.

In the presence of an external magnetic field, each multiplet level splits into M_L levels. The spectroscopic notation for different interactions is illustrated in figure 2.4.

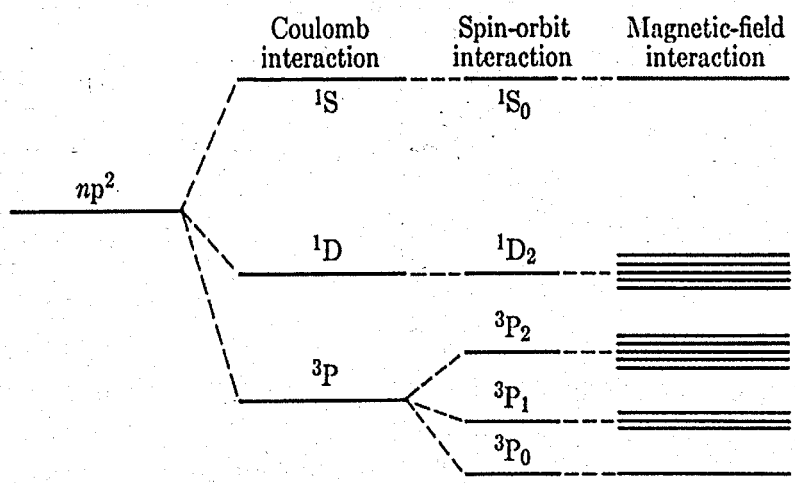

Figure 2.4. Energy levels of the np^2 configuration. (Adapted from M. Alonso, and E. Finn, University Physics, volume III – Quantum and Statistical Physics).[2]

Hund's rules are used to find the electronic configuration of an atom in its ground state. They give the values of L, S, and J for this lowest energy state. These rules, which must be followed in order, are:

1. S takes the maximum value allowed by Pauli's exclusion principle - as many as possible of the electrons must have parallel spins.
2. L takes the maximum value consistent with the value of S – the electrons have their orbital angular momenta as well aligned as possible.
3. For a shell* less than half full $J = |L-S|$, and for a shell more the half full J=L+S.[1]

If the shell is just half full, application of the second rule gives L = 0, so J = S.[5]
For example, the electronic configuration of Fe^{3+} is [Ar] $3d^5$, where [Ar] represent the electronic configuration of Argon. The five electrons occupy the 3d energy levels in such a way that:

1) $S = ½ + ½ + ½ + ½ + ½ = 5/2$,
2) $L = +2 + 1 + 0 - 1 - 2 = 0$, and
3) $J = L+S = S = 5/2$.

In this case the multiplicity is $2S+1 = (2 \times 5/2) + 1 = 6$ and the spectroscopic notation for the configuration of the ground state of Fe^{3+} is $^6S_{5/2}$. This configuration is illustrated in figure 2.5 on the following page.

*Energy gaps are observed between the allowed energy levels in atoms. These gaps occur between levels 1s and 2s, between 2p and 3s, 3p and 4s, etc. energy levels grouped between gaps are called shells.[2]

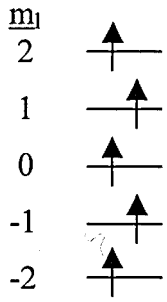

Figure 2.5 Representation of the spins of the 5 electrons in the 3d level for the electronic configuration of the ground state of Fe^{3+}.

2.2.4 Paramagnetism

As previously mentioned, paramagnetism is observed in materials in which some of the atoms possess permanent magnetic dipole moments. In the presence of an applied magnetic field these moments experience a torque that tends to align them in direction of the field. As the temperature decreases, this alignment is less and less affected by thermal motion. Therefore, paramagnetism is a temperature dependent property. The nucleus also has a magnetic dipole moment that is about 2,000 times smaller than the atomic magnetic dipole moment. Although magnetic effects resulting from nuclear magnetic dipole moments are important in some cases like NMR (nuclear magnetic resonance), these effects will not be considered here.

In terms of **L** and **S** the total magnetic dipole moment of an atom can be written

$$\boldsymbol{\mu} = -\tfrac{1}{2}\left(\frac{e}{m_e}\right)(\mathbf{L} + g_s\mathbf{S}) \qquad (2.28)$$

Closed shells of electrons in atoms do not contribute to the total orbital angular momentum or to the total spin angular momentum. Thus, only atoms with incomplete electronic shells have permanent dipole moments and contribute to paramagnetism.

Since transition metals have an incomplete 3d shell and rare earths an incomplete 4f shell, they are paramagnetic. The total magnetic dipole moment of the atom in the presence of an applied magnetic B field, normally assumed in the z-direction, acquires an extra energy E_B given by

$$E_B = -\boldsymbol{\mu} \cdot \mathbf{B} = -\mu_z B \tag{2.29}$$

The effect of the magnetic field on the ground state of an atom or an ion is to break the degeneracy associated with the 2J+1 different values of J_z. Quantum mechanical calculations of the expected values of E_B ($< E_B >$) give equally spaced energy levels

$$< E_B > = g\mu_B J_z B \tag{2.30}$$

where $J_z = -J, \ldots\ldots, -1, 0, +1, \ldots\ldots, J$, and g is the Landé g-factor given by

$$g = \left(\frac{3}{2}\right) - \left[\frac{L(L+1) - S(S+1)}{2J(J+1)}\right] \tag{2.31}$$

Comparison of the last two equations suggests an effective magnetic moment for the ion μ_{eff} such that

$$\mu_{eff} = -g\mu_B J \tag{2.32}[1]$$

Therefore, the Landé g-factor gives the number of Bohr magnetons associated with the effective magnetic dipole moment.

Assuming that the permanent dipole moments in a solid behave independently of each other, the relative occupation of the energy levels of eq. 2.30 is a function of temperature given by the Boltzmann factor

$$\exp\left(\frac{-E_B}{k_B T}\right) = \exp\left(\frac{-g\mu_B B J_z}{k_B T}\right) \tag{2.33}$$

where k_B is Boltzmann's constant. The contribution of one atom to the z-component of the magnetization is $-g\mu_B J_z$. For N magnetic moments per unit volume, the magnetization is

$$M = \frac{Ng^2\mu_B^2 J(J+1)B}{3k_B T} \tag{2.34}$$

In the following equations, B represents the local magnetic field at the ion -- the external magnetic field and the contributions from the magnetic moments of the neighboring ions.[1] For small magnetic fields the magnetization is a linear function of $\left(\frac{B}{T}\right)$ but approaches the saturation magnetization at large fields. The change in the function occurs when $\left(\frac{g\mu_B B}{k_B T}\right)$ is approximately 1 and we approach the maximum possible alignment of the dipoles with the field. Thus, the saturation magnetization is $Ng\mu_B J_z$.

The magnetic susceptibility χ was defined by equation 2.1. If χ is small, $\mu_0 M << B$ and the difference between the applied and the local fields as well as that between B and $\mu_0 H$ is unimportant. Therefore, from equations 2.1 and 2.34 it follows that

$$\chi = \frac{M}{H} = \frac{\mu_0 M}{B} = \frac{Ng^2\mu_B^2 J(J+1)\mu_0}{3k_B T} . \tag{2.35}$$

Because of a classical calculation by Langevin of the paramagnetic susceptibility of a paramagnetic ion of magnetic moment $p\mu_B$, the previous equation can be written in terms of p as

$$\chi = \frac{Np^2\mu_B^2\mu_0}{3k_B T} \tag{2.36}$$

where p corresponds to $g[J(J+1)]^{1/2}$ in equation 2.35. Equation 2.36 describes the **Curie law** for a paramagnet, i.e.,

$$\chi = \frac{C}{T} \tag{2.37}$$

with the Curie constant C given by

$$C = \frac{Np^2\mu_B^2\mu_0}{3k_B} \tag{2.38}$$

Curie's law is valid for localized magnetic moments that can be treated as distinguishable and obey Boltzmann's distribution. Another contribution to the paramagnetism of solids originates in the magnetic moments of conduction electrons. These moments are indistinguishable and because of Pauli's exclusion principle, the alignment of the moments in the presence of an applied magnetic field is hindered. Therefore, the value of the magnetic susceptibility of conduction electrons at a given temperature is lower than that given by Curie's law at that temperature.

In an applied magnetic field the energy of the electrons with spins parallel to the field is lower than the energy of anti-parallel spins. Assuming weak magnetic effects, the applied magnetic field B can be written as

$$B = \mu_0 H \tag{2.39}$$

and the calculated magnetic susceptibility for N conduction electrons per unit volume is

$$\chi_p = \frac{3N\mu_0\mu_B^2}{2\varepsilon_F} \tag{2.40}$$

with ε_F the Fermi energy (the highest energy of an electron at 0 K).[6] The contribution of the conduction electrons is called Pauli spin paramagnetism. This effect is very weak compared to effect of localized moments. The Pauli paramagnetic susceptibility χ_P is

actually on the order of magnitude of the diamagnetic susceptibility associated with conduction electrons $\chi_{dia}\left(\chi_p \cong \chi_{dia}\right)$. The net susceptibility of conduction electrons is positive and is equal to about $(2/3)\chi_p$ in approximate agreement with experimental values.[1] Although band structure effects and interactions between electrons affect the calculated values of χ_p, it gives the correct order of magnitude.

2.2.5 Diamagnetism

The source of diamagnetism, as shown classically by Langevin and in agreement with quantum mechanics, is the acceleration (or deceleration) that a changing applied magnetic field produces on the electrons orbiting the atomic nucleus. Detailed quantum-mechanical calculations show that the induced electric currents produced by the accelerated charges have certain stability and screen the interior of any material from the applied field. The induced magnetic moment on an isolated atom by an applied magnetic field is given by

$$\boldsymbol{\mu} = -\left(\frac{Ze^2}{4m}\right)\langle\rho^2\rangle\,\mathbf{B}, \tag{2.41}$$

where Z is the atomic number, e the magnitude of the charge of the electron, m its mass, **B** the applied magnetic field, and $\langle\rho^2\rangle$ is the mean square distance of the electrons from the z-axis (an axis through the nucleus in direction of **B**).[1]

Since the diamagnetic effect is weak, it is possible to ignore the effect on the field at the position of an atom induced by the magnetic moments of its neighbors. In this case we can assume $\mathbf{B} = \mu_0\mathbf{H}$. Thus, for N identical atoms per unit volume the

magnetization is

$$\mathbf{M} = N\,\boldsymbol{\mu} = -N\left(\frac{Ze^2}{4m}\right)\langle\rho^2\rangle\,\mu_0\mathbf{H}\,. \tag{2.42}$$

Finally, from the definition of magnetic susceptibility (equation 2.1) we have

$$\chi = \frac{M}{H} = \mu_0\frac{M}{B} = -N\left(\frac{Ze^2}{4m}\right)\mu_0\langle\rho^2\rangle. \tag{2.43}$$

This theoretical equation agrees well with experimental results.

Paramagnetic and diamagnetic effects coexist at the microscopic level. The dominant effect determines the type of magnetization (positive or negative) observed experimentally in a given specimen.

2.2.6 Magnetic Order

The behavior of paramagnetic materials was explained by assuming that the permanent magnetic dipole moments behave independently of one another. Even in the presence of an external magnetic field, no net magnetization is observed if the directions of the magnetic moments are completely randomized by thermal motion. For a given paramagnet, below a certain temperature, the interactions between the permanent magnetic dipole moments can no longer be ignored and spontaneous magnetization is observed in the absence of an external magnetic field. At this temperature, the material undergoes a phase transition from a disordered to a magnetic ordered state. The transition temperature varies widely from material to material. For example, it is 1,388 K for cobalt, and below 1 K for ionic salts with magnetic ions very separated.

When all the moments contribute equally to the spontaneous magnetization the magnetic order is called ferromagnetic. If half the dipoles are aligned in one direction and the other half in the opposite direction, no spontaneous magnetization is observed. This is the case of antiferromagnetic order. In some cases the cancellation of parallel and antiparallel magnetic moments is not perfect and a net magnetization remains. This type of behavior is called ferrimagnetism.

Before quantum mechanics, and in order to explain the ferromagnetic transition, P. Weiss suggested that the spontaneous magnetization of iron was due to the alignment of the atomic magnetic moments. He proposed the existence of a "molecular field" proportional to the magnetization and affecting any moment. The resulting effective magnetic field ($\mathbf{B}_{eff}$) can be written as

$$\mathbf{B}_{eff} = \mathbf{B}_{loc} + \lambda\mu_0\mathbf{M} \tag{2.44}$$

where $\mathbf{B}_{loc}$ is the magnetic field at the position of the atom and $\lambda\mu_0\mathbf{M}$ is the Weiss molecular field. λ is a dimensionless constant that determines the strength of the molecular field. [1, 7]

Detailed quantum-mechanical calculations using the idea of a molecular field give the following expression for the magnetic susceptibility

$$\chi = \frac{M}{H} = \frac{C}{(T - T_c)}. \tag{2.45}$$

This equation is a modified Curie law called the **Curie-Weiss law** and describes fairly well the behavior of ferromagnetic materials at high temperatures. C is the Curie constant, T_c is the curie temperature and represents the upper temperature at which

ferromagnetic order is observe. At $T = T_c$ the magnetic susceptibility diverges, and for temperatures below T_c ($T < T_c$) spontaneous magnetization occurs.

Néel generalized Weiss' idea of a "molecular field" to antiferromagnetic order, and divided the lattice of magnetic atoms into two sublattices A and B, with opposite orientations of the magnetic moments. The field produced by each sublattice affects the other one. In this case the magnetic susceptibility is given by the modified Curie law

$$\chi = \frac{M}{H} = \frac{C}{(T + T_N)}, \tag{2.46}$$

where C is the Curie constant and T_N, called the Néel temperature, represents the onset of antiferromagnetism. As shown by equation 2.46, the magnetic susceptibility is reduced below the Curie law value and remains finite at all temperatures.[1]

2.3 Literature Survey of Research on Manganites

CMR has been observed in doped manganites based on $LaMnO_3$, a perovskite type of structure. The general formula for these doped manganites is $RE_{1-x}AE_xMnO_3$, where RE stands for a trivalent rare-earth element such as La, Pr, Nd, Sm, Eu, Gd, Ho, Tb, Y, etc. or Bi^{3+}, and AE for a divalent alkaline earth ion as Sr, Ca, Ba, or Pb^{2+}.

The (RE, AE) site is normally called perovskite site-A, the Mn site is the B-site. See figure 2.6 on the following page (Adapted from Neil Mathur, and Peter Littlewood, Physics Today, January 2003, page 27).[8]

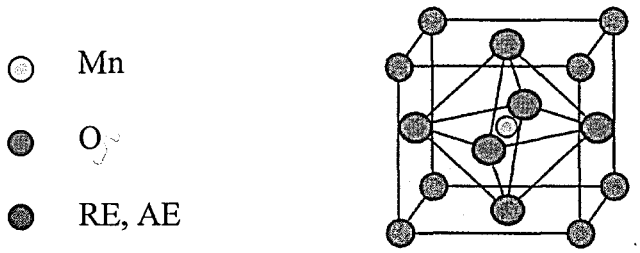

Figure 2.6 Perovskite structure of the Mn oxide or manganite. The Mn ion and its neighboring oxygen form the octahedron MnO_6 shown in the figure.

An interesting characteristic of the $RE_{1-x}AE_xMnO_3$ perovskite structure is its flexibility for chemical modification of the A-site or A-site doping. For example, in $La_{1-x}Ca_xMnO_3$ the solid state solution accepts values of x from 0 to 1. In the case of AE = Sr, x can have values up to 0.7 under normal preparation conditions, and up to 1.0 under high pressure.[9] In the manganite oxide $LaMnO_3$ the Mn ion has valence 3+. In the alkaline earth substituted perovskite type manganese oxides the Mn ion can have two oxidation states Mn^{3+} and Mn^{4+}. For example, if 10% of the La is substituted by Ca, then 90% of the Mn ions will be Mn^{3+} and the other 10% Mn^{4+}. The average Mn valence in this case will be 3(0.9) + 4(0.1) = 3.1. Therefore, in the case of $La_{0.7}Ca_{0.3}MnO_3$, the average Mn valence (AV) is AV = 3(0.7) + 4(0.3) = 3.3.

The behavior of an electron in a solid is governed by its charge, its spin, its orbital symmetry (the probability density of the electron cloud), and its interactions with other electrons and ions. Because of the flexibility of the perovskite structure to accept doping on the A-site, manganites are ideal for the study of strongly correlated electronic systems. They allow us to observe the competition between different effects like kinetic energy of mobile electrons, their Coulomb repulsion, the coupling between charge carriers and the lattice, etc.

The Mn^{3+} ion has 4 electrons in the outermost, five-fold degenerate, 3d energy level. The crystal field splits the five d orbitals into a t_{2g} triplet and an e_g doublet. Depending upon the type and the amount of doping, the separation between the triplet and the doublet is between 2 and 4 eV. These transition-metal 3d electrons experience a Coulomb repulsion that tends to localize them. This interaction competes with the hybridization with oxygen p electrons that tend to delocalize the 3d electrons. According to Hund's rule, in order to minimize electrostatic repulsions, the spins of these 4 electrons are up (lowest energy). Three of them are in a lower energy triplet state. The triplet has a total spin 3/2, and is called core spin $\mathbf{S_c}$. The three electrons in the triplet state are bound to the manganese ion - localized electrons. The remaining electron goes into a linear combination of e_g orbitals and the system further reduces its energy by splitting the doublet state into another 2 hyperfine sublevels, as shown in figure 2.7. This important effect in the manganites is called the Jahn -Teller effect.[10]

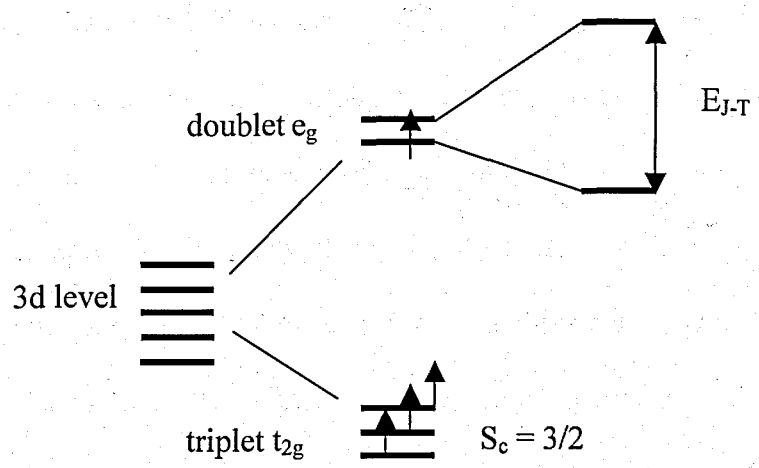

Figure 2.7 The 5-fold degenerate 3d energy level of Mn^{3+}, the triplet, the doublet, and the Jahn-Teller effect.

The e_g orbitals x^2-y^2 , and d $3z^2-r^2$ point toward O^{2-} ions. The t_{2g} orbital xy, yz, and zx point in between O^{2-} ions. Their shapes are illustrated in figure 2.8. (Adapted from N. Mathur, P. Littlewood, Physics Today, 25-30, July 2003).[8]

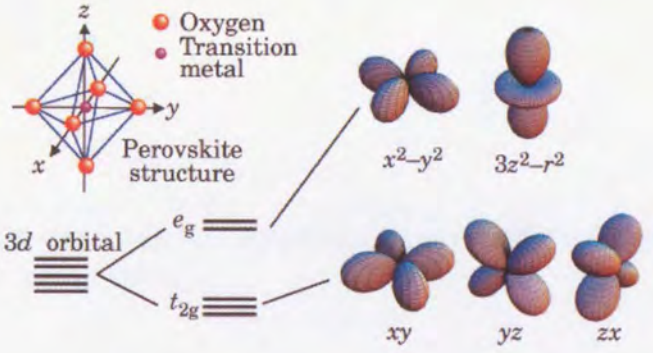

Figure 2.8 Octahedron formed by the transition metal and its oxygen nearest neighbors in the perovskite structure of $La_{1-x}Ca_xMnO_3$. The shapes of the orbitals of the Mn ion 3d electrons are also shown.

In the case of $La^{3+}Mn^{3+}(O^{2-})_3$, the electrons are not free to move (localized electrons) and the material is, at any temperature, an insulator. In $LaMnO_3$, due to a macroscopic lattice strain, the MnO_6 octahedra deforms, producing an elongation of the crystal in the xy plane, and a compression in the z direction, or an elongation in the z direction and a compression in the xy plane. These are the two linearly independent, even parity, volume preserving, Jahn-Teller modes that further remove the degeneracy of the doublet. Each type of Jahn-Teller mode favors the occupancy of one or the other of the two orbitals of the doublet. See figure 2.9 on the following page (Adapted from A. J. Mills, Nature, vol. 392, 12 March 1998).[10] In this figure, the Mn ions occupy the corners of the cube.

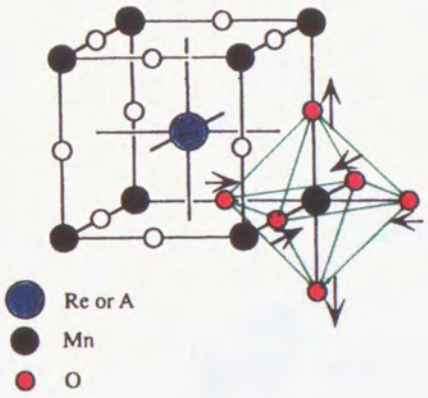

Figure 2.9 One of the two possible deformations of the MnO_6 octahedron or Jahn-Teller effect.

In $La^{3+}Mn^{3+}(O^{2-})_3$, local linear combinations of $3z^2$-r^2 and $3y^2$-r^2 orbitals produce stable states $3x^2$-r^2 and $3y^2$-r^2, alternating on the Mn sites in the xy-plane. Below about 140K, the spins of these electrons couple ferromagnetically in the xy plane and antiferromagnetically along the z-axis. The material is an antiferromagnet. This is illustrated in figure 2.10 on the following page (Adapted from N. Mathur, P. Littlewood, Physics Today, 25-30, July 2003).[8] Above this temperature there is no long-range magnetic ordering so we have a paramagnet. For certain hole doping concentrations, as in the case of Ca^{2+} or Sr^{2+}, some of the Mn^{3+} change into Mn^{4+} ions. Within the appropriate temperature range, the electrons move from Mn^{3+} to Mn^{4+} sites, and the solid shows metallic behavior. In the case of 100% Ca doping ($x = 1$), i.e., for samples of $Ca^{2+}Mn^{4+}(O^{2-})_3$, the charge density in the doublet state is zero and the compound is again an insulator.

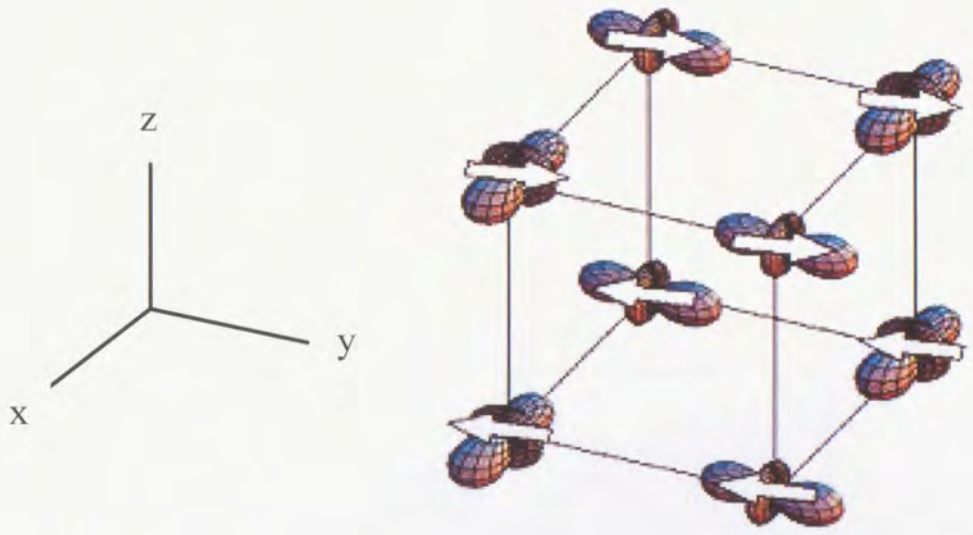

Figure 2.10 Spin and orbital coupling in the case of the Mott insulator $LaMnO_3$. Note that only the Mn sites are shown.

Perhaps the most interesting behavior of the doped manganite $La_{1-x}Ca_xMnO_3$ (LCMO) occurs for doping levels between 20 and 50% ($x = 0.2$ to $x = 0.5$). Within this doping range, as temperature decreases, LCMO undergoes a magnetic transition, at about the Curie temperature T_c, from a paramagnetic to a ferromagnetic phase. This transition is accompanied by an insulating-metallic transition near T_c. As the temperature decreases from room temperature, the system changes from a spin disordered to a spin ordered state. Since the scattering of charge carriers decreases with spin order, the values of electrical resistivity drop for temperatures below the transition T_c. For $0 < x < 0.2$, the system is an insulator at any temperature, and the magnetic order changes in a complicated way. Phases such as canted antiferromagnet (CAF) and ferromagnetic insulator (FI) are observed. Charge order (CO), a periodic pattern of Mn sites in different valence states, develops within the FI phase. When $x > 0.5$, LCMO is an antiferromagnet, and becomes charge ordered above certain temperatures. The

ground state is again insulating. This is clearly illustrated in figure 2.11, a phase diagram on the doping (x) temperature (T) plane for this compound.

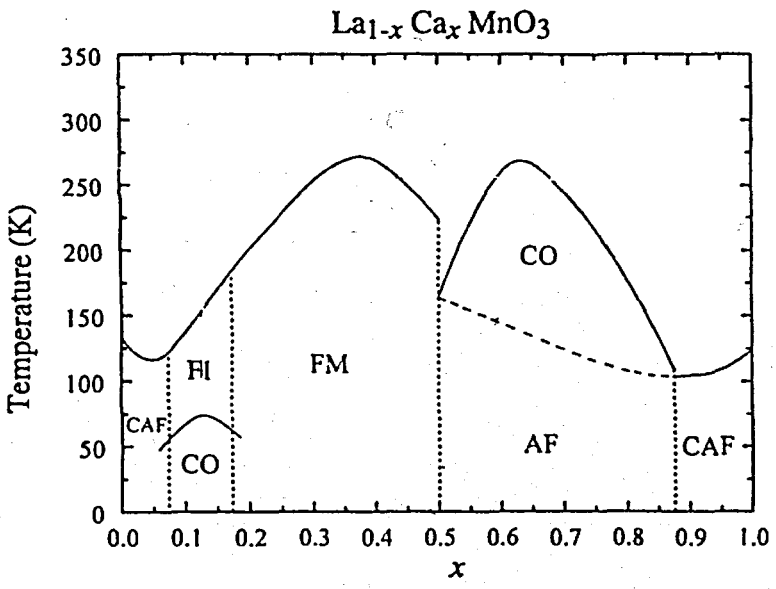

Figure 2.11 Phase diagram of $La_{1-x}Ca_xMnO_3$ on the doping (x) temperature (T) plane. (Adapted from A. J. Mills, Nature, vol. 392, 12 March 1998).[10]

Within the appropriate doping range, the application of an external magnetic field **H** aligns the spins of the charge carriers producing an additional decrease in electrical resistivity. This is the magnetoresistance effect (MR), normally defined by

$$MR = 100\% \left[\frac{\rho(H,T) - \rho(0,T)}{\rho(0,T)} \right] \tag{2.47}$$

where ρ (H,T) is the resistivity at a certain temperature T, measured in an applied field H, and ρ (0,T) the resistivity at temperature T, without field. MR is normally negative and, with applied fields of a few Tesla, near T_c, has a value of a few percent in the case of normal ferromagnetic materials, a few tens of percent for magnetic multilayers, and close to 50% in manganite perovskites (see figure 2.12).

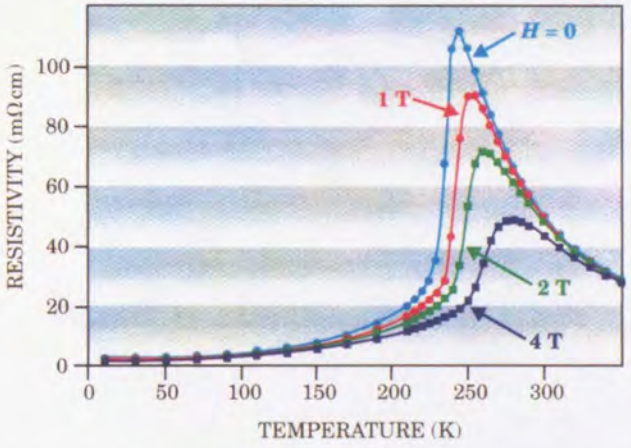

Figure 2.12 Electrical resistivity vs Temperature for $La_{1-x}Ca_xMnO_3$ under different magnetic fields. Adapted from P. Schiffer, A. P. Ramirez, W. Bao, S.-W. Cheong, Phys. Rev. Lett. 75, 3336, 1995.[11]

In order to understand the difference between electric conductivity in perovskites and normal ferromagnets, it is necessary to consider several important effects like electron-phonon coupling, ferromagnetic coupling, and spin polarization of charge carriers. The electrons in the highest energy levels of the Mn ions are shared with the O ions, forming an energy band whose width depends on the overlapping of the Mn and O orbitals. This overlapping depends on the geometry of the crystal lattice, and is maximum for an ideal perovskite in which the Mn-O-Mn bond is straight (the case of

regular MnO_6 octahedron with angle $\theta = 180°$). When a smaller ion such as Ca is substituted for a La ion, as in $La_{1-x}Ca_xMnO_3$, some of the Mn ions are displaced, and some of the Mn-O-Mn bonds bent ($\theta < 180°$), see figure 2.13.

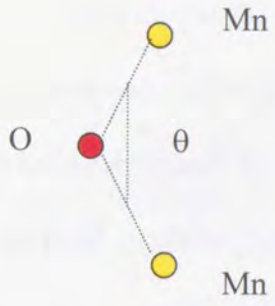

Figure 2.13 Mn-O-Mn bond, and angle θ.

Experiments by Sangwook, Cheong and colleagues at Bell Lab, and by Josep Fontcuberta and co-workers [12], working with samples of $La_{2/3-\delta}Y_\delta Ca_{1/3}MnO_3$, confirmed that as θ decreases from 180°, the orbital overlapping or equivalently the band width decreases, the ferromagnetic coupling becomes weaker, conductivity drops, and T_c is reduced.

Electron spin, as well as bandwidth, are involved in the movement of charge carriers. According to Hund's rule, the electron spin in the highest energy band should be aligned with the atomic magnetic moment due to the localized electrons (those electrons nearest the Mn sites). These localized electrons, sometimes called "fixed" electrons, give the sites their spins. The charge carriers can move more easily when the magnetic moments of neighboring ions are aligned. This increases the effective

bandwidth, reducing resistivity and exhibits a metallic behavior. This is often referred to as the double-exchange (DE) process.

The application of an external magnetic field would align the magnetic moments and widen the bandwidth. Magnetoresistance would be observed near the Curie temperature. In the calcium-doped materials, electron – phonon coupling competes with the double-exchange mechanism to inhibit the movement of charge carriers.

The calcium-doped manganese perovskite, above the Curie temperature, is paramagnetic and insulating. It has been found[8] that this calcium-doped material, when subjected to an external magnetic field, exhibits a much greater magnetoresistance effect than, for example, the metallic strontium-doped material.

Lattice vibrations, called phonons, affect the transport of charge carriers and this interference diminishes as the temperature approaches the Curie temperature. Vibrations of the oxygen ions (see figure 2.9) push electrons toward the vacant states of the manganese ion. This in turn, produces a local distortion of the lattice as mentioned earlier (see fig. 2-8). This distortion, or polaron, acts like an electron-trapping mechanism, restricting the movement of charge carriers and resulting in the insulating state, above the Curie temperature. As the temperature drops, the polarons disappear with a resulting increase in bandwidth and increased mobility of electrons.

It is interesting to note other findings that connect the bandwidth dependence to the electron-phonon coupling. Researchers at the Los Alamos National Laboratory and at Johns-Hopkins University have shown that the electron-phonon coupling is stronger for narrow-bandwidth materials and that the resulting self-trapping effect leads to higher resistivities.[8]

Also, neutron scattering experiments show that there exists small ferromagnetic regions well above the Curie temperature.[8] This would be expected since the polarons would confine spin-aligned electrons to particular locations in the crystal lattice and result in the observed small ferromagnetic regions or clusters in the normal paramagnetic phase. While it is still not well understood, this phase separation is a major focus in CMR research today (see figure 2.15, page 46).

2.4 Lattice Structure

The connective pattern of MnO_6 octahedra produces two types of lattice, a rhombohedral or an orthorhombic one. Such a lattice distortion is governed by a tolerance factor f. For a cubic perovskite f = 1, and the ratio between the two distances **a** and **b**, shown in figure 2.14 (darker lines), is

$$\frac{(r_A + r_O)}{(r_B + r_O)} = \sqrt{2} \tag{2.48}$$

where r_i represents the ionic radius of the ions at sites A, B or oxygen.

Thus, the deviation from f = 1, or definition of the tolerance factor is:

$$f = \frac{\text{distance } \mathbf{a}}{\sqrt{2}\ \text{distance } \mathbf{b}} = \frac{(r_A + r_O)}{\sqrt{2}(r_B + r_O)} \quad .^{13} \tag{2.49}$$

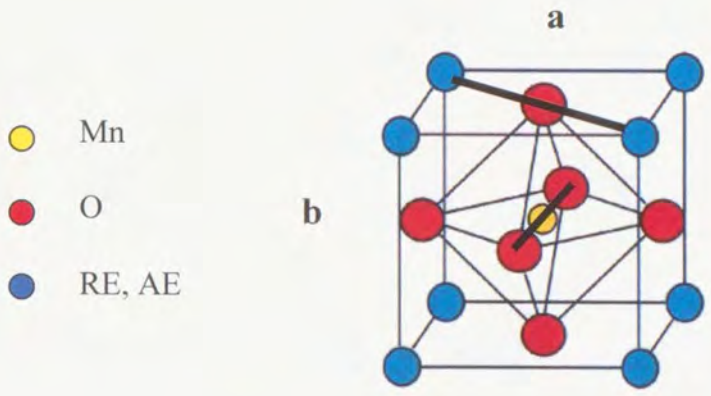

Figure 2.14 Assuming ions as rigid, touching spheres, the ratio between $(r_A + r_O)$ and $\sqrt{2}\,(r_B + r_O)$ defines the tolerance factor f.

As f decreases from 1 (smaller A-site ion), the lattice changes from rhombohedral to orthorhombic, i.e., if f has values between 1 and 0.96 the lattice is rhombohedral, and for $f < 0.96$ the lattice is orthorhombic. The angle θ (see figure 2.13, page 41) varies continuously as f decreases from 1.

2.5 Phase Coexistence in Manganites

Recently, atomic resolution experiments using scanning, tunneling, and magnetic force microscopy (TSM, TEM, MFM, respectively), and electron holography, revealed the coexistence, within a single crystal, of different electronic and magnetic phases.[14] There is evidence of magnetic, electronic, and crystal texture on mesoscopic length scale (tens or hundreds of nm). Today, this is the subject of many studies.[8]

Manganites are just one example of strongly correlated electronic systems in which the crystal, electronic and magnetic structures are tightly linked to one another.

Depending on the external conditions, the following three electronic phases can be distinguished: an electronic insulating solid or charge ordered insulating phase (COI), a poorly conducting electronic liquid with paramagnetic characteristics (PM), and a metallic electronic gas or ferromagnetic metallic phase (FMM).

At a given temperature and applied magnetic field, the phase stability depends on the competition between the delocalizing double exchange interaction (DE), and the localizing Jahn-Teller effect (JT). The DE exchange favors the motion of a valence electron between two adjacent Mn^{3+} and Mn^{4+} ions via the intervening O ion (delocalization). The J-T effect is a valence electron induced local distortion of the MnO_6 octahedron that tends to trap the electron (localization).

When the temperature is high, the spins are randomly oriented and the electron-lattice (electron-phonon) interaction or J-T effect is very strong. The localized valence electrons are in a poorly conducting phase, and the magnetic structure is paramagnetic (PM phase). As the temperature decreases, under a strong J-T effect and a weak DE interaction, antiferromagnetism is favored by a virtual exchange process called superexchange. The electronic system behaves as an insulating solid, and the charge ordered insulating phase (COI) is observed. At low temperatures, when the spins are aligned, the DE is enhanced and conductivity increases. Ferromagnetism is observed. This is the ferromagnetic metallic phase (FMM).

Depending upon valence electron concentration and temperature, other phases form. For example, as shown in figure 2.15 on the following page, a ferromagnetic charge ordered phase was detected in TEM and electron holography experiments.

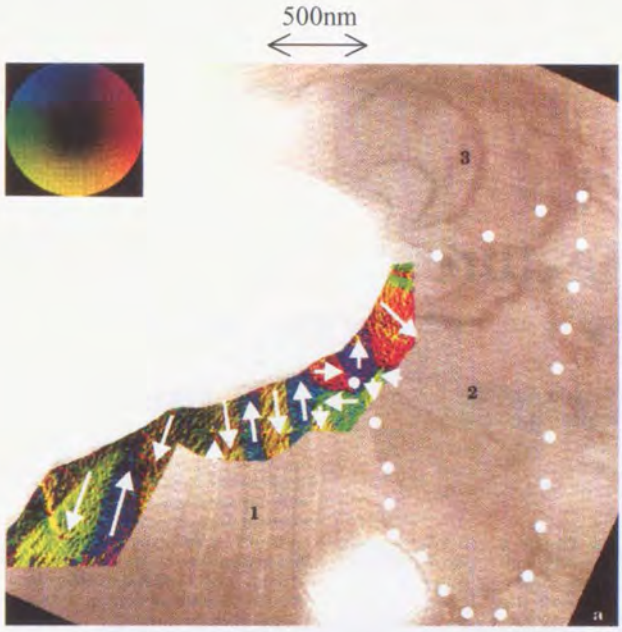

Figure 2.15 TEM and electron holography study of three adjacent grains in a polycrystalline sample of $La_{1/2}Ca_{1/2}MnO_3$ at 90K. The color wheel in the upper left of the figure is a direction indicator of magnetic moment (see color overlay and arrows). Grain 1 is ferromagnetic. In grain 2, an unexpected coexistence of ferro-magnetic domains with regions of strong charge order is observed. Grain 3 is charge ordered, but does not have a net magnetic moment. (Adapted from N. Mathur, and P. Littlewood, Physics Today, 25-30, January 2003).[8]

This Ferromagnetic charge-ordered phase was considered impossible because de-localization by DE interaction is required to produce ferromagnetism. This ferromagnetism is probably produced by hopping of charge carriers between nearest-neighbors ions rather than by DE interaction.[8]

The physical properties of manganites depend on the competition between the DE interaction and the J-T effect. A wide range of tuning parameters determines the outcome of this competition. Among them: chemical composition that affects the ratio between Mn^{3+} and Mn^{4+} ions, applied magnetic field, applied electric field, lattice strain, electromagnetic radiation, etc.

In summary, in divalent cation doped manganites, below a certain temperature, CMR occurs when a large applied magnetic field aligns the spins on the Mn sites and the valence electrons flow easily from one Mn ion to the next, through the intervening O ion. The colossal change in electrical resistivity is due to the highly insulating nature of the sample at high temperatures.

Phase coexistence is generally more likely to be observed in systems that exhibit first order phase transitions, i.e. discontinuous jumps in order and latent heat. This is the case of low temperature transitions between COI and FMM, and temperature-induced transitions between COI and PM. If the electron-lattice coupling is weak enough, the observed phase transitions are continuous (second order). This is, for example, the case of observed magnetic transitions from FMM to PM.[8]

2.6 The Role of Grain Boundaries in CMR of Manganites

In order to facilitate technological applications of CMR, it is necessary to find materials with an insulator to metal transition as close as possible to room temperature and with a strong enough MR characteristic in low magnetic fields (fields of the order of a few hundred milli-tesla).

It is well known that two independent processes contribute to the increase in magnetization of a ferromagnetic sample in an external magnetic field: i) In weak fields the volume of domains with magnetic moment parallel to the applied field grows at the expense of unfavorably oriented domains, and ii) Strong magnetic fields simply rotate the magnetization of domains.[5]

In trying to understand the mechanisms for CMR in doped manganites, many experiments have been done at low magnetic fields (LFMR), as well as at high magnetic fields (fields of the order of a few Tesla—HFMR). The samples used are monocrystalline or polycrystalline thin films or bulk polycrystalline materials. The type of thin film produced for MR studies depends on the relationship between the crystalline structures and lattice parameters of the substrate and the film deposited on it. Lattice parameters mismatch can produce structurally stressed single crystal or polycrystalline thin films. Grain size, interfaces and grain boundaries clearly affect LFMR in Mn perovskites.[15] Although the origin of LFMR is still unclear, two possible explanations have been proposed: i) A spin tunneling process across interfaces of grains separated by an energy barrier, related to the relative orientation of the magnetizations of the grains. ii) The spin dependent scattering at interfaces.[16] Josep Fontcuberta and his group at the "Universidad Autónoma de Barcelona" studied the effect of grain size and grain boundaries on MR of polycrystalline samples of $La_{0.67}Sr_{0.33}MnO_3$ at low and high magnetic fields.[15] They found that as the average grain size decreases, the value of electrical resistivity at any temperature increases, and that in the case of samples with grain size below 30 nm, a clear insulating behavior appears below 100 K. Samples with an average grain size larger than 30 nm exhibit metallic behavior all the way down from T_c. See figure 2.16 on the following page (adapted from Ll. Balcells, J. Fontcuberta, B. Martinez, and X. Obradors, Phy. Rev. B, **55**, number 22, December.1998-II).

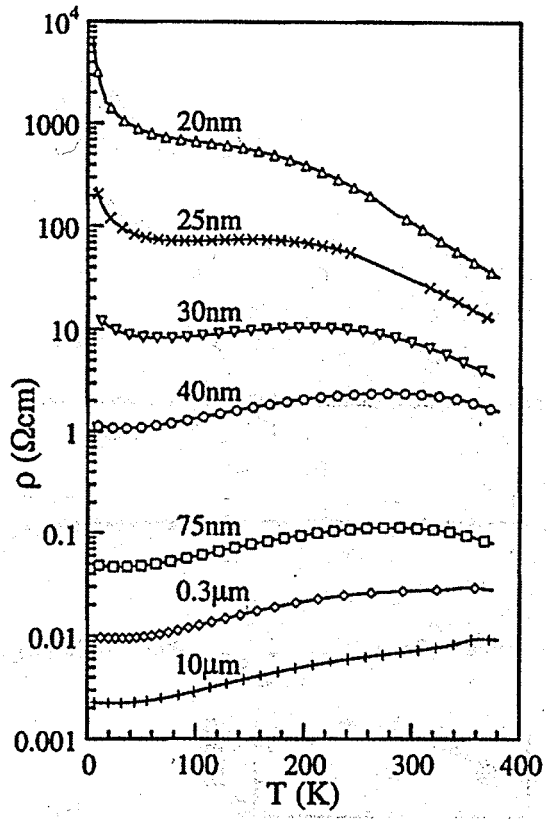

Figure 2.16 Temperature dependence of the zero field resistivity for samples of different grain sizes.[15]

The analysis of these HFMR experiments shows that as the average grain diameter d decreases, the HFMR effect increases. This suggests the existence of a surface layer, possibly of non-ferromagnetic nature, of thickness t that increases as d decreases. The thickness t is directly related to the intergranular resistance and the height of the energy barrier that the conduction electrons must cross or tunnel. On the other hand, LFMR investigation reveals that as d decreases, MR increases up to a grain size limit of about 0.5 μm diameter. Below this grain size, no further increase in MR is observed.

References

1. J. R. Hook, and H. E. Hall, Solid State Physics, 2nd ed., John Wiley & Sons, 1991.

2. M. Alonso, and E. Finn, University Physics, volume III – Quantum and Statistical Physics – Addison-Wesley, 1968.

3. D.Halliday, R. Resnick, and J Walker, Fundamentals of Physics, 7th ed., John Wiley & Sons, 2005.

4. R. Eisberg, and R. Resnick, Quantum Physics, 2nd ed., John Wiley & Sons, 1985.

5. C. Kittel, Introduction to Solid State Physics, 7th ed., John Wiley & Sons, 1996.

6. R. E. Hummel, Electronic Properties of Materials, Springer-Verlag, 1985.

7. N. W. Ashcroft, and N. D. Mermin, Solid State Physics, Saunders College Publishing, 1976.

8. N. Mathur, P. Littlewood, Physics Today, 25-30, January 2003.

9. Y. Tokura, Y. Tomioka, Journal of Magnetism ad Magnetic Materials, 200 1-23 (1999).

10. A. J. Mills, Nature, vol. 392, 12 March 1998.

11. P. Schiffer, A. P. Ramirez, W. Bao, S.-W. Cheong, Phys. Rev. Lett. 75, 3336, 1995.

12. J. Fontcuberta, Physics World, 33-38, February 1999.

13. J. B. Goodnough, J. M. London, in: K.-H. Hellwege, O. Madelung (Eds.), Magnetic and Other Properties of Oxides and Related Compounds, Landolt-Bornstein, New Series, Group III, vol. 4, Pt. A Springer, Berlin, 1970.

14. J. C. Loudon, N. D. Mathur, P. A. Midgley, Nature 420, 792, 2002.

15. Ll. Balcells, J. Fontcuberta, B. Martinez, and X. Obradors, Phy. Rev. B, 55, number 22 December,1998-II.

16. X. W. Li, A. Gupta, G. Xiao, and G. Q. Gong, Appl. Phys. Lett. 71, 1124, 1997.

Chapter 3 Experimental Techniques and Equipment

3.1 Introduction

The basic equipment used by researchers for investigation into super-conductivity is essentially the same used to make measurements of CMR in manganate materials. Voltage, current, pressure and temperature measurements as well as a vacuum system and cryogenic system for sample temperature reduction vary only in brand name and precision of measurements. The same measurement equipment and sample producing techniques are used for characterizing the magneto-resistive properties of samples such as the polycrystalline doped manganites. This chapter reviews the equipment, processes and procedures used for the investigations of this research project.

3.2 Techniques and Equipment

A standard, generally accepted technique was used in the preparation of samples, which included a typical solid-state reaction of high purity oxides or carbonates of the elements involved. These compounds were ground to a fine powder using an agate mortar and pestle. This mixture was placed in a high temperature alumina crucible and sintered at a high enough temperature to react the chemicals and achieve the desired crystalline structure. To ensure a complete reaction, the process of re-grinding and sintering was repeated several times.

For the sintering process, a Thermolyne programmable high temperature muffle furnace, type 46100 was used (figure 3-1). This furnace permits sintering temperatures up to 1700°C.

Fig. 3-1 Thermolyne High Temperature Furnace

The chamber section of this furnace is heated by six Super Kanthal 33 heating elements suspended within the chamber that is made of alumina and silica high temperature refractory fiber (figure 3-2).

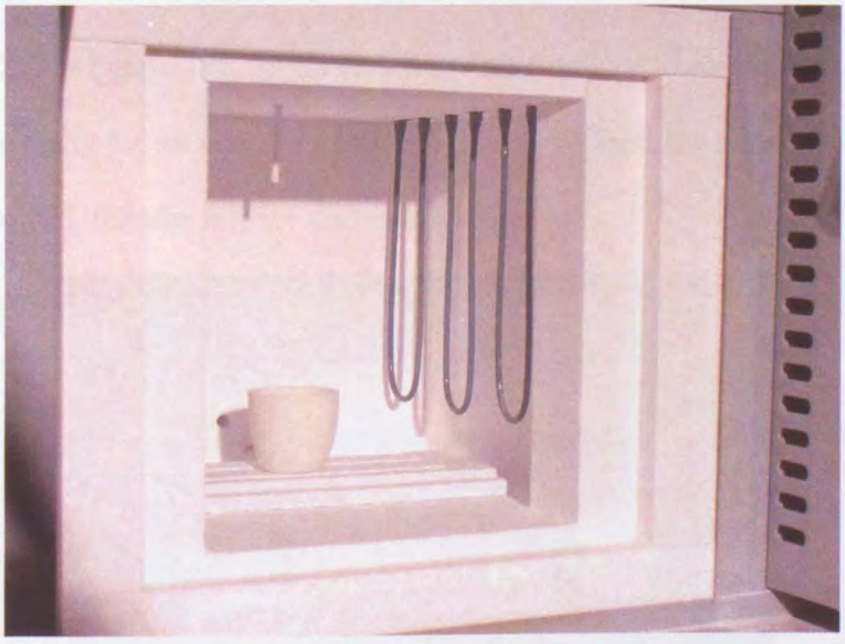

Fig. 3-2 Chamber of furnace showing U-shaped heating elements and thermocouple (small vertical rod above crucible).

A precious metal type B thermocouple senses the temperature in the chamber and transmits this information to the temperature controller (figure 3-2).[1] Since the furnace is programmable, it enables the operator to program up to 8 ramp segments (heat-up or cool-down rate) and 8 dwell segments (soak) for applications that require time and temperature relationship.

A typical program would be:

(PR1)-STEP This starts the furnace heating rapidly (about 20 minutes) from room temperature to
(PL1)-1180°C the desired sintering temperature level for

(PD1)-14 hrs the desired dwell time at that temperature. After this,

(PR2)-STEP steps the furnace back down (about 4 hours) to room temperature.
(PD1)-END Ends the program.

(PR1=program ramp #1, PL1=program level #1, PD1=program dwell #1)

After the last sintering, the material was again ground to a fine powder. Using a standard laboratory piston die and hydraulic press, the powder was pelletized with a pressure of 6.7×10^7 Pascals, into disks 13mm in diameter and 2-3mm thick. The pellets were then ready for the annealing process. For the annealing process, a Thermolyne type F21100 tube furnace was used (figure 3-3).

Figure 3-3 Thermolyne Tube Furnace with ceramic boat inserted at left end of tube.

The sample to be annealed was placed in a ceramic boat. The boat was then placed inside a quartz-glass tube (figure 3-4) which was then positioned so that tube and boat were midway into the oven.

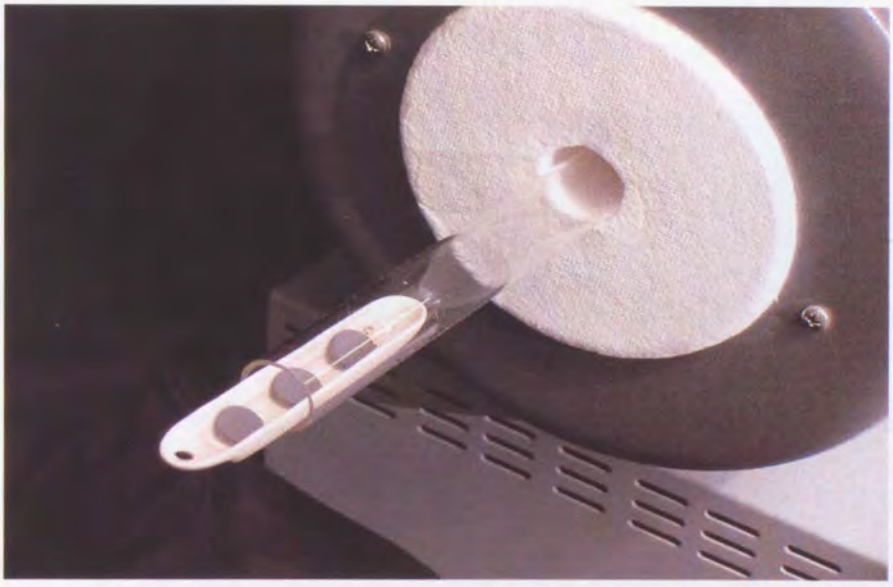

Figure 3-4 Three pellets in ceramic boat at opening of glass tube.

Initially, a manually controlled tube oven was used to heat the samples to about 850° C and then cooled by manual adjustment, incrementally, to room temperature over a period of 24 hours. A chromel-alumel thermocouple was used to monitor temperature. During annealing, the samples were exposed to a constant flow of oxygen. Later, a programmable temperature controller was acquired. This Barnant[2] Temperature Controller R/S model 689-0010 temperature controller (figure 3-5a) is designed to maintain a constant, pre-set process temperature to ± 0.4°C. It uses a microprocessor software algorithm that adjusts the heating or cooling by varying the output duty cycle for loads up to 15 amperes.

Figure 3-5a Temperature Controller for tube furnace

A representative program used with the Barnant temperature controller for annealing samples used the four programming segments below. Figure 3-5b is a time-temperature graph of the annealing sequence. The controller provides a linear change in temperature.

Segment 1 two hours at 800°C (about 30 minutes from room temperature)
Segment 2 30 hours for temperature drop from 800°C to 300°C
Segment 3 four hours for temperature drop from 300°C to 22°C
Segment 4 zero minutes to 'controller off' when 22°C is reached

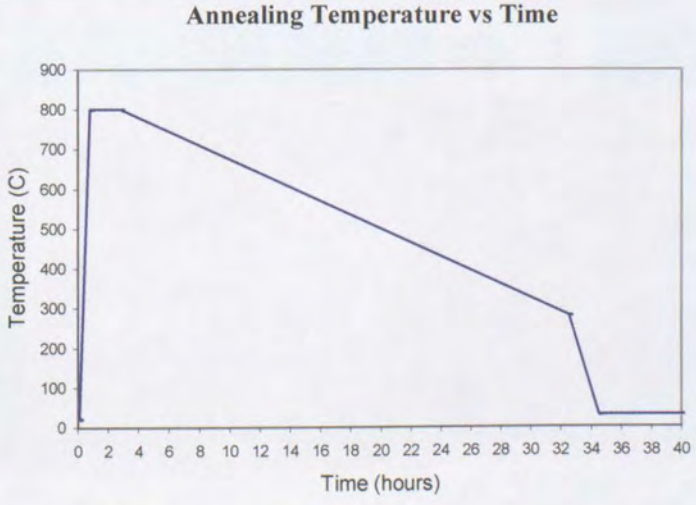

Figure 3-5b

Sample powder not used for pelletizing was used for making x-ray diffraction patterns. This powder, in a uniformly thick layer, was affixed to a microscope slide and placed into the sample holder of the x-ray diffractometer. The x-ray apparatus used, was an older model Philips[3] XRG-3000 scanning diffractometer. The graphs produced verified that the samples were of desired polycrystalline structure and showed very good agreement with similar patterns found in the literature.[4] Subsequent samples were sent to Kingston University for Scanning Electron Microscopy (SEM) analysis.[5]

To investigate the resistivity-temperature relationship, a cryogenic system was used. The apparatus for this system consists of an RMC-Cryosytems LTS-22 Series[6] closed cycle refrigerator system (figure 3-6) and a vacuum pump for reducing the sample chamber pressure to approximately 35 mTorr (4.65 Pascals), monitored with a TeraNova[7] model 924 thermocouple vacuum gauge (figure 3-7). The cryogenic system consists of a compressor, cold head assembly and a temperature controller.

Figure 3-6 Cryogenics refrigerator compressor

Figure 3-7 Terranova vacuum gauge

The compressor unit of the closed cycle refrigerator system is designed to compress the low pressure expanded helium gas from the cold head, remove the resultant heat of compression, and pass the high pressure helium gas to the cold head for re-expansion. The gas flow portion of the compressor contains the compressor pump, oil injection system, heat exchanger, oil separation system, and absorber. In addition, the compressor contains the electronics required for the compressor and cold head power.

The cold head/vacuum shroud assembly (fig.3-8) functions to expand the high pressure helium gas provided by the compressor to produce the refrigeration required for cryogenic temperatures to ± 1% of the preset Temperature. The first stage of the cold head provides refrigeration at a nominal 77 Kelvin and the second stage where the sample is normally mounted (figures 3-10, 3-11), provides refrigeration in a nominal 10 Kelvin. Figure 3-9 on the following page shows a component interconnection diagram.

Figure 3-8 Cold Head unit

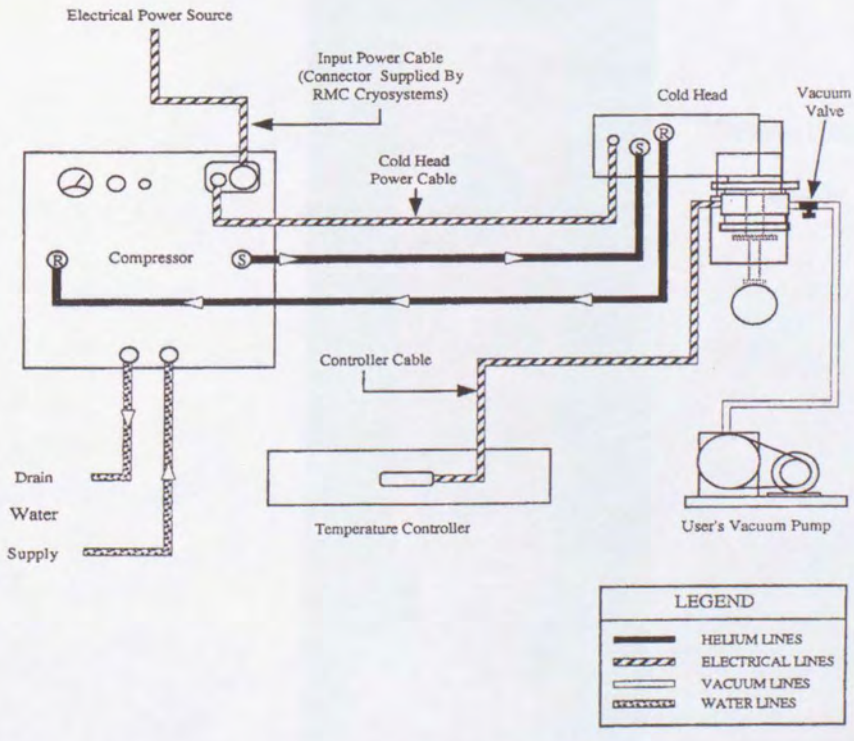

Figure 3-9 Component interconnection diagram

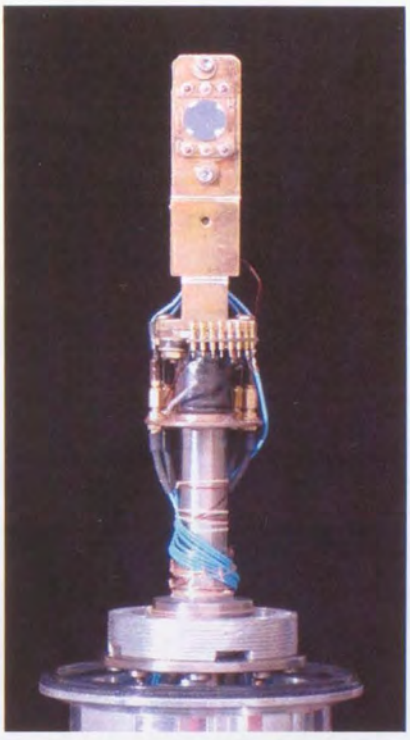

Figure 3-10 Cold finger (shroud removed)

Figure 3-11 Detail of cold finger with pellet attached.

The temperature controller (figure 3-12) supplied with the LTS-22 system provides the capability of obtaining sample temperatures over the entire operating range of the system and within ± 0.03% of the target temperature, rather than just the lowest attainable temperatures.[8]

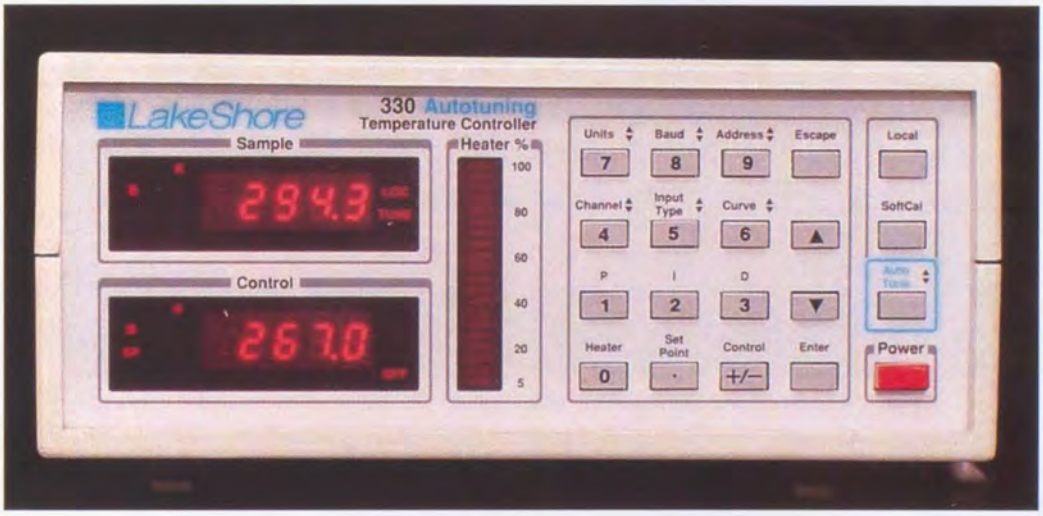

Figure 3-12 Temperature controller for cold head

Additional electronic measurement equipment included a Kiethley model 227 (figure 3-13) polarity reversible, constant-current source and a Kiethley model 182 precision digital voltmeter (figure 3-14, next page).

Figure 3-13 Keithley constant current source

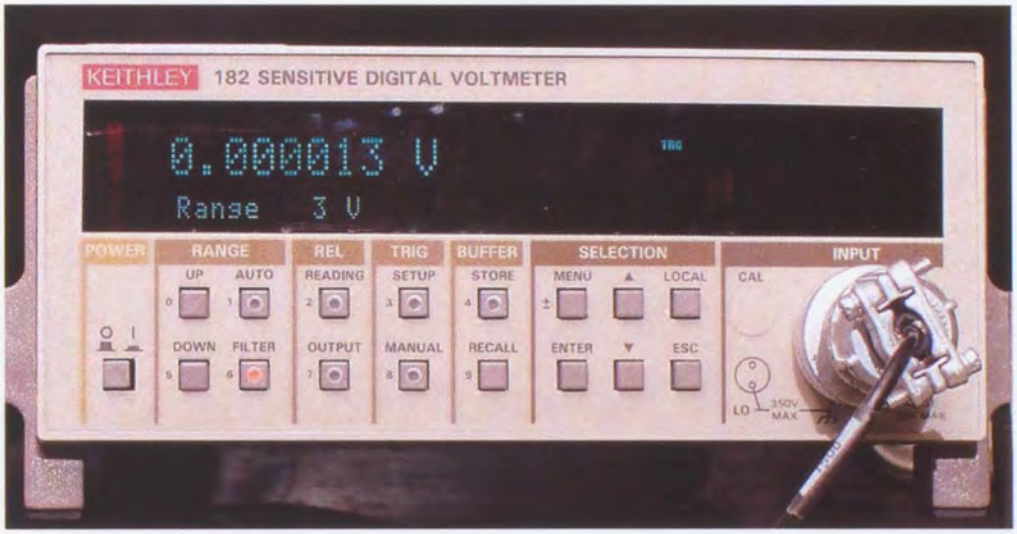

Figure 3-14 Keithley digital voltmeter

Measurements of voltage and current were made using a standard four-probe contact method. Silver paint contacts were symmetrically positioned around the edge of one face of the sample pellet, which was then mounted on the cold-finger (see figure 3-11, page 59). Contacts opposite each other were used for connections to the current source or voltmeter. A switching box, used in conjunction with the polarity-reversing switch on the current source, permitted voltage measurements to be taken in alternately perpendicular directions across the sample and also by reversing the direction of charge flow. The following block diagram illustrates how the electrical components are linked together (figure 3-15).

The resistivity of the pellet samples was obtained by introducing measurements of the physical dimensions of the pellet samples and the electrical data measurements, into the Van der Pauw formula for resistivity. The Van der Pauw formula[9] may be written as

$$\rho = \frac{\pi d}{\ln 2} \frac{(R_{ab,cd} + R_{bc,da})}{2} f$$

where the subscripts a,b,c,d refer to the silver contact points made on one of the flat surfaces, near the edge of the pellet sample, at positions as indicated in figure 3-15. (Also see appendix B, page iv.)

figure 3-15

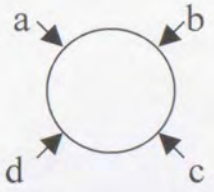

and where

ρ = resistivity in ohm-centimeters R = resistance in ohms (between contact points)
d = thickness in cm (for ρ in Ω-cm) f = correction factor (for shape).

Figure 3-16 is a block diagram of the electronic components connected to the sample that is mounted in the coldhead. The constant current source, typically 10 mA,

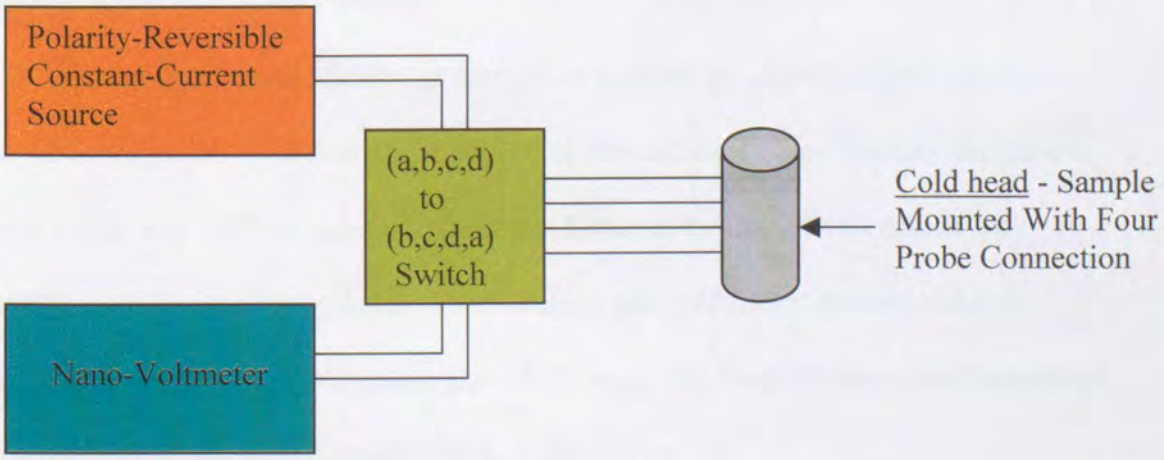

Figure 3-16

is connected to contacts (a,b) and voltage measurements are taken across contacts (c,d). After switching, the constant current source is connected to contacts (b,c) and a voltage measurement is taken across contacts (d,a).

The correction factor 'f' is obtained from the following formula:

$$f = 1 - \left\{ \left(\frac{R_{ab,cd} - R_{bc,da}}{R_{ab,cd} + R_{bc,da}} \right)^2 \frac{\ln 2}{2} \right\} - \left\{ \left(\frac{R_{ab,cd} - R_{bc,da}}{R_{ab,cd} + R_{bc,da}} \right)^4 \left(\frac{[\ln 2]^2}{4} - \frac{[\ln 2]^3}{12} \right) \right\}.$$

Here we let $x = \left(\frac{R_{ab,cd} - R_{bc,da}}{R_{ab,cd} + R_{bc,da}} \right)$

and since $\frac{\ln 2}{2} = 0.3466$, $\frac{[\ln 2]^2}{4} = 0.1201$, $\frac{[\ln 2]^3}{12} = 0.0277$,

then the correction factor is $f = 1 - 0.3466\,x^2 - 0.0924\,x^4$.

This correction factor and the above Van der Pauw formula were used in conjunction with an Excel Spreadsheet for calculating the resistivity of each pellet sample as a function of temperature.

Typically, magnetic fields are applied to samples by positioning the opposite poles of a magnet on each side of the shroud of the cold head. For these investigations, a more stable and uniform magnetic field was obtained by using two ceramic disk magnets. One magnet was placed on each side of the cold finger, sandwiching the pellet sample in between. Measurements of the magnetic field density at the position of the pellet sample were consistently 350 mTesla.[10]

To avoid the possibility of any magnetic remanence, resistivity data were first taken without the magnets in place. Once satisfactory data were obtained without the field, the magnets were positioned with great care for symmetry on all axes about the pellet sample.

Modern and appropriate equipment was used to produce structurally sound polycrystalline doped-manganite samples and to accurately measure their electrical resistivity as a function of temperature, with and without, an applied magnetic field. The existing equipment was improved by the addition of a temperature controller, a switching box for forward/reverse/transverse voltage reading across samples. A new hydraulic die with much finer tolerance pistons and mold was acquired for the sample pellet producing system.

References

1. Eurotherm Controls, Operating Manual #818 Controller/Programmer. Eurotherm Controls Inc. 11485 Sunset Hills Road, Reston, VA, 20190-5286

2. Barnant Temperature Controller R/S model 689-0010 Barnant Company, Barrington, IL, 60010

3 Phillips XRG-3000 scanning x-ray diffractometer Phillips Electronic Instruments, Inc. Mount Vernon, NY

4 X.L. Wang, S.X. Dou, H.K. Liu, et al., Large low-field magnetoresistance over a wide temperature range induced by weak-link boundaries in $La_{0.7}Ca_{0.3}MnO_3$, Applied Physics Letters, Vol. 73 No. 3, 20 July 1998.

5. Electron Microscope Laboratory (WB 35), Bill Edwards, Kingston University, Kingston-upon-Thames, Surrey, U.K.

6. RMC-Cryosystems LTS-22 Series, Research and Manufacturing Company, Inc. 44003 Santa Rita Ave., Tucson AZ, 85714

7. TeraNova Scientific Model 924 thermocouple vacuum gauge Terranova Stockroom Corp., 1305 Space Park Way, Mountain View, CA, 94043

8. LakeShore model 330 Autotuning Temperature Controller Lakeshore Cryogenics, Inc., 64 Walnut St., Westerville, OH 43081

9. Phillips Research Reports, Vol. 13, No. 1, Feb. 1958, A Method of Measuring Specific Resistivity and Hall Effects of Discs of Arbitrary Shape, L.J. van der Pauw

10. Magnetic flux density measurements were made with a model 4048 Bell Gauss/Tesla meter. F.W. Bell Mfg. 6120 Hanging Moss Rd., Orlando, FL, 32807

Chapter 4

Preparation of Polycrystalline Superconducting Samples of $Y_1Ba_2Ca_3O_{7-\delta}$

4.1 Introduction

The era of high transition temperature superconductivity ("High T_c" superconductivity) began in 1986 with the preparation of a barium-doped lanthanum cuprate ($La_{2-x}Ba_xCuO_4$), with a transition temperature of 30 K. Only a few months after this discovery, three main types of high temperature superconductors were found. They are: $Y_1Ba_2Cu_3O_{7-\delta}$ (YBCO), $BiSrCaCuO_{7-\delta}$ and $Tl_2Ba_2Cu_3O_{10}$, with transition temperatures of 90, 104, and 125 K, respectively.[1,2]

The standard procedures for making polycrystalline, superconducting pellet samples of these materials, the experimental techniques and the hardware and equipment required for their characterization are very similar to those necessary for the preparation and characterization of polycrystalline magnetoresistive samples of the doped manganite $La_{(1-x)}Ca_xMnO_3$. As described in Chapter 2, the phenomenon of colossal magnetoresistance (CMR) has been observed in doped manganites. The laboratory and equipment were set up to produce superconducting samples of YBCO. Generally accepted, standard results for this superconductor were used to fine-tune the entire system. Once satisfactory samples were made, the entire system was ready to commence investigations into colossal magnetoresistance.

4.2 Preparation of Superconducting YBCO Samples

For the preparation of the superconducting pellet samples, oxides or carbonates of Y, Ba and Cu (Y_2O_3, BaO_2, $BaCO_2$, CuO) were used with purities of 99.99%, 99.9%, 99.9% and 99.9%, respectively. Since the Yttrium-Barium-Copper oxides and their characteristics have been well documented, the standard 1-2-3 compound $\{Y_1Ba_2Cu_3O_{(7-\delta)}\}$ was used for setting up and getting the entire system functioning properly. In conjunction with several steel dies and pistons, a hydraulic press capable of exerting 134,000 Newtons of force (10^9 Pascals of pressure with the dies used here) was used for forming the pellets.

After mixing, in appropriate proportions, the oxides or carbonates of the elements involved, the chemicals were ground to a very fine powder with an agate mortar and pestle. The sample powder, in a high temperature ceramic crucible, was then placed into a sintering oven where the temperature was monitored with a chromel-alumel thermocouple. Experiments with sintering time and temperatures from 700°C to 940°C over 12 hours to 48 hours, indicated that the best results were achieved by sintering at a temperature of 875°C for 12 hours with two intermediate grindings and sinterings.

Structurally sound sample pellets were produced by adjusting fabrication processes such as pelletizing pressure and compressing technique, sintering time and temperature, and annealing time and temperature. Typical problems that were corrected were fracturing of the pellet upon removal from the die and wafer-like layering of pellets due to inconsistencies within the sample powder when placed into the die. Two important solutions were found that greatly increased the production of good pellet

samples. One solution was to slowly increase the pelletizing pressure by .17 x 10^8 Pa increments and holding at that pressure for several minutes while any trapped air escaped. The other solution came from procuring a substantially thick-wall die, with pistons lengths being twice the diameter of the die hole into which the sample powder was placed. The highly polished die wall was lubricated with steric acid. The use of non-tipping pistons, machined to extremely close tolerance to fit the die hole, assured a constant, evenly distributed pressure over the entire sample powder within the die chamber. After experimenting with a range of pressures used with the hydraulic press and the dwell-time for the pressure increase increments, it was found that ideal pelletizing was achieved with a pressure of 5.5 x 10^8 Pa, increased at 2-3 minute intervals at .17 x 10^8 Pa each.

Annealing in oxygen has become a standard practice as it has been found that the superconducting transition temperature decreases continuously with decreasing oxygen content.[3] The pellet samples were placed in a ceramic boat and inserted into the quartz-glass tube of a tube oven and centered in the oven where they were annealed in a continuous flow of oxygen for 24 hours as the temperature decreased from 770°C to room temperature.

4.3 Characterization of YBCO Samples

The post-annealing process included cutting the sample into a parallelepiped shape. After cleaning the sample with acetone, the sample was mounted on the plug-in frame which inserts into the electrical contacts of the cold finger within the cold head. Silver paint was used to make wire contacts on the sample at each end and two contacts

spaced approximately one-third the length of the sample, from each end. The contacts thus situated were used as a four-probe method for electrical measurements of voltage change with temperature.

The principle technique used to determine the onset of the superconducting state is to measure electrical resistance as a function of temperature R(T). When a ready indication is desired, a two-probe measure across the specimen is most convenient. A better and more precise method, that eliminates the resistance of the contacts, uses a four-probe contact setup for determining R(T).

Using a jeweler's saw, the specimen for which resistance measurements were made was cut into a symmetric shape such as a parallelepiped. Two contacts (probes) for input current were attached near the ends and two contacts (probes) were attached near the center, all in a linear fashion. For the input current, a constant current source was used.

Being placed close together, the center two voltage-contacts have a very small amount of specimen material and therefore resistance between them. This small specimen resistance in parallel with the very large voltmeter resistance, permits virtually all of the current to pass between the specimen voltage contacts. The silver contact resistance at the current input points is negligible. The similarly very low resistance of the silver voltage contacts on the specimen and at the voltmeter and the very high input resistance (ohm/volt) of the voltmeter assure a very accurate voltage measurement between the center-two (voltage) contacts on the specimen.

Since this phase of the equipment and process setup was intended to establish a functional system for investigations into colossal magnetoresistance, resistance

measurements rather than resistivity measurements were made to verify that samples were in fact superconducting. Resistance measurements are easy to make and provide a clear indication of the onset of superconductivity. That the entire process and system were functioning properly is shown in the resistance-temperature graph below (fig. 4-1).

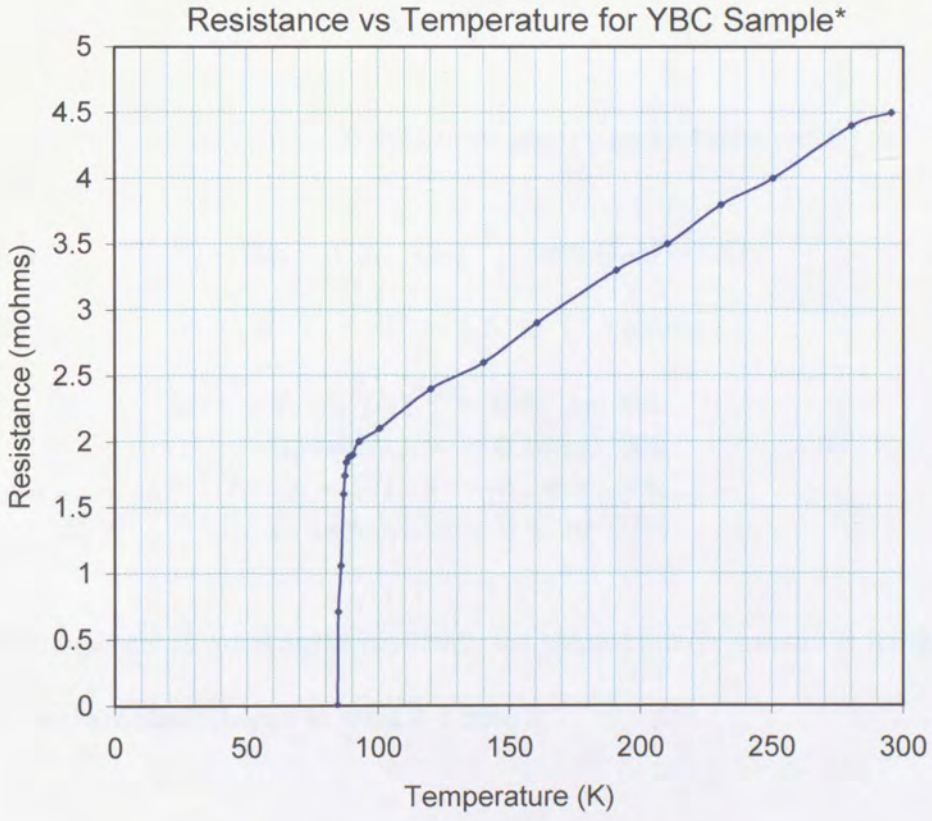

* See section 4.3, page 68

Figure 4-1. Electrical resistance in ohms as a function of absolute temperature for a polycrystalline sample of $Y_1Ba_2Cu_3O_{7-\delta}$.

As the oxygen content increases during the annealing process and more grains undergo the structural phase transition from tetragonal to orthorhombic, the onset of the superconducting transition temperature (T_c) increases up to 92 K. Typically, samples of

$Y_1Ba_2Cu_3O_{7-\delta}$ with $\delta \approx 0.2$ yield an onset of T_c at 90 K.[1] The oxygen content of the superconducting samples used here could be increased with further oxygen annealing.

The YBCO samples used here were analyzed and the compositions were determined by electron microprobe x-ray analysis (sometimes referred to as Energy Dispersive Analysis of X-rays or EDAX).

A cursory arithmetic check to determine atomic percentages yields:

$Y_1 \quad Ba_2 \quad Cu_3 \quad O_{7-\delta}$ [where $(7-\delta) = 6.5$]

or $1 + 2 + 3 + 6.5 = 12.5$ atoms

so
$Y \rightarrow 1/12.5 = 0.08$ or 8%
$Ba \rightarrow 2/12.5 = 0.16$ or 16%
$Cu \rightarrow 3/12.5 = 0.24$ or 24%
$O \rightarrow 6.5/12.5 = 0.52$ or 52%

These percentages are in good agreement with the sample analysis made at Kingston University[5] and are summarized in table 4-1 below.

Element	Theoretical Atomic Percentage	Sample Analysis[5] Atomic Percentage
Y	8	8.04
Ba	16	15.31
Cu	24	24.64
O	52	52.01

Table 4-1 Table of theoretical and actual atomic percentages

References

1. F.J. Adrian, D.O. Cowan, Johns Hopkins University Applied Physics Labs, The New Super Conductors, C & EN, 21 Dec. 1992.

2. C. W. Chu, J. Bechtold, L. Gao, P.H. Hor, Z.J. Huang, R.L. Meng, Y. Y. Sun, Y. Q. Wang, Y.Y. Xue, Phys. Rev. Lett. 60, 941 (1988).

3. C.P. Poole Jr., T. Datta, H.A. Farach, Copper Oxide Superconductors, Wiley Interscience Publications, John Wiley and Sons, 1988.

4. P.F. Bongers, C. Schlenker, B. Stritzker, High T_c Superconductors, Proceedings of Symposium A, Nov. 1988.

5. Electron Microscope Laboratory (WB 35), Bill Edwards, Kingston University, Kingston-upon-Thames, Surrey, U.K.

Chapter 5 Preparation of CMR Samples

5.1 Introduction

Initially, after the discovery of a new type of solid-state compound that exhibited the phenomenon of colossal magnetoresistance, the immediate interest of researchers was focused on its characterization. This characterization was done immediately after the pellet samples of the compound were produced. While this immediate characterization yielded interesting and useful results, the long-term usefulness of the samples was limited due to the physical instability of the pellets. Little attention was given to the preparation of structurally sound pellet samples that could be studied over an extended period of time.[1-5]

In this research project, recognizing the importance of long lasting and stable solid state structures in technological applications, a new method in the preparation of structurally sound polycrystalline samples of doped manganites was developed. This new method introduced into the process is called "flashing".

5.2 Sample Preparation

Using the procedures and techniques for producing superconducting YBC samples (see chapter 4), colossal magnetoresistive pellets of $La_{0.7}Ca_{0.3}MnO_3$ were prepared from a mixture of high quality La_2O_3, $CaCO_3$ and MnO_2 (99.99% pure). These pellets, commonly referred to as LCM compounds, were made using standard stoichiometric methods to produce the compound $La_{0.7}Ca_{0.3}MnO_3$.

The consistency of the LCM compound was of such a nature that it would not bond with the normal heat treatment and pelletizing pressure used for the YBC samples.

Pellets formed using the same technique were found to literally disintegrate after only a few hours. A typical pellet fabrication process would be

- Oxides finely ground
- Sintering at 1100°C for 12 hours
- Regrind, sinter at 1130°C for 14 hours
- Press into pellet using 5.7×10^8 Pa of pressure with hydraulic press
- Anneal in oxygen from 950°C to 450°C over 12 hours

Experiments using pressures varying from $.33 \times 10^8$ Pa to 6.7×10^8 Pa were made and all pellets disintegrated soon after pressing, regardless of the pressing force used. Control pellets were set aside and not annealed, to determine if the annealing process affected the stability of the pellets. It was determined that it did not. (See figures 5-1,2,3,4.)

Figure 5-1 Pellets before annealing.

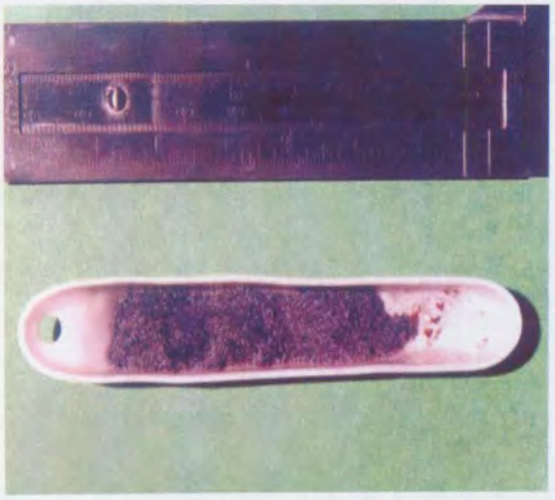

Figure 5-2 Same pellets several days after annealing.

Figure 5-3 Same disintegrated pellets showing that 2.2, 5.7 and 89.1 kN pelletizing force made no difference in structural integrity.

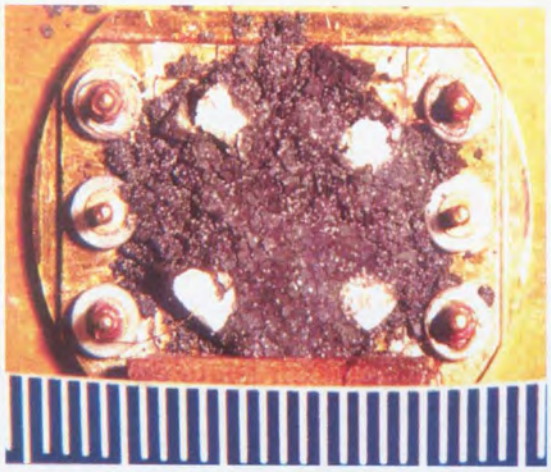

Figure 5-4 A pellet initially presumed stable, lasted three days. Here, removed from coldhead, silver contacts are visible.

Clearly, the heat treatment/pelletizing process needed to be modified. Although conversations with Dr. Fontcuberta, a scientist at the Universidad Autonoma de Barcelona, confirmed that the sample structural instability was experienced in other labs, a review of the literature revealed no practical information regarding researcher's pellet fabrication techniques.

While most articles would mention pelletizing and sintering, specific pressures or forces were not stated and only general time-temperature figures were provided, some of which were clearly unusable. No reference to structural stability of polycrystalline samples was found in the reviewed literature. A change in details of the R(T) curve for $La_{0.7}Ca_{0.3}MnO_3$ thin-film with Cr ions implanted was noted when measurements were repeated two weeks later.[6] We believe that this was due to structural instability. The production of structurally sound samples will be vital in future applications of CMR.

The structural integrity of the pellets was achieved by including a "flashing" process within the usual pellet fabrication process. This 'flashing' involved placing the newly formed pellet in an oven where it was subjected to a rapid increase in temperature, sufficient to cause a partial-melting of the material and cause the grains to grow larger and bond together. Numerous experiments were required to find the correct 'flashing' time and temperature that would produce the requisite bonding without damaging the pellet. The process was so successful that pellets over a year old show no signs of disintegration.

As a starting point in the investigation to find the optimum flashing time and temperature, the sample pellet was heated to 1300°C for 12 hours. As the following figures (figures 5-5 and 5-6) illustrate, this time and temperature was much too great, with the sample melting through the inverted crucible upon which it was placed in the furnace.

Further experiments revealed that when the sample was heated to 1250°C for two hours, the material began melting and became fluid but when heated to 1230°C for two hours, the material showed some melting while retaining granularity.

Figure 5-5 Hole in bottom of crucible which through sample pellet melted.

Figure 5-6 Inside of crucible showing melted path where sample pellet slid down inside.

Continued tests narrowed the flashing range to temperatures between 1300°C and 1525°C with flashing time held to 10 minutes. To ascertain which combination would maximize the change in magnetoresistance, three pellets were flashed at 1300°C, 1450°C and 1525°C and labeled sample #1, #2 and #3, respectively. Resistivity measurements were made, with and without samples being subjected to a magnetic field (approx. 350 mTesla). The percentage change in resistivity was calculated using the two maximum resistivity values for each sample, with and without the magnetic field. Sample #1 (1300°C) produced a 2.4% MR change, sample #2 (1450°C) a 4.3% change and sample #3 (1525°C) a 2.9% change (see fig. 5-10, pg. 62). It can be seen from the scales on the graphs (figures 5-7,8,9) that as the flashing temperature increased, causing an increase in grain size, the resistivity decreased. Also, the metal-insulator transition temperature for the lower flashing temperature is lower than that of the two higher flashing temperature samples. While samples #2 and #3 exhibit a greater percentage change in MR at their respective transition temperatures, sample #1 shows less variation and greater percentage MR over a wider temperature range, a desirable characteristic for magnetoresistive materials.

Figure 5-7 Resistivity curves for sample #1 (1300°C)

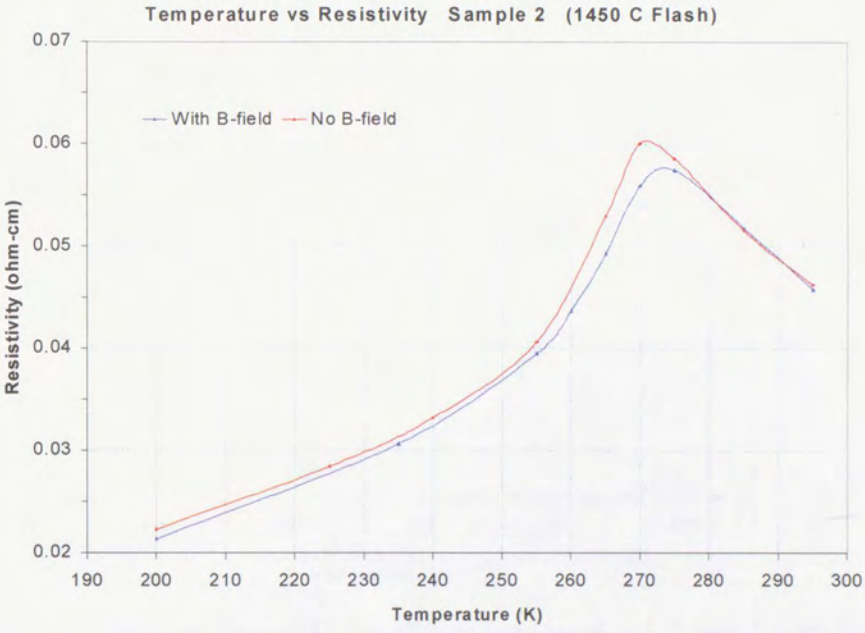

Figure 5-8 Resistivity curves for sample #2 (1450°C)

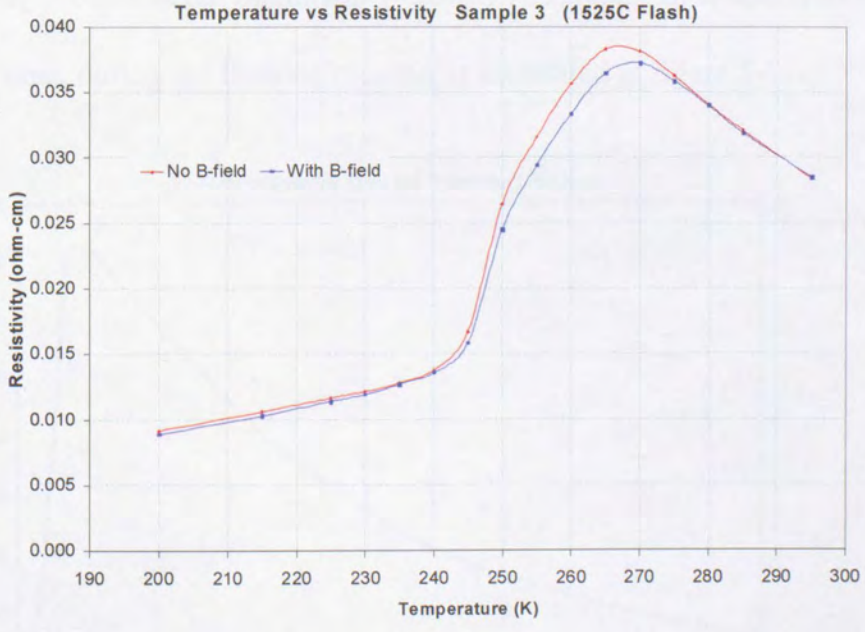

Figure 5-9 Resistivity curves for sample #3 (1525°C)

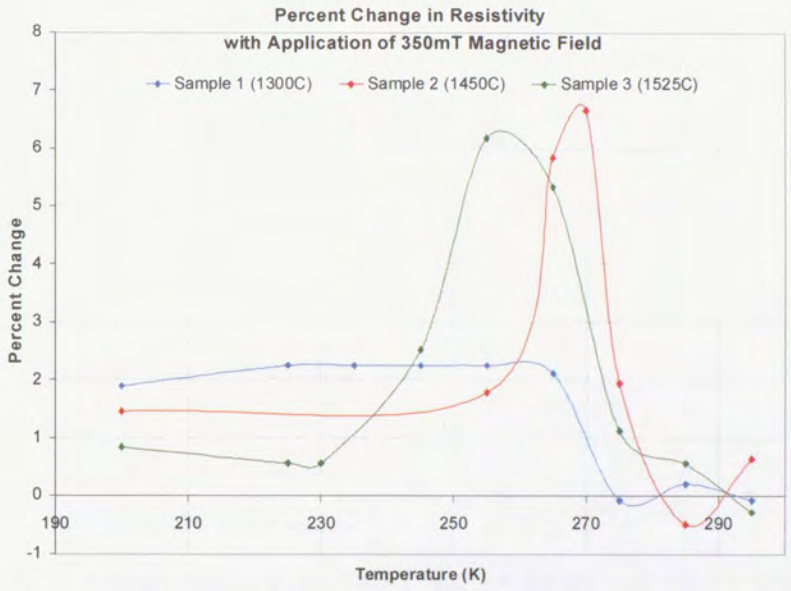

Figure 5-10 Percent change in resistivity for samples 1,2 and 3 with each curve referenced to its own maximum resistivity for no magnetic field.

The subsequent refinement of the flashing technique combined with visual inspections, over time, of the sample pellets resulted in a favored time and temperature for the flashing process of ten minutes at 1450°C. The change in temperature of the sample with time, during the flashing process, is illustrated in figure 5-11.

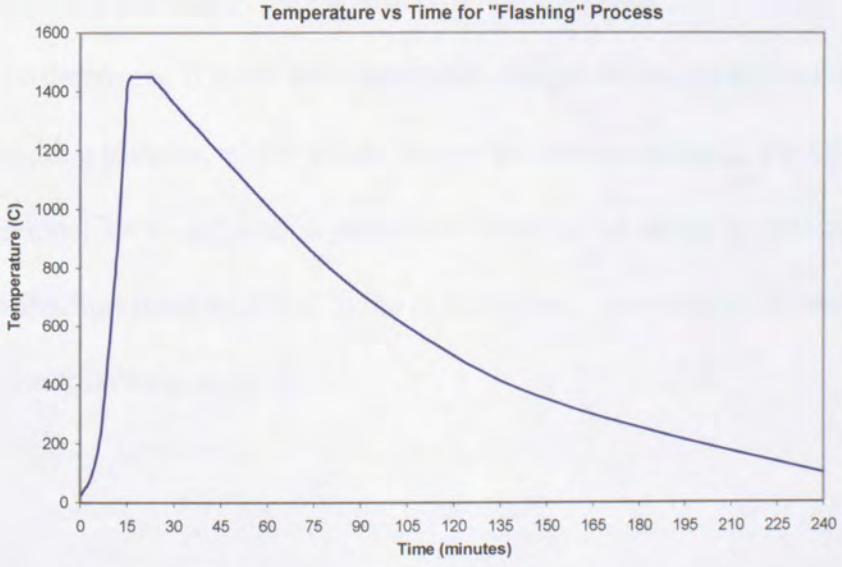

Figure 5-11

Two other considerations must be incorporated into a general pellet fabrication procedure. It has been found that when grain size is reduced, there is a greater change in magnetoresistance.[7] Also, that the Curie Temperature (T_c) increases with oxygen content.[8] With these considerations, in order to maximize T_c and MR, the following pellet fabrication process was established.

- Oxides finely ground
- Mixture sintered at 1180°C for 14 hours
- Mixture reground and sintered at 1180°C for 14 hours
- Mixture pressed into pellets
- Pellets 'flashed' at 1450°C for 10 minutes
- Pellets held in O_2 at 800°C for 24 hours
- Pellets annealed for 5 days in O_2 from 800°C to 450°C

This process produced pellets that were structurally stable with no indication of weakening or deterioration over a period of seven months.[9]

To determine if there were structural changes to the crystalline structure caused by the flashing process, which would render the sample unusable for CMR investigations, X-ray diffraction patterns of some of the samples were compared to X-ray diffraction patterns found in the publications.[7] An example is shown in figure 5-12 on the following page.

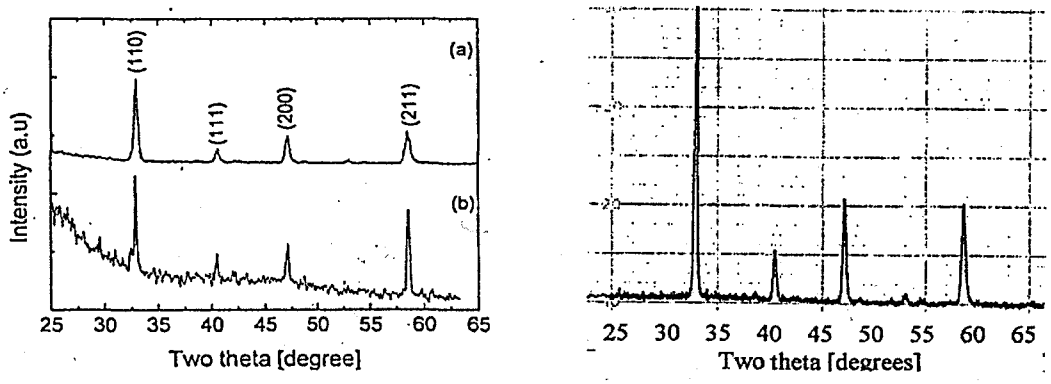

Figure 5-12 Left--published X-ray diffraction pattern.[6] Right--X-ray diffraction pattern of an LCM sample after flashing.

A desirable characteristic of magnetoresistive materials would be a large change in resistivity over a large temperature range, induced by a 'low' magnetic field. Much of the early research involved the use of 'large' magnetic fields (several Teslas), depending on the compound being investigated and temperatures below 80 K. More recent investigations have revealed interesting factors that affect magnetoresistance. For example, researchers at the University of Cambridge and Imperial College[10] found that bulk $La_{0.67}Ca_{0.33}MnO_3$ samples made with varying grain size showed that while resistivity increased with reduced grain size, magnetoresistance increased. The Curie temperature T_c remained constant.[7] The experimental results of samples 1, 2 and 3 are in agreement with previous observations where resistivity increased as grain size decreased.

Other researchers suggest that an optimal grain size should be around 1-3 microns and that greater magnetoresistance can be achieved by increasing the number of weak-link grain boundaries by using smaller grain sizes.[10] Their investigations also showed that a partial-melt, fusing grain boundaries together, enhanced the magneto-resistive effect when subjected to a 'small' applied magnetic field (~300mT).[11]

References

Ref. 1-5*

1. G.C. Bhar, et al, J. of Magnetism and Magnetic Materials 188, 180-184, 1998.
2. L. Balcells, et al, Physical Review B, Vol. 58, No. 22, December 1998.
3. J.R. Sun, et al, Applied Physics Letters, Vol. 73, No. 20, November 1998.
4. X.L. Wang, et al, Applied Physics Letters, Vol. 73, No. 3, July 1998.
5. R. Mahendiran, et al, J. Phys. D:Appl. Phys. 28, 1743-1745m 1995.

6. L. F. Cohen, K. A. Thomas, R. Chater, J. D. M-Driscoll, T. Tate, N. D. Mathur, M. G. Blamire, and J. B. Evetts, Appl. Phy. Letts., 73, No. 7, 1005 -1007, 17 August 1998.

7. X.L. Wang, S.X. Dou, et al, Large low-field magnetoresistance over a wide temperature range induced by weak-link grain boundaries in $La_{0.7}Ca_{0.3}MnO_3$, Applied Physics Letters, Vol.73 No.3, 20 July 1998.

8. Fei, Yang, Oxygen Effects In Lanthanum Calcium Manganese Oxide (Thin Film, Magnetoresistance), Chinese Univ. of Hong Kong, DAI 59 #11B, 1997

9. **Jerry Brower**, **Javier Estrada**, Stable Polycrystalline CMR Materials, High-Tech Materials Alert, Technical Insights, May 19, 2000.

10. J.E. Eveffs, U. of Cambridge, J.L. MacManus-Driscoll, Imperial College, To Elucidate and Optimise the Properties of CMR oxide materials, Summary Report on EPSRC Grants GR1K73862 & GR/K71516

11. G.C. Bhar, U. Chatterjee, et al, Magnetoresistance effect in bulk samples of $La_{0.67}Ca_{0.33}MnO_3$ under a low magnetic field, Journal of Magnetism and Magnetic Materials, 188 (1998) 180-184, 6 March 1998.

*Out of scores of articles reviewed, only these five articles describe sample preparation. While no pelletizing pressures are provided, the articles do provide sintering times and temperatures. Of all of the articles reviewed, including these five, none address the subject of a sample instability or disintegration.

Chapter 6 Experimental Results and Analysis

6.1 Introduction

As previously mentioned (see chapter 2), the first goal of this research project was to find an experimental method for the preparation of structurally sound Ca, and Ca and Fe doped manganites. This objective was achieved with the development of a new process called "flashing", discussed in chapter 5.

Several samples prepared for this project, using this technique, were left in open crucibles, exposed to the atmospheric environment of the laboratory – dry during the winter and humid during the summer. After about three years of exposure, no visible sign of deterioration has been observed in these pellets. In a couple of cases, resistivity measurements vs. temperature were taken several months after the electrical resistance was measured for the first time. The results were the same.

This structural stability contrasts with our initial experience with pellets changing into dust after a few days of their preparation. Recently, a conversation with Dr. Fontcuberta (a researcher at the "Instituto de Ciencias de Materiales" of the "Universidad Autónoma de Barcelona") confirmed that this lack of structural stability was a common denominator, especially in the case of the preparation of Sr doped CMR samples. We believe that many of the electrical resistivity vs. temperature curves found in the literature represent measurements taken immediately after the corresponding pellet was prepared, and that the important problem of structural stability was simply not addressed. We expect that the "flashing" technique can be applied to the preparation of any doped manganite.

In order to find the optimum process in the preparation of structurally sound samples, many polycrystalline pellets were prepared and characterized. Normally, the typical insulator-metal transition was observed but the resistivity vs. temperature characteristic changed with time due to structural instability.

Two pellets were pressed to pressures of 1.7×10^8 and 5.7×10^8 Pa, respectively. These samples were flashed at 1230°C for 10 minutes and then they were annealed in an oxygen atmosphere for 48 hours. As shown in chapter 5, the flashing technique used in the preparation of the samples did not affect their polycrystalline structures. Even though both pellets were difficult to cut using a jeweler's saw, they were labeled "soft" and "hard" because of the pressures used in their preparation.

Using a standard four-probe technique, the resistance vs. temperature (R vs. T) characteristics for both samples were obtained, with and without an applied magnetic field of the order of 350 mT. See figures 6-1 and 6-2, page 85.

It is interesting to notice that in the case of the "hard" sample the magneto-resistance was positive. A new R vs. T curve was obtained again with the same result. The "soft" and "hard" samples were used in a collaboration study between our lab at Grand Valley State University and The University of South Carolina where sophisticated equipment for magnetic measurements is available. The two samples were characterized by electron-microscope analyzes, resistivity vs. temperature, magnetic susceptibility, and magnetoresistance at different magnetic field strengths (0, 100, 200, 300, 400, 500, and 1000 mT). These results were presented during the general annual meeting of the American Physical Society in March of 2002, and are summarized together in the following pages.[1, 2, 3]

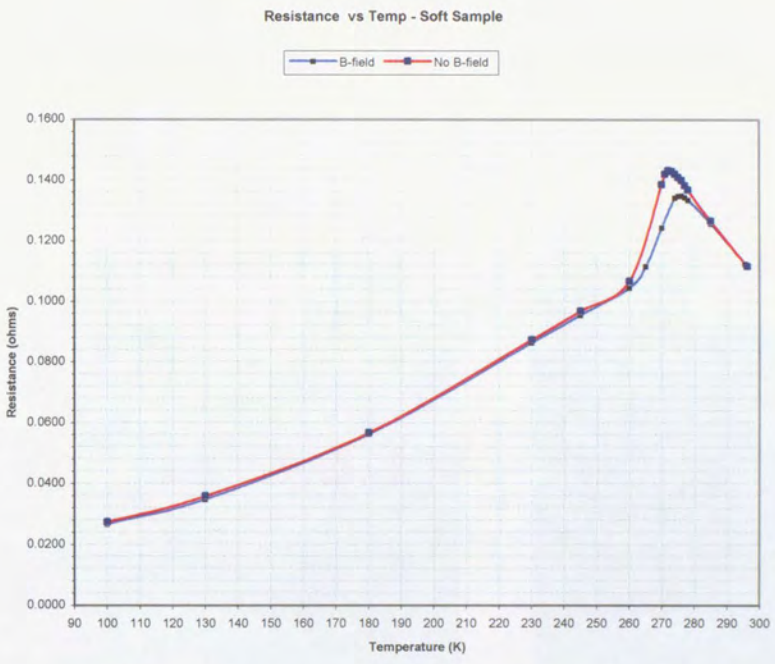

Figure 6-1. Four-probe resistance vs. temperature, with and without an applied magnetic field of the order of 350 mT, for the "soft" sample.

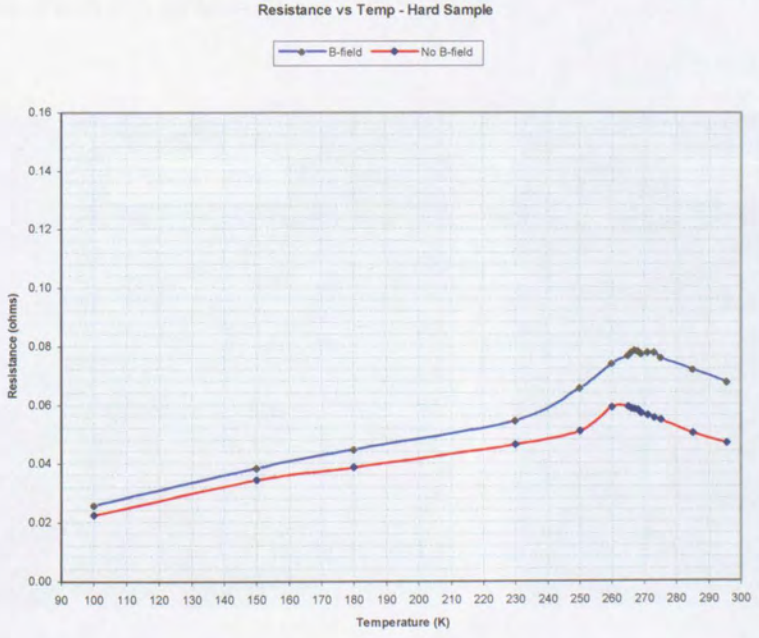

Figure 6-2. Four-probe resistance vs. temperature, with and without an applied magnetic field of the order of 350 mT, for the "hard" sample.

As shown in the following scanning electron micrographs (secondary electron images), the hard sample is denser and its grains are more connected and partially fused to one another. At a 6000x magnification, no inter-granular material can be observed.

a)

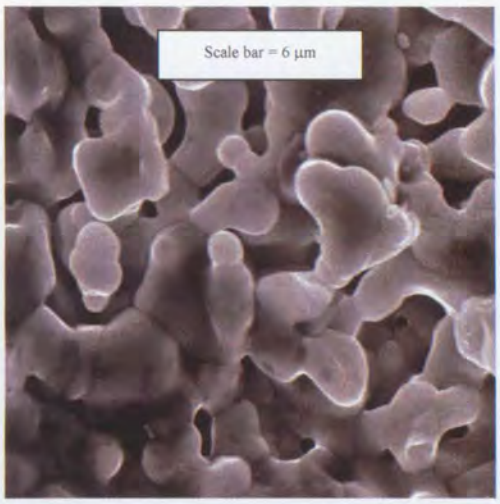

b)

Figures 6-3, **a)** Hard CMR sample at 500x magnification, note the uniformity and high density of grains. **b)** Hard CMR sample at 6000x magnification where the connectivity of the grains can be seen.

c)

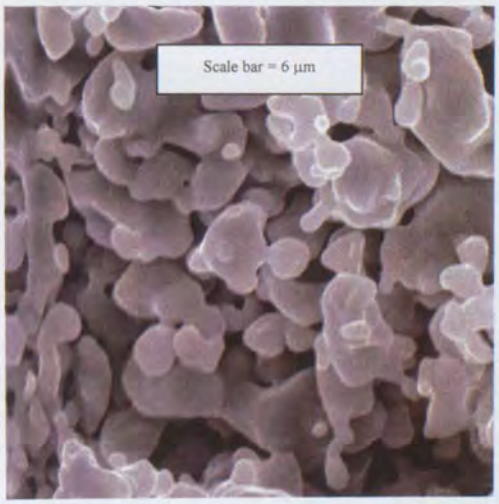

d)

Figures 6-3 **c)** Lower density soft CMR sample at 500x magnification. **d)** The soft CMR sample as seen at 6000x magnification. Compared to the previous micrograph, the grains are less connected.

As explained in the introduction to this chapter, the magnetic measurements for the hard and soft samples were made at the University of South Carolina and at the National Magnetic Laboratory (NML) in Tallahassee, Florida, where appropriate and sophisticated equipment was available. The graphs (figures 6-4 through 6-16) were produced from the data obtained at these facilities and were received in an electronic format for subsequent reproduction in this thesis.

The NML uses non-SI measurement units with the equipment at that facility. For this reason, the axes labels and numerical units used in the graphical representations produced from the analyses performed at that facility are reproduced, as received, with non-SI units. The following paragraphs provide useful information for interpreting the graphs (figures 6-6 through 6-15).

Figures 6-6 and 6-7:

The red circles represent experimental data and the green blocks represent computer generated data using the equation printed on the graph. The equation is for a straight-line, y=b+mx. The correlation coefficient R indicates the relationship between log(R/T) and $T^{-1}(K^{-1})$ where R in log(R/T) is the resistance, not to be confused with R printed on the field of the graph and typically used to express the correlation coefficient in computer programs. The correlation coefficients of .9996531 and .9898576 for figures 6-6 and 6-7, respectively, indicate a very strong correlation and therefore linearity.

Figures 6-8, 6-14 and 6-15:

The information about the best-fit between the experimental data (red circles) and the computer generated data (green squares) is given by the inset of figure 6-8. The first line of the inset shows the equation of the power law used in the computer program (y = m1 + m2*m0^m3) where the numbers 0,1,2 and 3 are subscripts. This equation, written in terms of resistivity and temperature is $\rho = m_1 + m_2 T^{m_3}$. The computer calculated values of m_1 and m_2 and the exponent m_3 are also shown in the inset. The large number of significant figures are an artifact of the computer program generating the values graphed. This precision is limited by the error, seen in the inset, and is based upon the number of significant figures of the actual data. Furthermore, the inset gives the calculated value of chi-square (Chisq) and the correlation coefficient (R). The smaller the value of chi-square, the better the agreement between experimental and theoretical values. Chi-square = 0 would mean a perfect fit. The chi-square value in the inset, on the order of 10^{-9}, indicates an exceptionally close fit as can be seen by the curves in the graph itself. A correlation coefficient between zero and one indicates the relationship between the data being compared, with R=0 having no correlation and R=1 being a very strong relationship. The value in the inset indicates a very strong relationship with a value of .9999592. Similar insets are used in figures 6-14 and 6-15.

Figures 6-9 and 6-10:

The insets show the symbols used in each case for normalized resistance versus temperature. After each symbol is a ratio between resistance measured with an applied magnetic field at a given temperature, to its value with zero field and T=300 K.
For example, R(0.3,T)/ R(0, 300) means the ratio of resistance at 0.3 Tesla at a specific value of T (K) to the resistance at zero Tesla and at T=300 K.

Figure 6-13:

Since it is simpler to accurately measure the mass of a sample rather than its volume, in magnetic labs it is preferred to calculate mass susceptibility (magnetic moment per unit mass per magnetic field intensity). In addition, the cgs system of units is normally used at the above mentioned labs. The units for mass susceptibility in this graph are in (emu/g.gauss).
The corresponding units for mass susceptibility [χ_m] in the SI system would be

$$[\chi_m] = \left[\frac{(\text{mag. moment per unit mass})}{(\text{mag. intensity})}\right] = \frac{\left(\frac{Am^2}{kg}\right)}{(Am^{-1})} = \frac{m^3}{kg}$$

In the inset of the figure, the symbol used in each graph is shown together with the mass susceptibility, the units, and the corresponding field intensity.

As it can be seen in the next two graphs, both samples clearly show the insulator to metallic transition at a temperature of about 277 K.

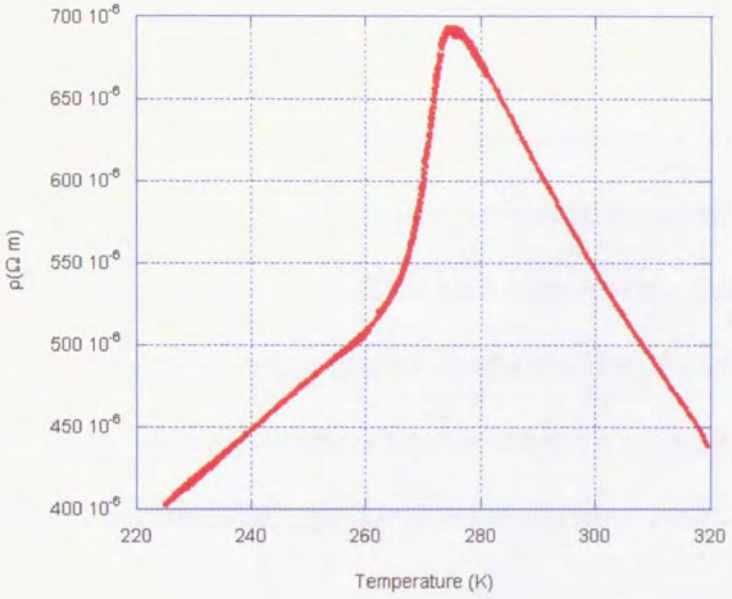

Figure 6-4. Resistivity vs. temperature for the "soft" CMR sample in the temperature range from 220 to 320 K.

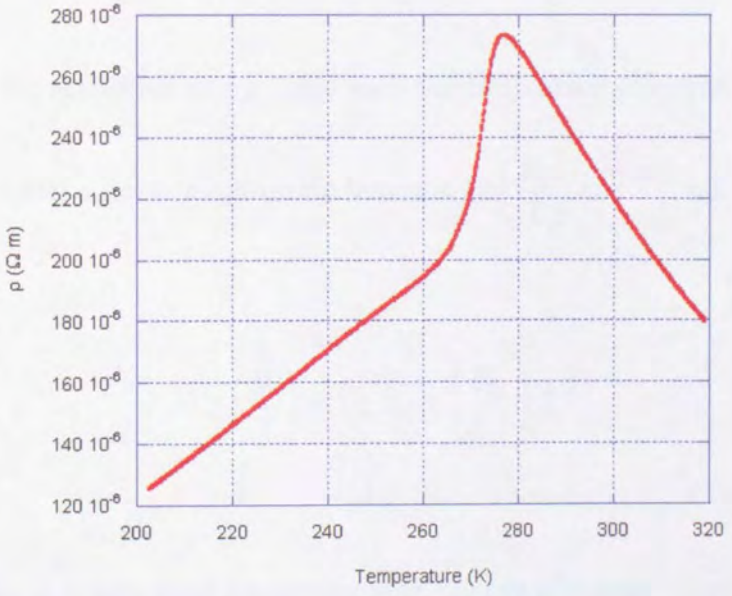

Figure 6-5. Resistivity vs. temperature for the 'hard' CMR sample in the temperature range from 200 to 320 K.

In both cases (soft and hard samples), from 220 K to 260 K, the electrical resistivity increases linearly with temperature (metallic transport). Above 280 K, the electrical resistivity decreases linearly with temperature (insulating transport). The temperature where the metal-insulator transport transition occurs is very similar for soft and hard samples, and coincides well with the Curie temperature, as confirmed by the magnetic measurements shown later. These experimental values of resistivity are such that, at any temperature, the resistivity of the hard sample is less than the resistivity of the soft sample, i.e., the hard sample is more conductive than the soft.

For the temperature region above the transition, the model by Jaime and Salomon predicts an exponential behavior given by equation 6.1.[4,5]

$$\left(\frac{R}{T}\right) = R_0 \exp\left(\frac{E_\sigma}{k_B T}\right) \tag{6.1}$$

where E_σ is the activation energy, and k_B is the Boltzmann constant. From this equation we should expect a linear relationship between $\mathrm{Ln}\left(\frac{R}{T}\right)$ and T^{-1}, i.e.

$$\mathrm{Ln}\left(\frac{R}{T}\right) = \mathrm{Ln}\, R_0 + \left(\frac{E_\sigma}{k_B}\right) T^{-1} \tag{6.2}$$

This model is in a very good agreement with the experimental results for the soft and hard samples as shown by the following figures 6-6 and 6-7 (also see page 90).

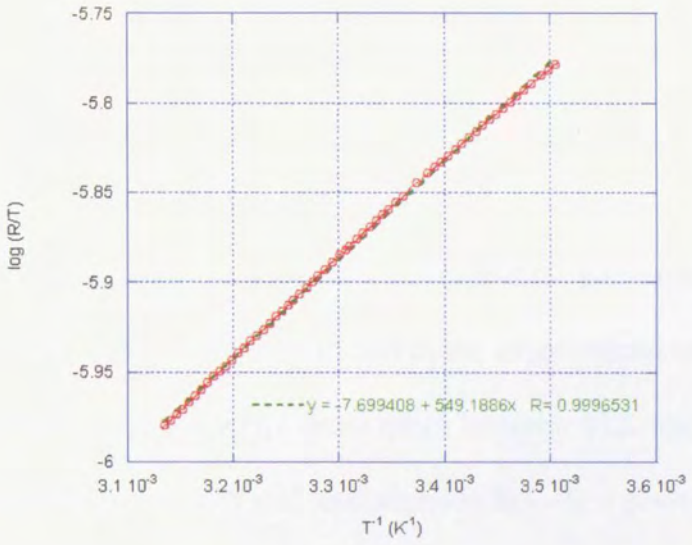

Figure 6-6. Ln (R/T) vs. T^{-1} for the hard sample, in the temperature range between 280 K and 320 K.

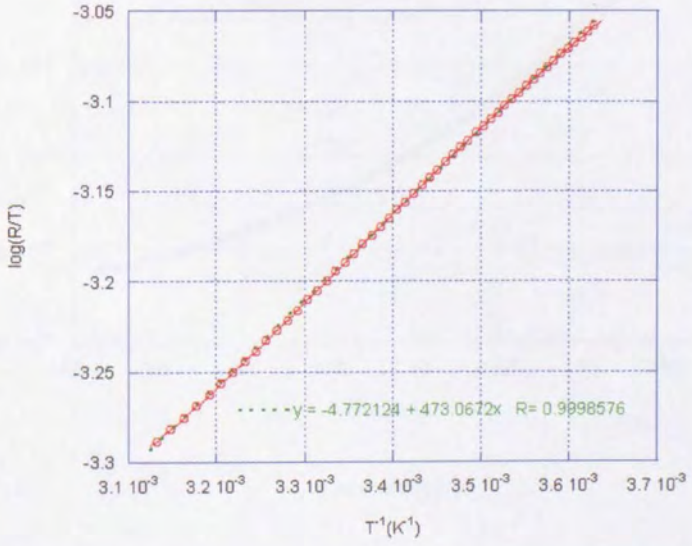

Figure 6-7. Ln (R/T) vs. T^{-1} for the soft sample, in the temperature range between 280 K and 320 K.

For a small temperature range, just below the transition, ferromagnetic ordering produces a sharp drop in resistivity. This ferromagnetic transition is clearly observed in a graph of magnetic susceptibility vs. temperature (see figure 6-13).

Mainly because of magnetic ordering and mixed phases, the region below the transition temperature, down to about 200 K, is the most interesting but more difficult to understand. No simple model was found to fit the experimental results in this region.

Well below T_c, in the temperature range between 40 K and 180 K, our experimental results for the soft and hard samples fit well, a power law where the electrical resistivity is directly proportional to $T^{2.29}$. This type of power law, illustrated in figure 6-8 for the soft sample, was observed in other research projects [6].

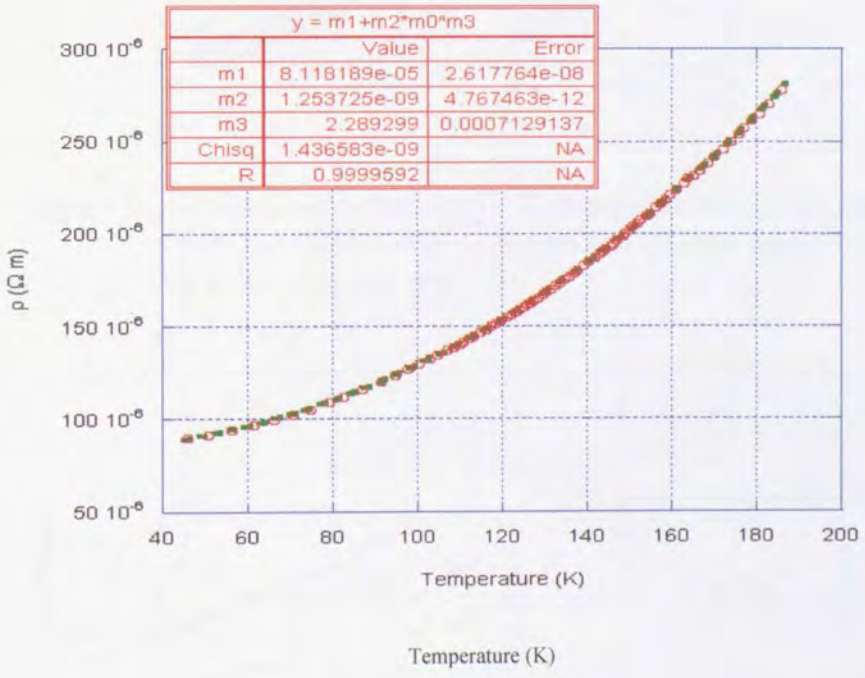

Temperature (K)

Figure 6-8. ρ vs. T for the soft sample in the temperature range between 45 K and 185 K (red dots). The dashed green line represents a power law fit where the power of T is treated as an independent variable. The best fit corresponds to $T^{2.29}$.

As the temperature of a 30% Ca doped manganite sample is lowered from room temperature, the sample undergoes ferromagnetic ordering below the Curie temperature and the electrical resistivity decreases. In the presence of an external magnetic field the ferromagnetic ordering is further enhanced and an additional drop in resistivity is expected. Figures 6-9, and 6-10 show the effect of different applied magnetic fields on the "hard" and "soft" samples, respectively.

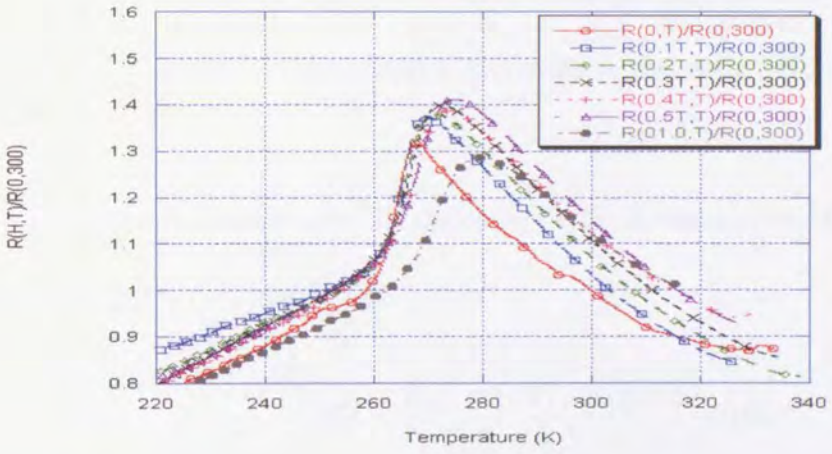

Figure 6-9. Normalized resistance vs. Temperature curves for the "hard" sample near the transition temperature, at different magnetic fields (0, 0.1, 0.2, 0.3, 0.4, 0.5, and 1 T).

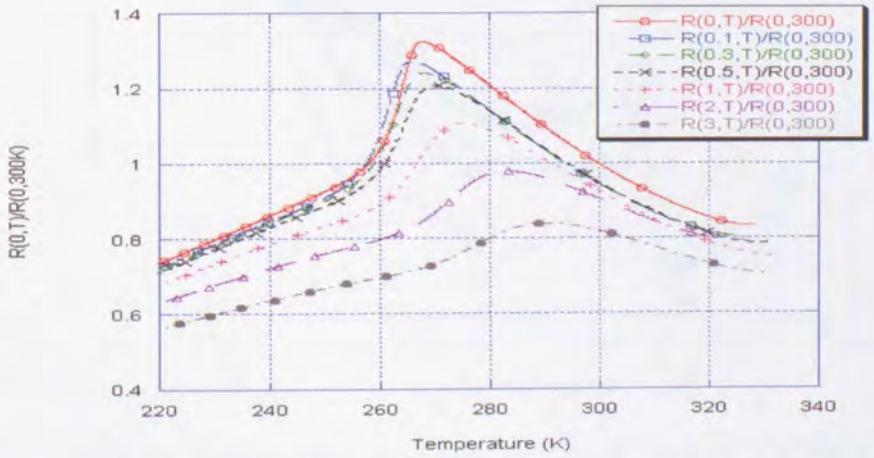

Figure 6-10. Normalized resistance vs. Temperature curves for the "soft" sample near the transition temperature, at different magnetic fields (0, 0.1, 0.3, 0.5, 1, 2, and 3 T).

Careful inspection of the previous two graphs shows that, for both samples, as the applied magnetic field increases the temperature at which the peak occurs (T_c) shifts towards higher temperatures. This is due to magnetic ordering.

The "hard" sample (figure 6-9) exhibits an unusual behavior. At low fields and for some temperature ranges, resistivity increases with increasing field. This is a positive magnetoresistance effect attributed by some researchers to the presence of inhomogeneities.[3] The soft sample produces the standard negative magnetoresistance, i.e. the resistivity at any given temperature decreases as magnetic field increases (see figure 6-10).

The magnetoresistance effect at different fields, defined by equation 6.3, is plotted below (figures 6-11 and 6-12).

$$MR = \frac{R(H=0,T) - R(H,T)}{R(H=0,300K)} \times 100\ \%. \qquad (6.3)$$

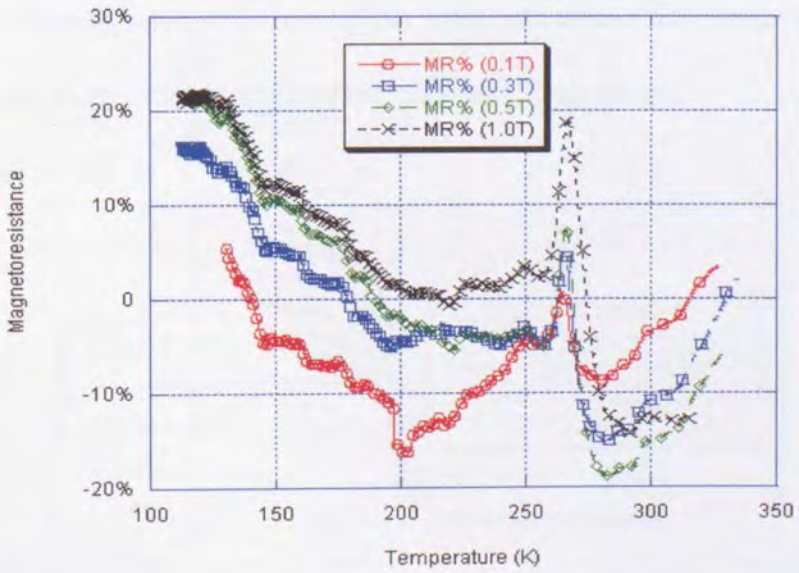

Figure 6-11. MR vs. Temperature curves for the "hard" sample at different magnetic fields (0.1, 0.3, 0.5, and 1 T). Notice the positive magnetoresistance at low fields and for some temperature intervals.

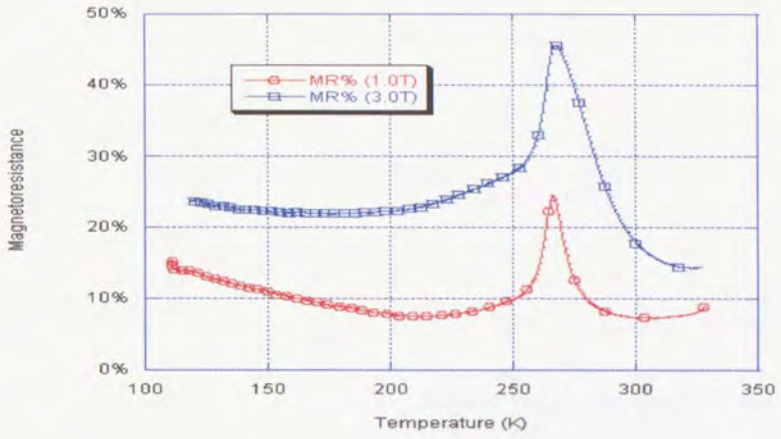

Figure 6-12. MR vs. Temperature curves for the "soft" sample at two magnetic fields. The sample's MR is negative but the percent change is shown as positive in this case.

6.2 CMR in "Soft" and "Hard" Samples of $La_{0.7}Ca_{0.3}MnO_3$ Magnetic Measurements

Using a SQUID magnetometer, the magnetic susceptibility as a function of temperature, at different magnetic fields, was obtained for the soft and the hard samples. The results for the case of the "hard" sample are shown in figure 6-13. These curves clearly show a paramagnetic to ferromagnetic transition at a critical temperature T_c about 280 K, practically independent of the magnetic field applied.

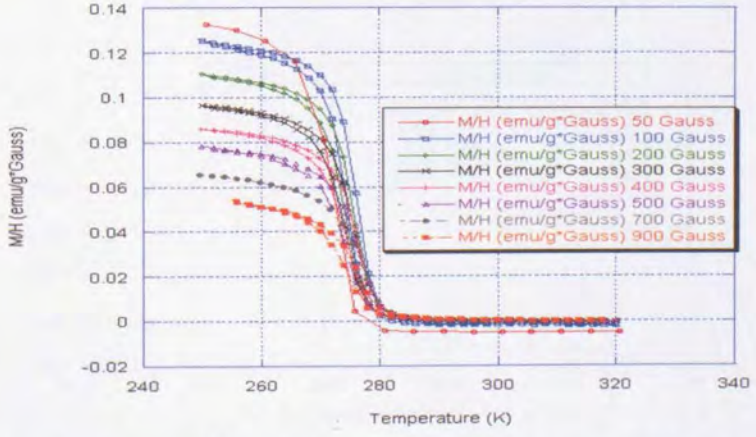

Figure 6-13. Magnetic susceptibility versus temperature curves for the "hard" sample under different magnetic fields.

For each applied magnetic field, the paramagnetic region (above T_c) fits well, the Curie-Weiss law, as given by equation 6.4 .

$$\chi = \frac{C}{(T - T_C)} \tag{6.4}$$

where C is the Curie constant, and T_c the Curie temperature. Figures 6-14 and 6-15 show the paramagnetic susceptibility regions for the hard and the soft samples at 40 mT and 20 mT, respectively, their corresponding best least squares fit to the Curie-Weiss law, and the calculated values for T_c and C.

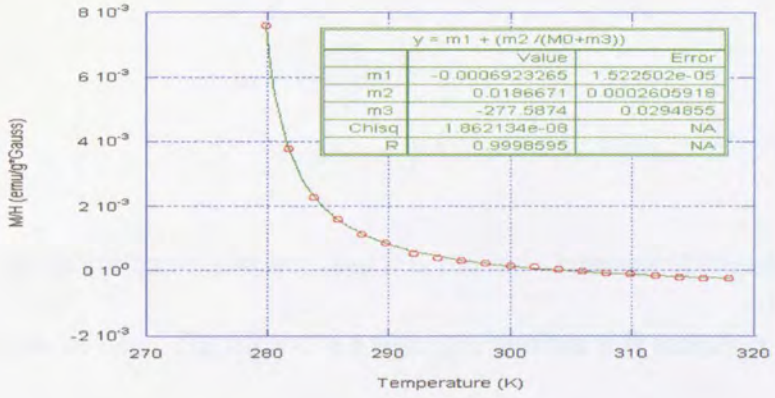

Figure 6-14. Paramagnetic susceptibility vs. temperature at 40 mT for the "hard" sample (red circles). Best least-squares fit to Curie-Weiss law (green line). T_c = 277.5874 K and C = 0.0186671 emu K / g G.

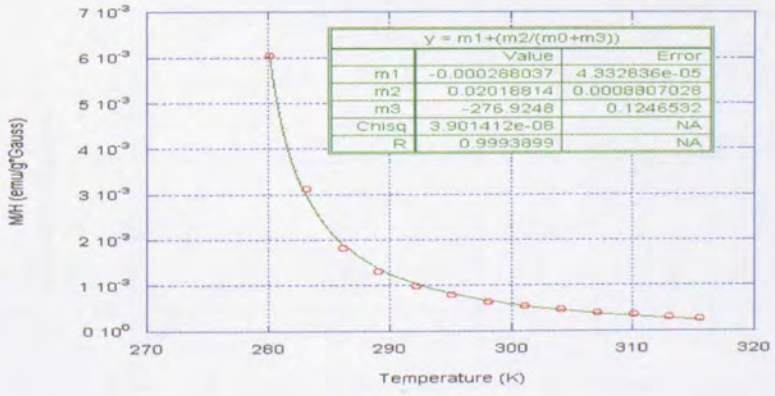

Figure 6-15. Paramagnetic susceptibility vs. temperature at 20 mT for the "soft" sample (red circles). Best least-squares fit to Curie-Weiss law (green line). T_c = 276.9248 K, and C = 0.02018814 emu K / g G.

Several similar best least-squares fit calculations show that the paramagnetic to ferromagnetic transition, for different applied magnetic fields, occurs at a Curie temperature T_c very close to 277 K for both hard and soft samples.

In LaCaMnO samples the only magnetic ion is Mn. The La ion is weakly diamagnetic.[7] Having the experimental values of the Curie constant (C) at different applied magnetic fields, it is possible to calculate the corresponding effective magnetic moments of Mn ions at temperatures above T_c. C and the effective magnetic moment per Mn ion (μ) are related by equation 6.5.

$$\mu = \left(\frac{3Ck_B}{n} \right)^{\frac{1}{2}} \tag{6.5}$$

where k_B is the Boltzmann constant, and n is the ratio between Avogadro's number and the atomic mass of Mn. The effective magneton number p is simply μ divided by the Bohr magneton $\mu_B = eh/4\pi mc = 9.2741 \times 10^{-24} JT^{-1}$. The calculated magneton numbers at different fields are plotted below (figure 6-16).

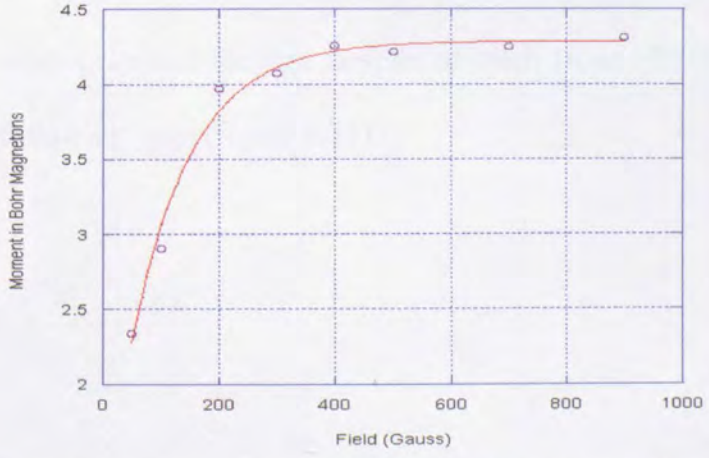

Figure 6-16. Effective magneton number calculated for the "hard" sample vs. magnetic field. Saturation is reached at "high" magnetic fields.

The experimental values of the effective magneton numbers for Mn^{3+} and Mn^{4+} are 5.0 and 4.0, respectively.[7] In an ideal $La_{0.7}Ca_{0.3}MnO_3$ specimen 70% of the Mn ions are Mn^{3+}, the remainder (30%) are Mn^{4+} ions. Thus, it is natural to expect an effective magnetic moment $\mu = (0.7 \times 5.0 + 0.3 \times 4.0)\ \mu_B = 4.7\ \mu_B$ in this type of sample.

Taking into account the effect of weak diamagnetic La^{3+} ions, unavoidable Mn vacancies and porosity of the material, the saturation value for the effective magneton number (4.3), achieved at fields above 40 mT, as shown by the previous graph, is in good experimental agreement with a theoretical value of 4.7.

6.3 Effect of Grain Size and Annealing Atmosphere in $La_{0.7}Ca_{0.3}MnO_3$ Samples

Once the flashing technique was established, and structural stability achieved, the main research goal was to determine the optimum flashing temperature. For this purpose, four samples were prepared, flashed at 1300, 1450, 1525, and 1600°C, and annealed in an O_2 atmosphere. These samples correspond to Batch 14 #1 through #4 in the laboratory record book.

The four samples were analyzed with an electron-microscope at Kingston University.[8] Micrographs of the four samples of batch 14, at 6000X magnification, are shown on the following page (figure 6-17).

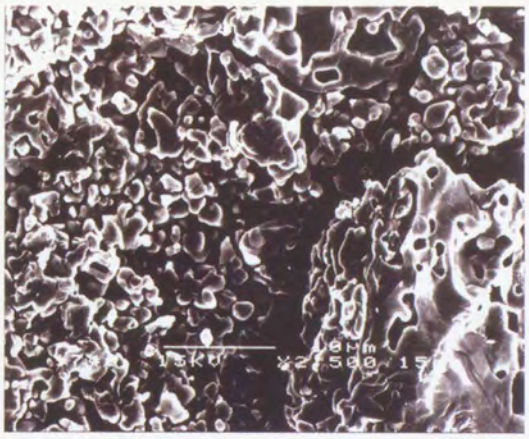

Sample #1. Flashed at 1300°C

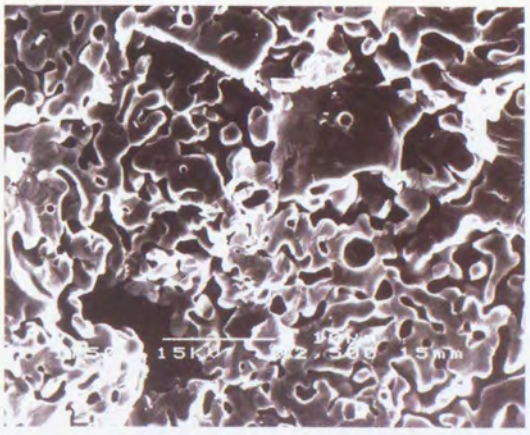

Sample #2. Flashed at 1450°C

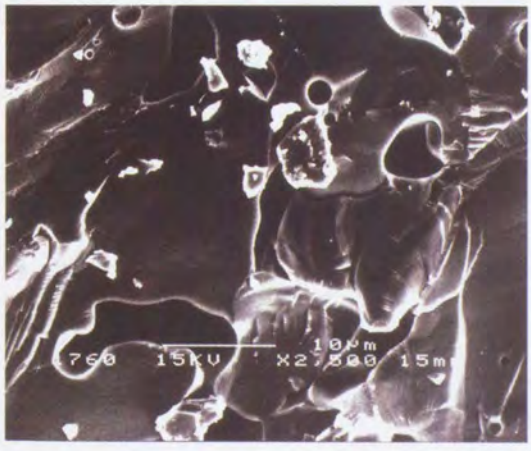

Sample #3. Flashed at 1525°C

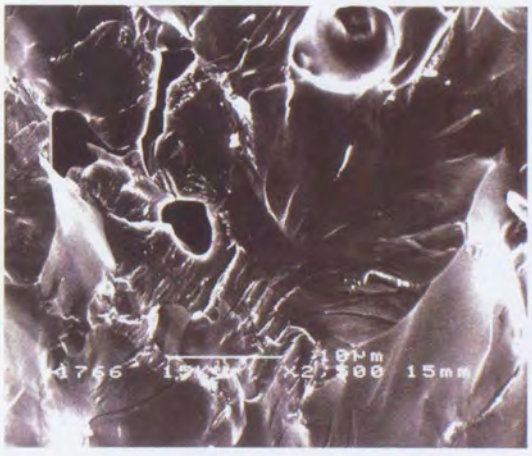

Sample #4. Flashed at 1600°C

Figure 6-17 Micrographs of the four samples of batch 14, at 6000x magnification. The horizontal white line located near the bottom of the images is a scale indicating a 10μm span. These samples were prepared with different flashing temperatures.

Careful inspection of the micrographs shows how the grains fuse more and more as the flashing temperature increases. For samples #1 and # 2, it is possible to estimate average grain sizes of the order of 1.5 and 1.7 to 2.0 μm, respectively. For samples #3 and #4, it is not possible to assign grain sizes.

A simple calculation of the atomic composition for an ideal specimen of $La_{0.7}Ca_{0.3}MnO_3$ gives the following values: 14% La, 6% Ca, 20% Mn, 60% O, and no contamination. After studying four different, representative areas in each sample, the average atomic composition for these specimens was determined. In table 6.2, below, these results are presented and compared to ideal atomic compositions.

Element	Ideal atomic %	Avg. atomic % Sample # 1	Avg. atomic % Sample # 2	Avg. atomic % Sample # 3	Avg. atomic % Sample # 4
La	14	15.35	16.40	15.47	15.40
Ca	6	6.58	6.83	6.39	7.08
Mn	20	20.24	22.14	21.43	27.19
O	60	56.15	54.35	56.59	49.96
Si	0	1.68	0.28	0.12	0.37

Table 6.2. Average atomic compositions for batch 14 samples – Ideal atomic %.

Even though the high purity of the oxides and carbonates of the elements used in the preparation of the samples were thoroughly mixed and sintered several times, some differences between actual and ideal compositions remain. This is mainly due to experimental error during the weighing process with an analytical balance, the presence of small amounts of unreacted material, oxygen vacancies, and the unavoidable but small contamination produced by reaction with the crucible and traces of impurities in the oxides and carbonates used.

Within a reasonable experimental error, the sample composition is close to the ideal. The main contaminant is Si, from the standard high temperature crucible used in the experiments. As table 6.2 shows, the oxygen content of the sample flashed at the

highest temperature is the lowest. This suggests that oxygen vacancies increase at elevated flashing temperatures. The reduction in oxygen concentration reduces T_c as shown in resistivity vs. temperature graphs below.

Using the van der Pauw method, electrical resistivity as a function of temperature was determined, with and without an applied magnetic field of the order of 350 mT. These results are shown in figures 6-18 through 6-21.

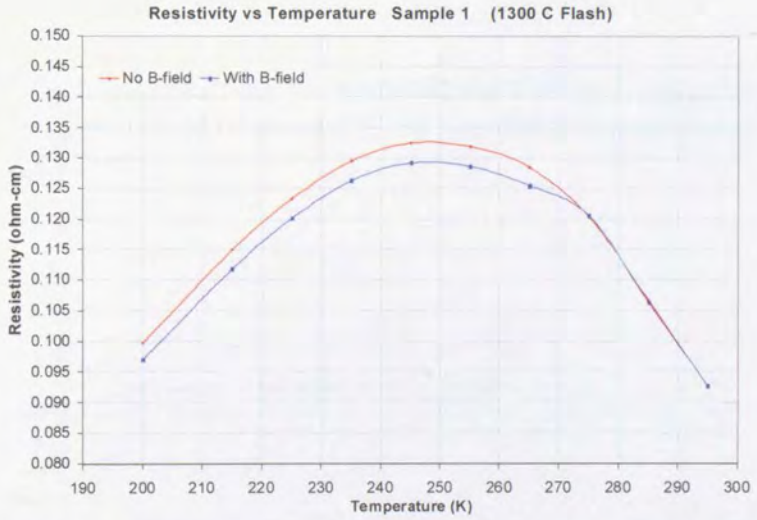

Figure 6-18. Electrical resistivity vs. temperature, with and without an applied magnetic field of about 350 mT, for Batch 14, sample #1, flashed at 1300° C.

Figure 6-19. Electrical resistivity vs. temperature, with and without an applied magnetic field of about 350 mT, for Batch 14, sample #2, flashed at 1450° C.

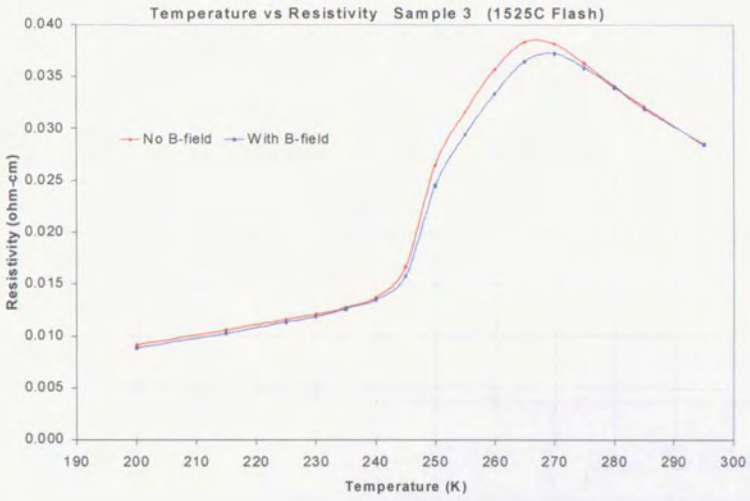

Figure 6-20. Electrical resistivity vs. temperature, with and without an applied magnetic field of about 350 mT, for Batch 14, sample #3, flashed at 1525° C.

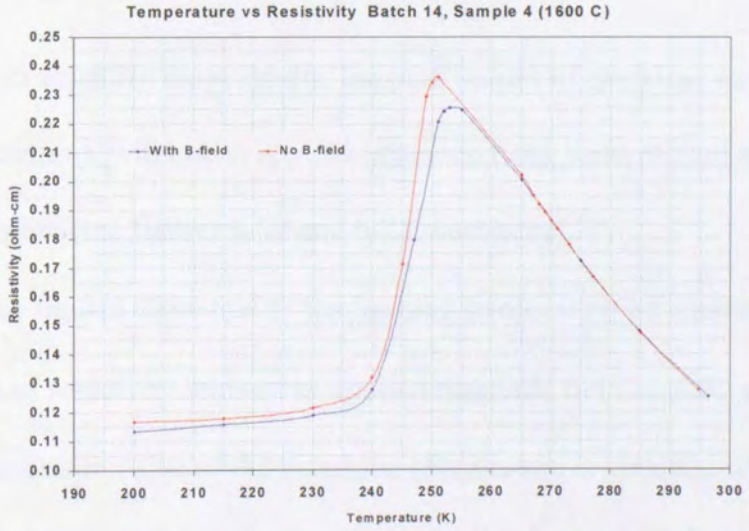

Figure 6-21. Electrical resistivity vs. temperature, with and without an applied magnetic field of about 350 mT, for Batch 14, sample #4, flashed at 1600° C.

In all of these cases, the insulator to metal transition was observed at a critical temperature T_c. The main results of the resistivity vs. temperature experiments are summarized in table 6.3, where $T_c(0)$, $T_c(B)$, $\rho_{max}(0)$, and $\rho_{max}(B)$ represent transition temperatures and peak electrical resistivity values with and without an applied magnetic field B. $T_{flashing}$ is the flashing temperature.

Sample #	$T_C(0)$ (K)	$T_C(B)$ (K)	ρ_{max} (0)(Ω-cm)	ρ_{max} (B) (Ω-cm)	$T_{flashing}$ (C)
1	248	248	0.133	0.130	1300
2	271	273	0.061	0.058	1450
3	266	269	0.039	0.037	1525
4	251	253	0.236	0.226	1600

Table 6.3. Summary of some experimental results for the four samples of Batch 14.

In order to visualize these results, the peak values of electrical resistivity and the transition temperatures, without an applied magnetic field, were plotted as a function of flashing temperature (see figures 6-22 and 6-23, next page).

These two figures show that as the flashing temperature increases to 1525°C, the maximum value of resistivity without an applied magnetic field $\rho_{max}(0)$, decreases. Also, that the maximum value of the transition temperature is obtained with a flashing temperature of 1450°C. From these graphs, it can be seen that there is an optimum flashing temperature range for which the transition temperature is greatest and for which the electrical resistivity is lowest. These effects are due to the increase in grain size as flashing temperature increases. At temperatures above this ideal range, the material begins to melt and becomes an insulator.

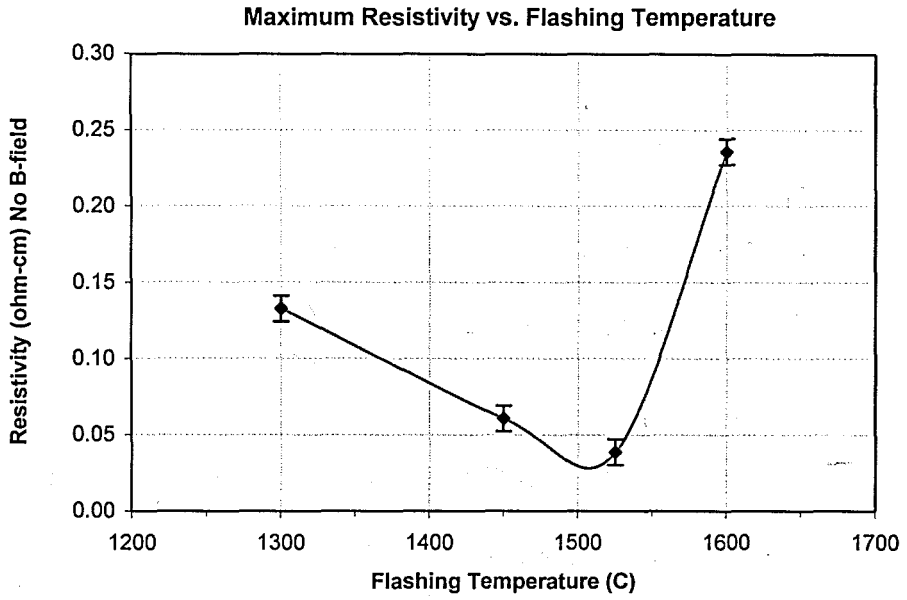

Figure 6-22. Peak values of electrical resistivity, without an applied magnetic field, $\rho_{max}(0)$ vs. flashing temperature.

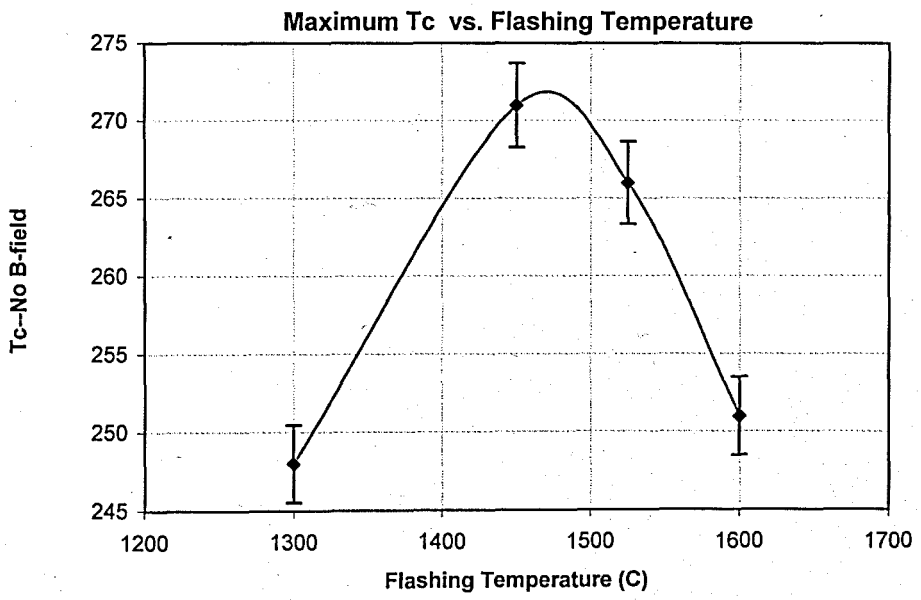

Figure 6-23. Insulator – metal transition temperature, without an applied magnetic field, vs flashing temperature.

A new and interesting result discussed in this chapter is the positive magneto-resistance observed, and verified for different applied magnetic fields, in the "hard" sample. After observing the magneto-resistance of the hard samples, other researchers suggest that the combination of pelletizing pressure, flashing temperature, and annealing environment used with these samples, produced inhomogeneities that caused the observed positive magnetoresistance.[3] This could be the subject of future investigations.

From the analysis of the four samples pelletized at a pressure of 6.7×10^8 Pa and different flashing temperatures (Batch 14), an optimal flashing at 1450°C was determined. This flashing temperature produces a low electrical resistivity and a high transition temperature (see figures 6-22 and 6-23).

References

1. Correlation between Heat Treatment, Resistivity and Magnetoresistance in Poly-crystalline samples of $La_{0.7}C_{0.3}MnO_3$, Presentation during the annual meeting of the American Physical Society. March 2002. **Javier Estrada, Jerry Brower**, Grand Valley State University, Physics Depart., Allendale , MI 49401. **Vincent Montgomery**, Kingston University, Chemistry Depart., Kingston-upon-Thames, Surrey, UK.

2. Characterization of Ca doped Manganite Samples Prepared Using a Modified Solid State Reaction Technique. Timir Datta, Michael Bleiweiss, Superconductivity Inst. University of South Carolina, Columbia, SC 29208. **Jerry Brower, Javier Estrada**, Physics Department, Grand Valley State University, Allendale, MI 49401. **Vincent Montgomery**, Chemistry Department, Kingston University, Kingston-upon-Thames, Surrey, U.K.

3. Michael Bleiweiss, Ph. D. Dissertation (University of South Carolina, Columbia, SC 2003). Dr. Timir Datta, advisor.

4. S. L. Yuan, J. Q. Li, Y. Jiang, Y. P. Yang, X. Y. Zeng, G. Li, F. Tu, G. Q. Zhang, C. Q. Tang, and S. Z. Jin, Phys. Rev. B 62, 5313 (2000).

5. M. Jaime and M. B. Salamon, Physics of Manganites, edited by T. A. Kaplan and S. D. Mahanti (Kluwer Academic Press, New York, 1999).

6. M. Jaime, P. Lin, M. B. Salamon, and P. D. Han, Phys. Rev. B 58, R5901 (1998).

7. N. W. Ashcroft and N. D. Mermin, Solid State Physics, Saunders College Publishing, 1976. Tables 31.3 and 31.4.

8. Electron Microscope Laboratory (WB 35), Bill Edwards, Kingston University, Kingston-upon-Thames, Surrey, U.K.

Chapter 7

Iron Doped Manganites - Experimental Results – Analysis

7.1 Introduction

Many experiments in the partial substitution of Mn in Ca doped manganites have been performed.[1,2] In particular, Fe substitutions with a generic formula $La_{0.7}Ca_{0.3}(Mn_{1-x}Fe_x)O_3$.[3] Although the results of several of these experiments are very interesting, they do not address the problem of the structural stability of the samples.

Once again, the initial experience in the preparation of Ca and Fe doped manganites was similar to the preparation of Ca doped samples. Without the flashing technique explained before, the samples crumbled after a few days. Therefore, the final experimental goal of this research project was the preparation of structurally sound iron doped manganites, their characterization, the analysis of the experimental results, and the comparison with results obtained by other researchers.

The iron doping of manganites is particularly interesting for two reasons: First, the ionic radii of Fe^{3+} and Mn^{3+} are very similar (0.64 and 0.66 Å, respectively)[4] ; this fact reduces the lattice effect of iron doping in manganites to a minimum. Second, among the "3d" ions or iron group ions, Fe^{3+} and Mn^{2+} share the highest experimental magneton number (see table 7-1).[5] Therefore, a strong influence of the relatively high magnetic moment of Fe^{3+} on the electrical conductivity and on the paramagnetic-ferromagnetic transition temperature of iron doped manganites is expected.

7.2 Results and Analysis

Previous experiments in Fe doping of manganites showed that for levels between zero and 8% Fe, typical CMR electrical resistivity vs. temperature curves are obtained, with transitions decreasing in temperature at about 22 K for each 1% Fe doping (see figure 7-1, adapted from J.R. Sun, et al [3]). For doping levels above 8% Fe, the electrical resistivity increases steadily as temperature decreases (the typical behavior of semiconductors) and no transition to a metallic state is observed.

ION	CONFIGURATION	BASIC LEVEL	MAGNETON # *
Ti^{3+}, V^{4+}	$3d^1$	$^2D_{3/2}$	1.8
V^{3+}	$3d^2$	$^3F_2$	2.8
Cr^{3+}, V^{2+}	$3d^3$	$^4F_{3/2}$	3.8
Mn^{3+}, Cr^{2+}	$3d^4$	$^5D_0$	4.9
Fe^{3+}, Mn^{2+}	$3d^5$	$^6S_{5/2}$	5.9
Fe^{2+}	$3d^6$	$^5D_4$	5.4
Co^{2+}	$3d^7$	$^4F_{9/2}$	4.8
Ni^{2+}	$3d^8$	$^3F_4$	3.2
Cu^{2+}	$3d^9$	$^2D_{5/2}$	1.9

* Experimental values

Table 7-1. Effective Magneton Numbers for the Iron Group Ions

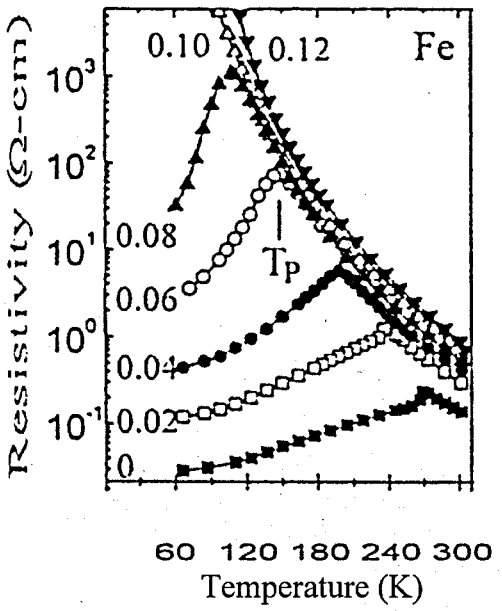

Figure 7-1. Electrical resistivity vs. Temperature for iron doped manganites. Curves for 2, 4, 6, and 8% Fe substitution are shown.[3]

A careful look at figure 7-1 shows that the 5 and 7% Fe doping levels - not present – would be ideal to compare electrical resistivity values and transition temperatures with those found in the experiment by J.R. Sun and his group.[3]

Except for the addition of iron oxide (Fe_2O_3) in appropriate proportions, the preparation technique followed for Ca and Fe doped manganite samples $La_{0.7}Ca_{0.3}Mn_{1-x}Fe_xO_3$, was the same as the one used in the preparation of Ca doped manganites, explained in chapter 5.

Two 5% Fe doped pellets ($La_{0.7}Ca_{0.3}Mn_{1-0.05}Fe_{0.05}O_3$) were prepared. To increase inter-grain contact, a pressure of 6.7×10^8 Pa was used to produce 13mm-diameter pellets. These pellets were "flashed" at 1250°C and 1500°C, respectively, for a period of 10 minutes. The pellets were labeled Batch 15, samples #1and #2, respectively. The last step in the sample preparation was the annealing in an O_2 atmosphere from 850°C to room temperature, during a time interval of 48 hours.

After several months of environmental exposure, no visible sign of structural deterioration was observed in either sample.

Using the well known van der Pauw technique (see chap. 3, pg. 63 and apdx B, pg iv) and data obtained from the experimental measurements of the samples, the electrical resistivity as a function of temperature, with and without the application of a magnetic field of the order of 350 mT, was calculated for the 5% Fe doped samples. Plots for the two samples are shown in figures 7-2 and 7-3.

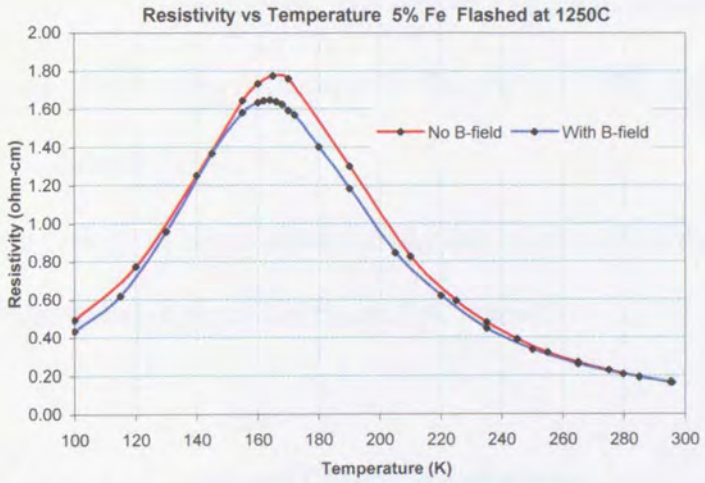

Figure 7-2. Electrical resistivity vs. Temperature, with and without an applied magnetic field of 350 mT, for 5% Fe doped manganite flashed at 1250°C (Batch 15, sample #1).

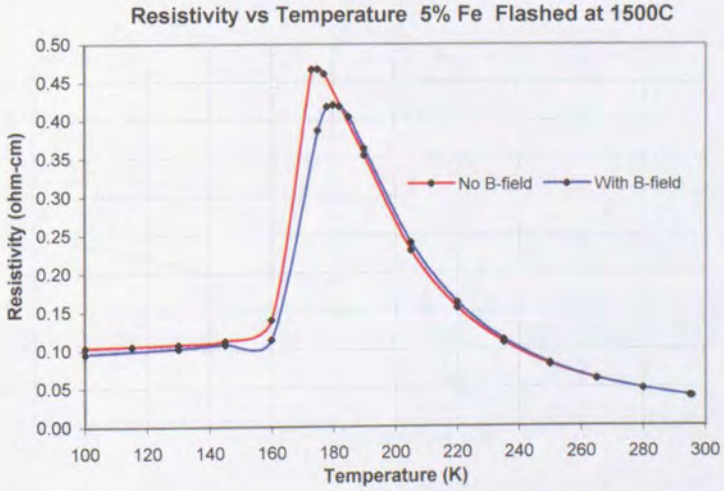

Figure 7-3. Electrical resistivity vs. Temperature, with and without an applied magnetic field of 350 mT, for 5% Fe doped manganite flashed at 1500°C (Batch 15, sample #2).

As revealed by detailed inspections of the previous two graphs, the sample annealed at 1500°C (sample #2) is almost four times less resistive than the one annealed at 1250°C (sample #1). This is clearly an effect produced by grain size and grain fusion, as the following electron-microscope micrographs in figure 7-5 show. Furthermore, the transition temperatures (T_c) with and without an applied magnetic field are practically the same for sample #1. For sample #2, T_c with an applied magnetic field is a little higher than the transition temperature without it (about 180 K, compared to 173 K). At the transition temperatures, the percent change in resistivity is greater for sample #2 flashed at 1500°C than for sample #1 flashed at 1250°C (10% for sample #2, compared to 7% for sample #1).

The percent change in electrical resistivity due to an applied magnetic field of 350 mT was calculated and is plotted in figure 7-4, below.

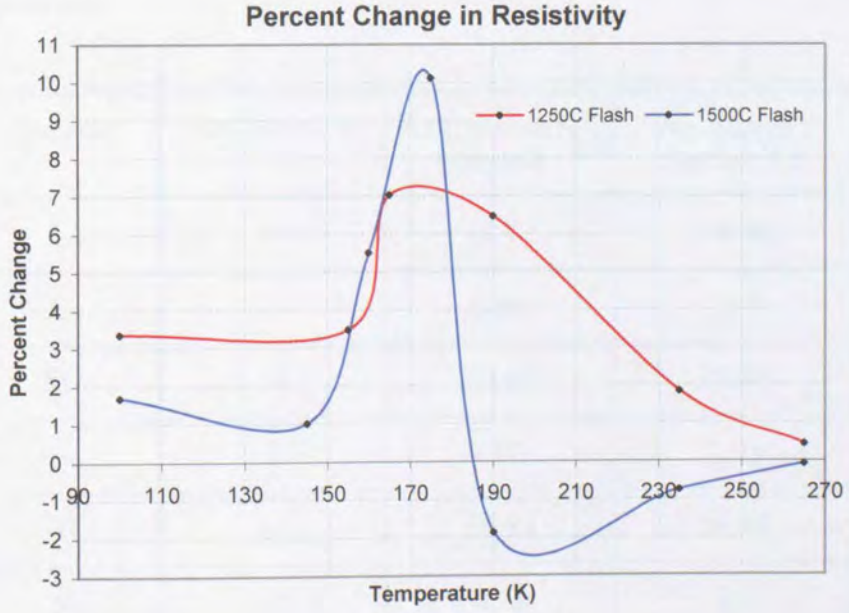

Figure 7-4. Percent change in resistivity vs. temperature for 5% Fe doped samples (Batch 15, #1 and #2) with an applied magnetic field of 350 mT.

Some of the experimental results for samples of batch 15 are summarized in table 7-2.

Sample number	Flashing temp. (C)	$T_c(0)$(K)	T_c(B)(K)	$\rho_{max}(0)$ (Ω-cm)	ρ_{max}(B) (Ω-cm)	% change in MR
1	1250	165	165	1.80	1.63	7 %
2	1500	173	180	.45	.40	10 %

Table 7-2

Using an electron-microscope, an average atomic composition for the two samples of batch 15 was determined and micrograph pictures at different magnifications were taken.[6] A calculation of the atomic composition of an ideal specimen of $La_{0.7}Ca_{0.3}Mn_{0.95}Fe_{0.05}O_3$ gives the following values: 14% La, 6% Ca, 19% Mn, 1% Fe, 60% O, and no contamination. Notice that a 5% atomic substitution of Fe for Mn results in a 1% Fe content in the specimen. After studying different, representative areas in each sample, the average atomic composition for these specimens was determined. In table 7-3, below, these results are presented and compared to ideal atomic compositions.

Element	Ideal atomic %	Avg. atomic % Sample # 1	Avg. atomic % Sample # 2
La	14	14.92	14.54
Ca	6	6.96	7.18
Mn	19	20.98	20.80
Fe	1	1.00	1.05
0	60	56.83	56.46
Si	0	0.18	0.0

Table 7-3. Atomic compositions, actual and ideal, for batch 15 samples.

Even though the high purity* oxides and carbonates of the elements used in the preparation of the samples were thoroughly mixed and sintered several times, some differences between actual and ideal compositions remain. This is mainly due to experimental error during the weighing process with an analytical balance, the presence of small amounts of un-reacted material, oxygen vacancies, the unavoidable but small contamination produced by reaction with the crucible, and traces of impurities in the oxides and carbonates used in the preparation.

Within a reasonable experimental error, the sample composition is close to the ideal. The main contaminant is Si, from the standard high temperature crucible used in the experiments. As table 7-3 shows, the oxygen content of the two Fe doped samples, flashed at different temperatures, is practically the same. There is no correlation, in this case, between oxygen content and the small difference in transition temperature.

Micrographs of the two samples of batch 15, at 6000X magnification, are shown together for comparison purposes on the following page (figure 7-5). As observed in the case of Ca doped manganites, careful inspection of these micrographs shows how the grains fuse more and more as the flashing temperature increases. While for sample #1 it possible to estimate an average grain sizes of the order of 2.0 μm, for sample #2 it is not possible.

* (La_2O_3) 99.99%, ($CaCO_3$) 99.95%, (Fe_2O_3) 99.97%, (MnO_2) 99.999%

Sample #1

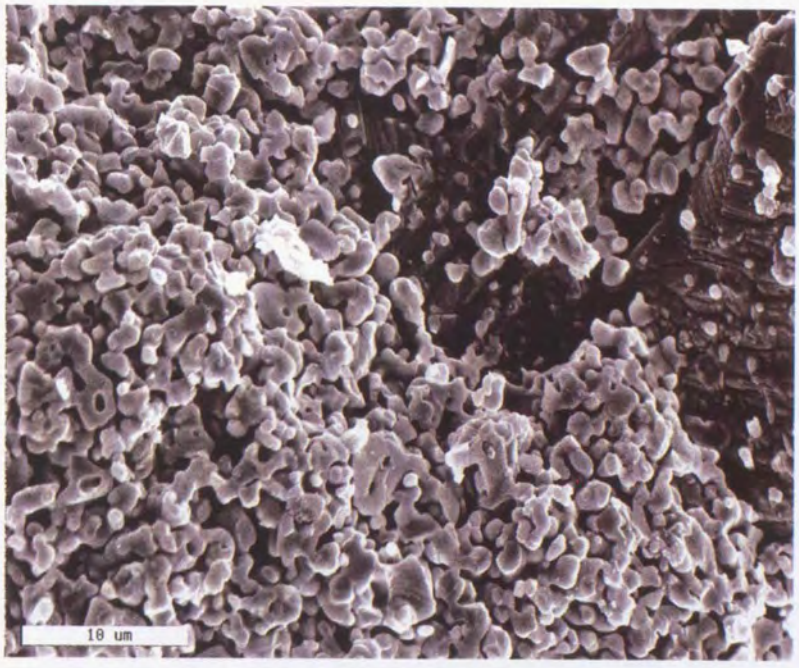

Sample #2

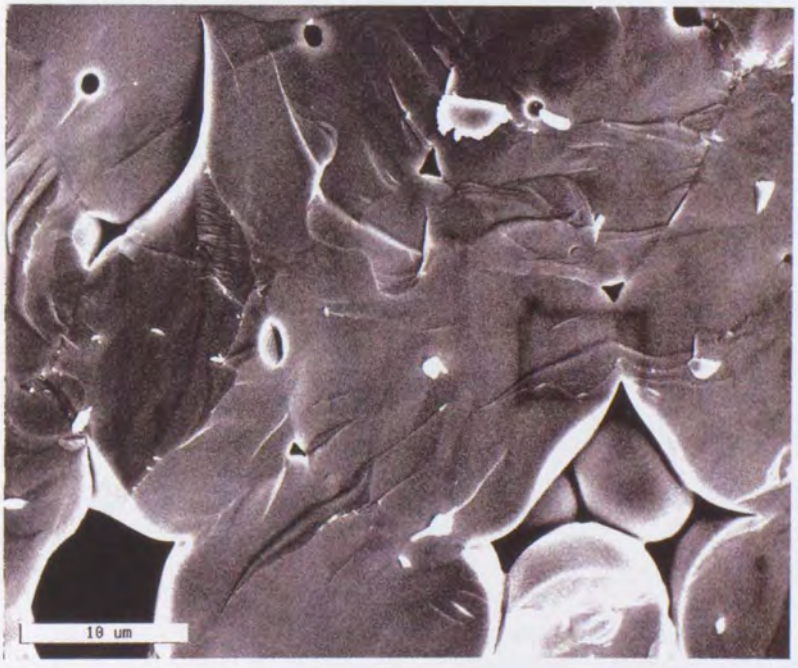

Figure 7-5 Micrographs, under the same magnification, for 5% Fe doped manganite samples, in order of increasing flashing temperature (1250°C and 1500°C - Batch 15, Sample #1 and Sample #2, respectively).

Since the maximum magnetoresistive effect and the minima values of electrical resistivity for the 5% Fe doped samples occurred at a flashing temperature of 1500°C, this flashing temperature was used in the preparation of 7% Fe doped samples. The samples were flashed for 15 minutes. In order to investigate the effect of different pelletizing pressures and annealing atmospheres, six 7% Fe doped samples were prepared by the solid-state reaction technique previously discussed.

These pellets were pressed in pairs with pelletizing pressures of 0.67×10^8, 3.3×10^8 and 6.7×10^8 Pa, respectively. One of each of the pellet pairs was annealed in air and the other one of the pair was annealed in an oxygen atmosphere. During the oxygen annealing process the samples were slowly cooled down from 800°C to 300°C over a period of 30 hours. The temperature was decreased to room temperature over a period of 4 hours. As with previous manganite samples, the electrical resistivity as a function of temperature was calculated for the six 7% Fe doped samples. The corresponding plots are shown in figures 7-6 through 7-11. For comparison and convenience, these plots are shown in their respective pairs, on the following pages.

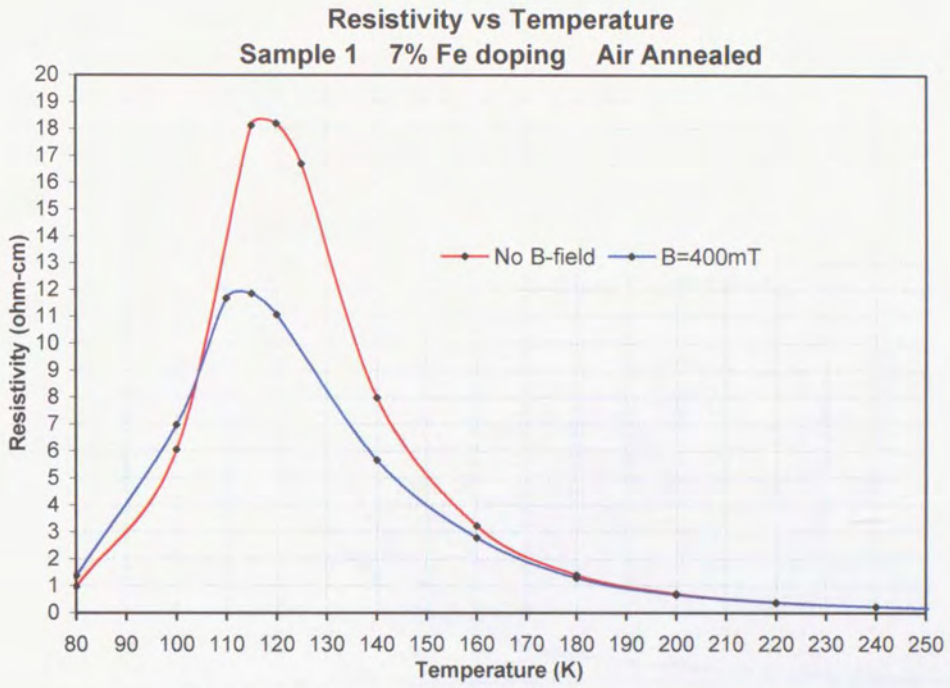

Figure 7-6. Sample 1, 7% Fe, air annealed, 0.67 x 10^8 Pa pelletizing pressure.

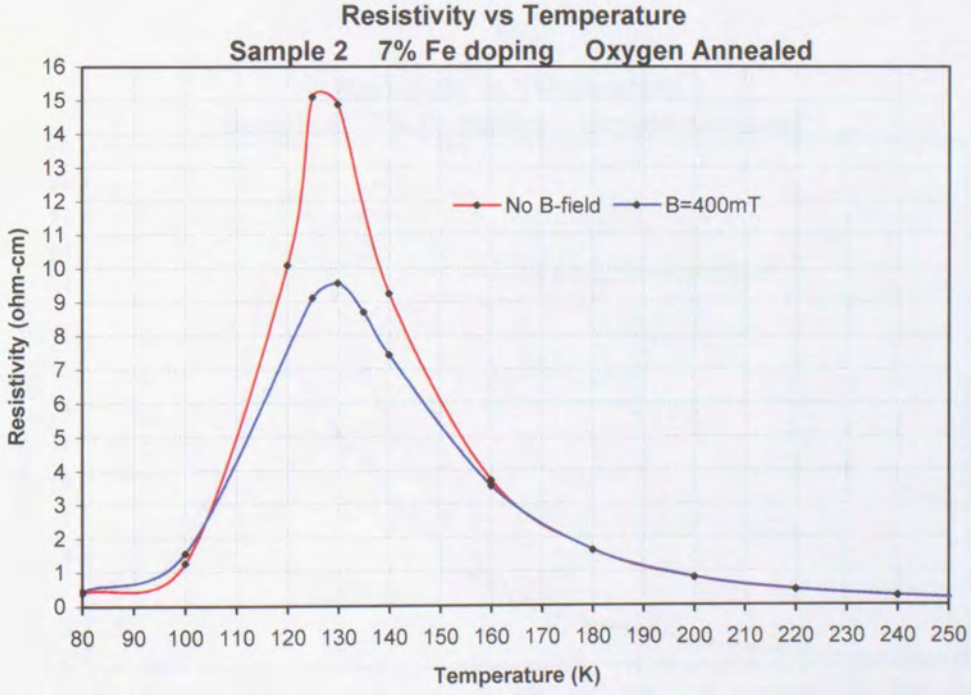

Figure 7-7. Sample 2, 7% Fe, oxygen annealed, 0.67 x 10^8 Pa pelletizing pressure.

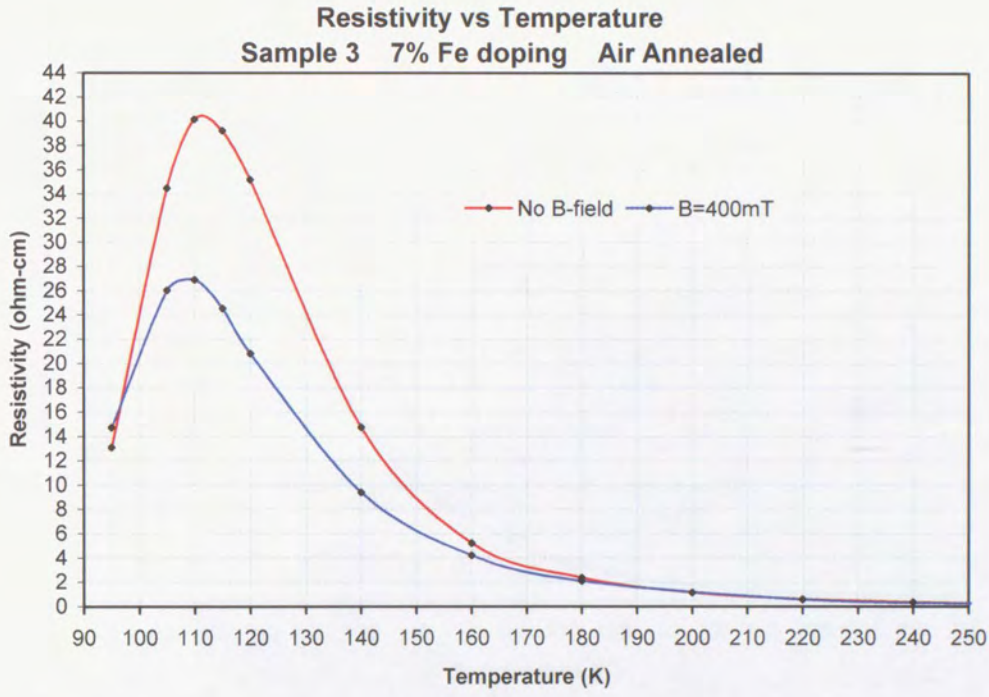

Figure 7-8. Sample 3, 7% Fe, air annealed, 3.3 x 10^8 Pa pelletizing pressure.

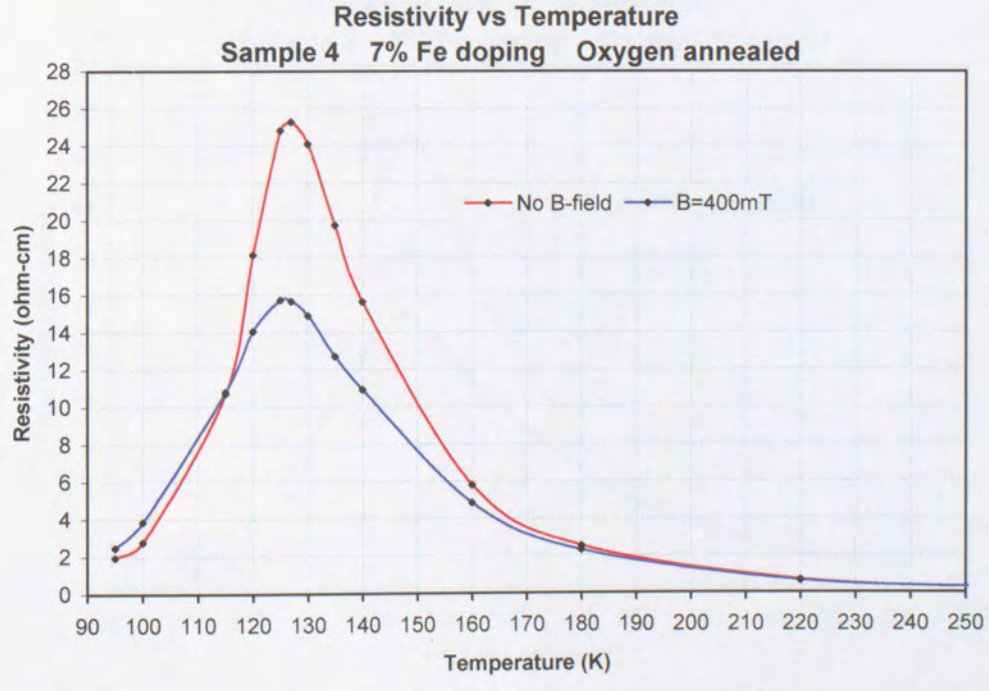

Figure 7-9. Sample 4, 7% Fe, oxygen annealed, 3.3 x 10^8 Pa pelletizing pressure.

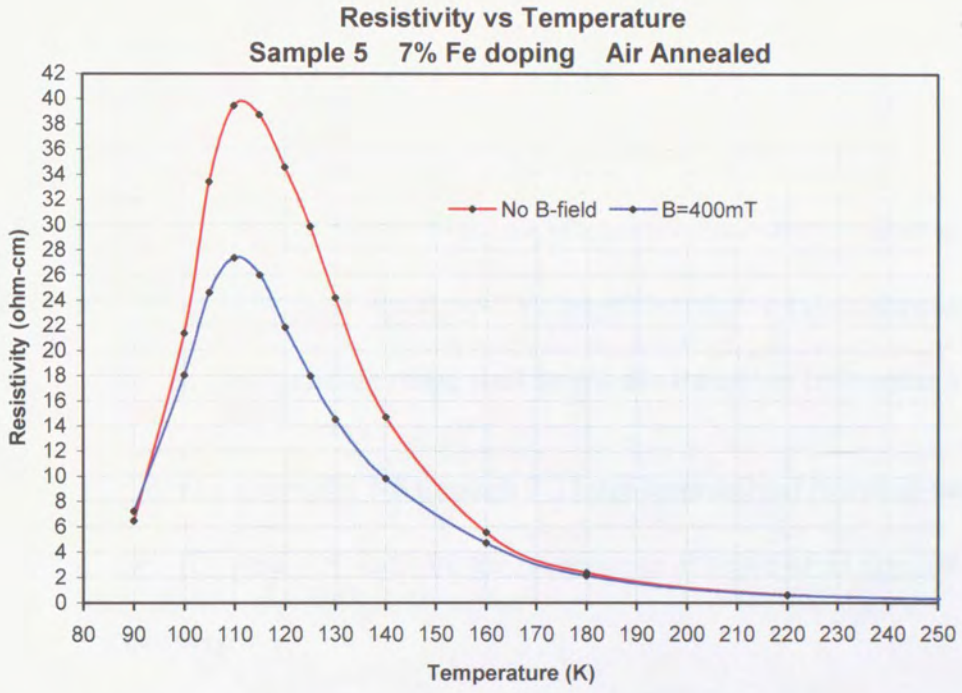

Figure 7-10. Sample 5, 7% Fe, air annealed, 6.7 x 10^8 Pa pelletizing pressure.

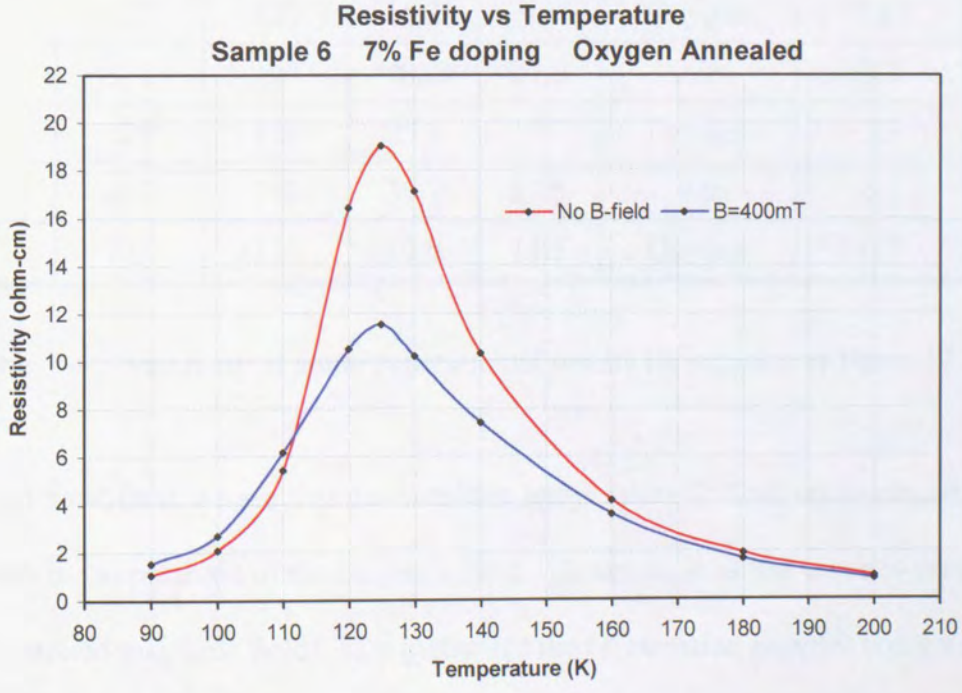

Figure 7-11. Sample 6, 7% Fe, oxygen annealed, 6.7 x 10^8 Pa pelletizing pressure.

In the case of sample 1 (7% Fe, 0.67 x 10^8 Pa, air annealed) there is a slight positive magnetoresistance effect in the temperature range between about 80 K - 105 K. This positive magnetoresistance effect, as mentioned before, has been attributed by some researchers to the presence of inhomogeneities.[7] The rest of the samples of batch 17 (samples 2 through 6) show the normal negative magnetoresistance over most of the studied temperature range. The same small positive magnetoresistive effect appeared in these last five samples in a temperature range well below the transition temperature.

Other results shown in graphs 7-6 through 7-11 are summarized below in table 7- 4. The parentheses (B) and (0) indicate the presence or absence of an applied magnetic field, respectively.

Sample number	$T_c(0)$(K)	$T_c(B)$(K)	$\rho_{max}(0)$ (Ω-cm)	$\rho_{max}(B)$ (Ω-cm)	Annealing atmosphere	Pressure (10^8 Pa)
1	117	112	18.6	12.0	Air	0.67
2	127	129	15.2	9.6	Oxygen	0.67
3	112	109	40.2	27.0	Air	3.3
4	127	126	25.3	15.7	Oxygen	3.3
5	112	111	39.7	27.5	Air	6.7
6	125	125	19.0	11.5	Oxygen	6.7

Table 7-4. Summary of some experimental results for samples of Batch 17.

From these data, we see that the transition temperature T_c does not necessarily increase with the application of the magnetic field. However, in all the cases (with and without an applied magnetic field), T_c is higher for the O_2 annealed samples compared to T_c for the air annealed samples. As shown in table 7-5 on the following page, the percent difference in the magnetoresistance at the transition temperature, defined as

$$\% \text{ difference} = \left[\frac{\rho_{max}(0) - \rho_{max}(B)}{\rho_{max}(0)} \right] \times 100, \qquad (7.1)$$

is higher when the sample is annealed in oxygen. Also, there is approximately a 1.3% difference in magnetoresistance for the 0.67 x10^8 Pa pelletizing pressure and approximately an 8.8% difference for the 6.7 x 10^8 Pa pelletizing pressure.

Sample number	ρ_{max} (0) (Ω- cm)	ρ_{max} (B) (Ω- cm)	Percent difference	Annealing atmosphere	Pressure (10^8 Pa)
1	18.6	12.0	35.5%	Air	0.67
2	15.2	9.6	36.8%	Oxygen	0.67
3	40.2	27.0	32.8%	Air	3.3
4	25.3	15.7	37.9%	Oxygen	3.3
5	39.7	27.5	30.7%	Air	6.7
6	19.0	11.5	39.5%	Oxygen	6.7

Table 7-5 Percent Magnetoresistance Difference at T_c.

The percentage change in magnetoresistance for the whole temperature range in this experiment was calculated for samples prepared under maximum pressure (samples #5 and #6) and is shown in figure 7-12.

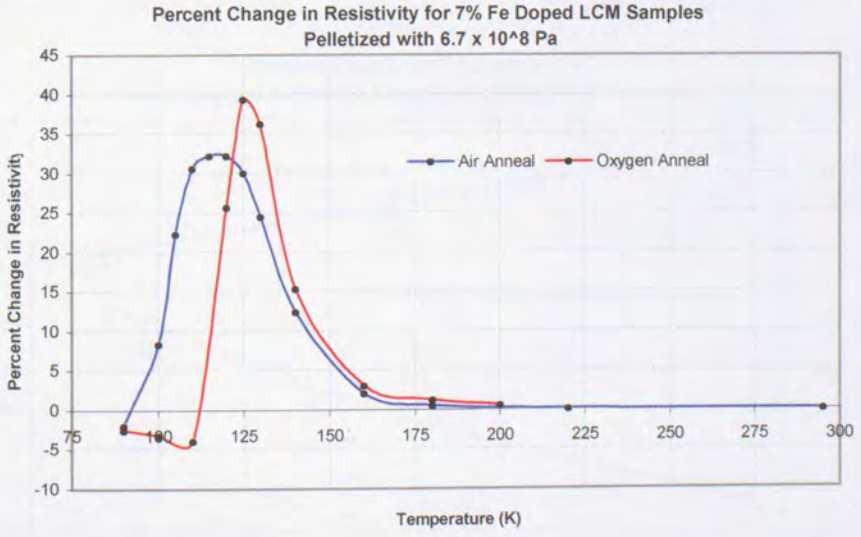

Figure 7-12 Percent change in resistivity for samples #5 and #6.

The results of the analysis of the six pellet samples show clearly that both pelletizing pressure and oxygen annealing affect the magnetoresistive properties. When annealed in air, the samples exhibit a decrease in magnetoresistance as the pelletizing pressure is increased. The oxygen annealed samples, however, exhibit an increase in magnetoresistance at the transition temperature, as the pelletizing pressure is increased. These effects are illustrated in the two graphs, figures 7-12 and 7-13).

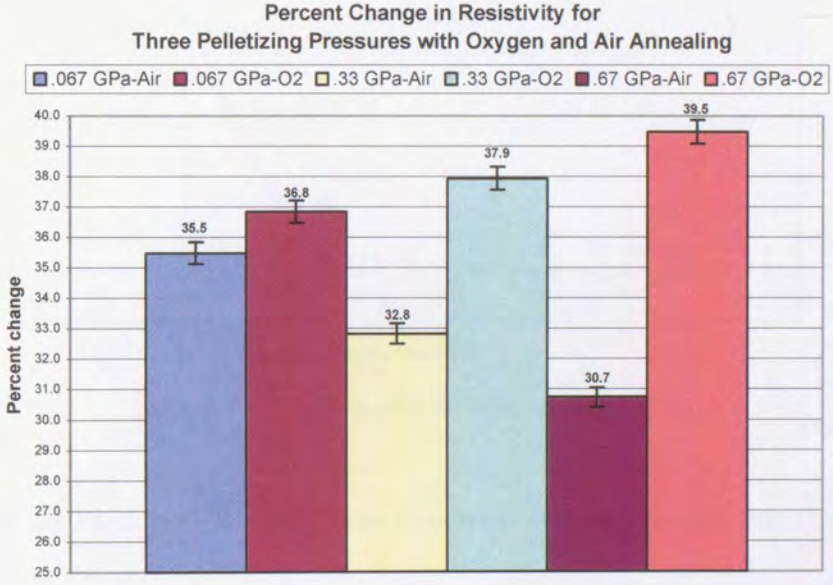

Above, figure 7-12

Below, figure 7-13

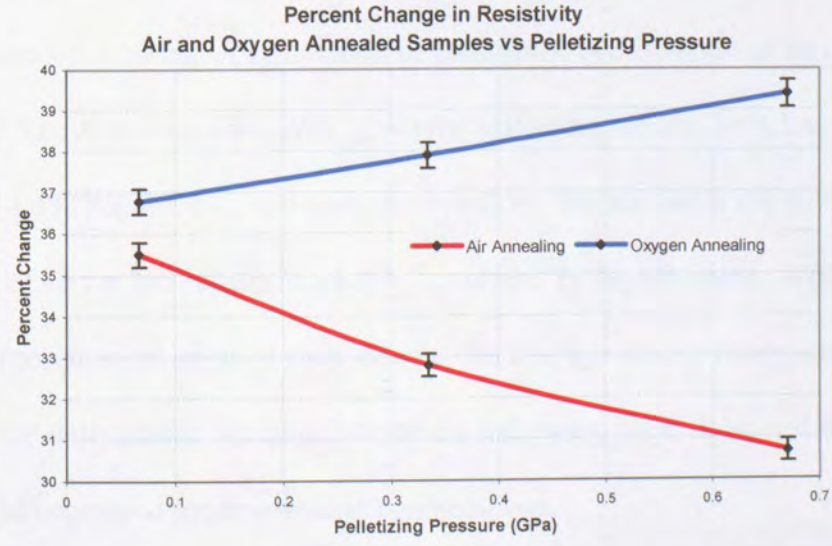

To illustrate the extremes in the magnetoresistive properties of the samples tested, pellets #5 and #6 and pellet #1 from batch 15 were selected. The following graph (figure 7-14) shows the percent change in resistivity for the three pellet samples.

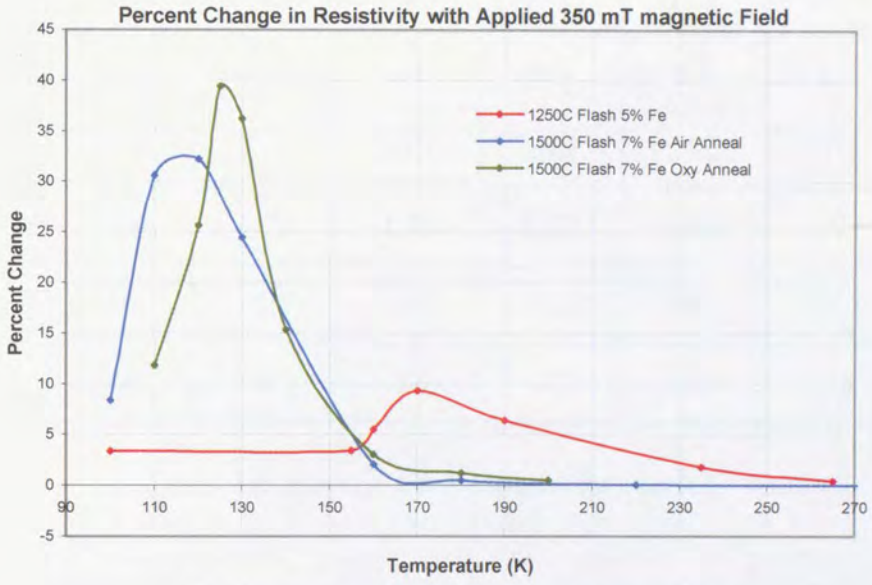

Figure 7-14 Percent change in resistivity.

These six Fe-doped samples were also analyzed with an electron microscope by Mr. Bill Edwards at Kingston University. An average atomic composition for the samples of batch 17 was determined, and micrograph pictures at different magnifications were taken. A calculation of the atomic composition of an ideal specimen of $La_{0.7}Ca_{0.3}Mn_{0.93}Fe_{0.07}O_3$ gives the following values: 14% La, 6% Ca, 18.6% Mn, 1.4% Fe, 60% O, and no contamination. Notice that a 7% atomic substitution of Fe for Mn results in a 1.4% Fe content in the specimen. After studying different, representative, areas in each sample, the average atomic composition for these specimens was determined. In table 7-6, on the following page, these results are presented and compared to ideal atomic compositions.

Element	Ideal atomic %	Avg. Atomic % Sample 1	Avg. Atomic % Sample 2	Avg. atomic % Sample 3	Avg. atomic % Sample 4	Avg. atomic % Sample 5	Avg. atomic % Sample 6
La	14	15.5	16.1	15.7	16.2	15.8	15.5
Ca	6	6.7	6.8	6.8	6.8	6.7	6.9
Mn	18.6	20.4	20.7	20.7	21.2	20.6	20.4
Fe	1.40	1.78	1.76	1.52	1.55	1.74	1.62
0	60	55.7	54.7	55.2	54.1	55.1	54.8
Si	0	0	.24	.12	.13	.18	.21

Table 7-6. Atomic compositions for batch 17 samples.

As in the case of 5% Fe-doped samples, even though high quality oxides and carbonates were used, and careful preparation techniques were followed, some differences between actual and ideal compositions remained. This is attributed to unavoidable contamination from crucibles and impurities in the precursor materials used.

Within a reasonable experimental error, the sample composition is close to the ideal. The main contaminant is Si, from the standard high temperature crucible used in the experiments. As table 7-6 shows, the oxygen content of the 7% Fe doped samples is practically the same. There is no correlation, in this case, between oxygen content and the small difference in transition temperatures.

Micrographs of the six samples of batch 17, at 6000X magnification are, for convenience, shown together on the following page (figure 7-15).

(1)

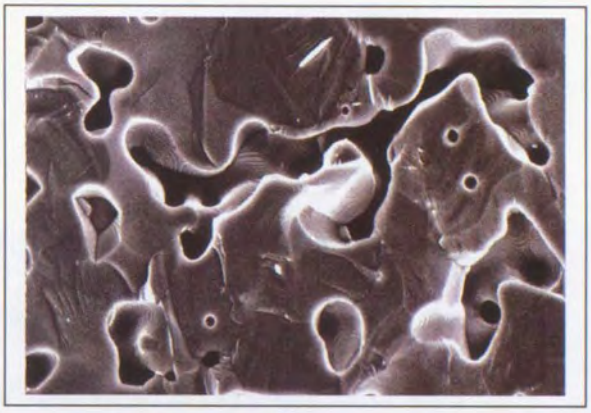

(2)

(3)

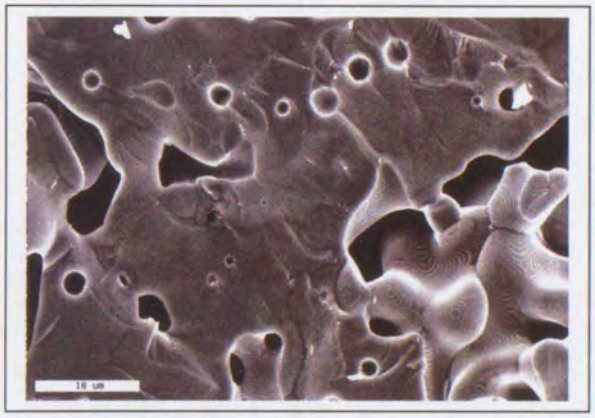

(4)

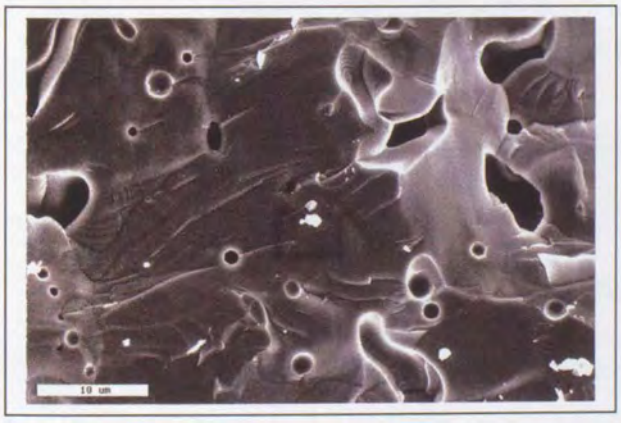

(5)

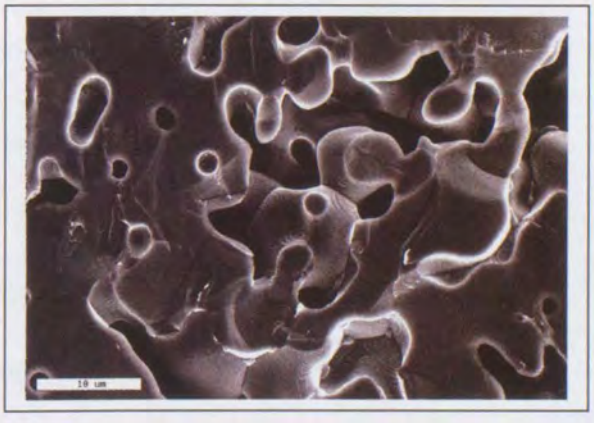

(6)

Figure 7-15. Micrographs of the six samples of batch 17, at 6000X magnification.

While on first examination, these micrographs appear to be quite similar, a careful inspection using the included 10 μm scales reveals larger voids in samples pressed at 0.67 x 10^8 Pa (#1, and #2). As expected, the apparent density of the other samples, produced under greater pressure, is higher. The actual density could clarify these micrograph observations. Immediately after the pellets were pressed, they had flat cylindrical shapes. After the temperature treatments of "flashing" and annealing, they contracted and slightly deformed. This made it difficult to accurately determine their densities by simply measuring masses with an analytical balance and dimensions with a vernier caliper. Approximate values of density were calculated for each of the six samples of batch 17 and are shown below in table 7-7.

Sample #	1	2	3	4	5	6
ρ (g/cm^3)	4.31*	4.31	4.57	4.53	4.64	4.94
Pressure (10^8 Pa)	.67	.67	3.3	3.3	6.7	6.7

*estimate

Table 7-7. Approximate densities for the six samples of batch 17.

The densities of the samples follow the expected pattern: higher densities for samples pelletized at greater pressure.

Finally, with the help of Dr. Ruslan Prosorov at the University of South Carolina, the magnetic mass susceptibility as a function of temperature, for all the 7% Fe-doped samples of batch 17, was determined using a computer controlled SQUID susceptometer. Measurements for applied magnetic fields of 0.1, 0.4, and 1 Tesla were taken. The plotted results are shown on the following page (figure 7-16).

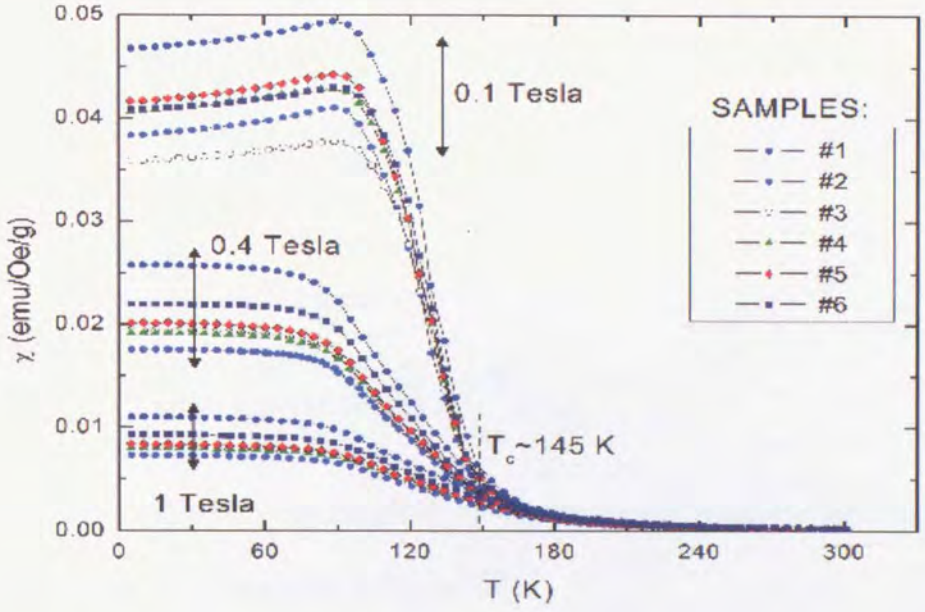

Figure 7-16. Mass* susceptibility as a function of temperature under applied magnetic fields of 0.1, 0.4 and 1.0 T, for the six Fe-doped samples of batch 17.

It can be observed in the above graph, that as the temperature decreases from room temperature, the six samples of batch 17 undergo a magnetic transition from a paramagnetic to a ferromagnetic state. In all of these samples the transition begins at the same temperature - about 145 K - and ends at about 85 K with the midway transition occurring at about 119 K. This midway transition temperature is nearly the same as the average of the transition temperatures of all six samples, as indicated in column 3 of table 7-4. This is also observed in the graphs of electrical resistivity vs. temperature previously shown in figures 7-6 through 7-11.

As discussed in chapter two, the magnetization **M** (magnetic moment per unit volume) is proportional to the macroscopic magnetic field intensity **H,** i.e. $\mathbf{M}=\chi\,\mathbf{H}$ (see eq. 2.1, page 1). The magnetic induction **B** is given by

$$\mathbf{B} = \mu_0\mathbf{H} + \mu_0\mathbf{M} \qquad (7.2)$$

* See reference page 89

By combining equations 2.1 and 7.2, it is possible to write

$$\mathbf{M} = \frac{\chi \mathbf{B}}{\mu_0 (1+\chi)}. \tag{7.3}$$

For diamagnetic and paramagnetic substances, the absolute value of the magnetic susceptibility χ is very small compared to 1.

Therefore, for these materials, $\mathbf{M} \cong \frac{\chi \mathbf{B}}{\mu_0}$. (7.4)

The inverse relationship between magnetic susceptibility and magnetic field induction shown by equation 7.4, is apparent in figure 7-16.

7.3 Conclusions

In the case of Ca and Fe doped manganite samples, the "flashing" technique is applicable and useful in the preparation of structurally sound pellets. Using this "flashing" technique, 5 and 7% Fe-doped specimens were prepared. Eight samples were produced and analyzed (batch 15, samples #1 and #2, and batch 17, samples #1 through #6). Electron microscope analyses indicate that, within reasonable experimental error, the atomic composition of these samples is ideal. Furthermore, there is practically no correlation between oxygen content, flashing temperature, and pelletizing pressure. Electron microscope micrographs show the effect of increasing "flashing" temperature on the increase of grain size and connectivity.

In the case of 5% Fe-doped manganites, the electrical resistivity vs. temperature graphs show how, as the flashing temperature increases, the insulator-to-metal transition becomes sharper, and the percent difference in resistivity at the transition (T_c) increases. The comparison of resistivity values and atomic concentrations for Ca and Fe doped

samples flashed at 1500°C (sample #2 of batch 15 and all the samples of batch 17) indicates that, as the percent Fe doping increases from 5 to 7%, the electrical resistivity at T_c increases about two orders of magnitude and the oxygen content slightly decreases. The change in T_c is about 25 K per 1% Fe doping. Also, Ca and Fe doped samples are more resistive than the Ca doped manganites. These observations coincide with previously published results[3].

In all the Fe doped cases, T_c is approximately the same with and without an applied magnetic field. For 7% Fe samples, the percent difference in resistivity at the transition temperature, with and without applied magnetic field, increases with flashing temperature for oxygen annealing, but decreases for air annealed samples. Magnetic susceptibility vs. temperature measurements for the six 7% Fe doped samples of batch 17, at different magnetic fields, reveal the expected para-ferromagnetic transition. The onset of the magnetic transition is the same in all the cases (about 145 K) – see figure 7-16. This is approximately the Curie temperature. As can be seen in table 7-4, the observed electrical resistivity transition occurs slightly below the Curie temperature.

References

1. G. Turilli and F. Licci, Phys. Rev. B **54**, 13052 (1996).

2. A. Maignan, C. Martin, and B. Raveau, Phys. Rev. B **102**, 19 (1997)

3. J. R. Sun, G. H. Rao, B. G. Shen, and H. K. Wong, Applied Physics Letters, **73**, No. 20, 2998 (1998).

4. CRC Handbook of Chemistry and Physics, 48th edition, F-143, 1967 – 1968.

5. Charles Kittel, Introduction to Solid State Physics, 7th edition, John Wiley & Sons, 1996, page 426.

6. Electron Microscope Laboratory (WB 35), Bill Edwards, Kingston University, Kingston-upon-Thames, Surrey, U.K.

7. M. Bleiweiss, Ph. D. Dissertation (University of South Carolina, Columbia, SC., 2003). Dr. T. Datta, advisor.

8. Charles Kittel, Introduction to Solid State Physics, 5th edition, John Wiley & Sons, 1996, page 417.

General Conclusions and Comments – Future research

In any technological application involving solid-state devices, the use of materials with lasting and stable properties is essential. The "flashing" procedure developed in this research project will be of vital importance in future manganite research and applications.

The "flashing" procedure was used in the preparation of all of the samples studied for this project. It was observed that, as the flashing temperature increases to an optimal value, the grains grow larger, become more connected and, for a given Fe concentration, the electrical resistivity decreases and the transition temperature increases. Beyond a certain flashing temperature point, the material begins to decompose and becomes more and more resistive. For a given doping concentration, it is possible to find an optimum flashing temperature.

This research has provided a more complete picture of the magnetoresistive properties of Ca and Fe doped manganites with doping levels between 0.0 and .08 . We now know that increasing the Fe doping level to 7% provides a substantial improvement over a 5% doping level in that the magnetoresistance effect is increased by nearly four times (10% for 5% Fe doping and 40% for 7% Fe doping---see figure 7-14).

The resistive transition and resistivity are higher for Ca doped samples compared to Ca and Fe doped samples. As the Fe concentration increases, the samples become less conductive and the transition temperature decreases at a rate of about 25 K for each 1% of Fe content. With the exception of the "hard" sample, negative magneto-resistance is observed in all the cases studied. In general, the onset of the magnetic

transition is field independent, coincides with the resistivity transition for Ca doped specimens and is higher for Ca and Fe doped specimens.

This research has shown conclusively that annealing in oxygen not only increases MR characteristics, but also increases the transition temperature as well. Both of these properties are valuable advances toward the use of MR materials in commercial/industrial applications.

Future researchers will benefit from the discovery in this project that sample fabrication has the additional tuning parameter of adjusting the pelletizing pressure used to make the pellets. As the research here has shown, the increased inter-grain connectivity resulting from increased pelletizing pressure increases the MR response of the material.

Other than the study of the effect of flashing in other Ca and 3d-element doped manganite samples and their characterization, an obvious continuation of this research would be the systematic study of the positive magnetoresistance observed in the case of the "hard" Ca doped manganite pellet. This would require the preparation of many samples under different flashing temperatures, pelletizing pressures and annealing conditions. A very detailed electron-microscope study of all the samples would be required.

APPENDIX A

Presentations given at the American Physical Society annual meeting.

1. "Modified Solid State Reaction Technique to Produce Structurally Sound Polycrystalline Samples of Colossal magnetoresistive $La_{0.7}Ca_{0.3}MnO_3$."
   J. Brower, J. A. Estrada, V. Montgomery, T. Datta, and M. Bleiweiss, Bulletin Am. Phys. Soc., Vol. 45, No. 1, 756, 2000.

2. "Magnetoresistance of Lanthanum-based Perovskite Manganites" A. Lungu, M. Bleiweiss, S. Saygi, T. Datta, Z Iqbal, J. Amirzadeh, J. A. Estrada, and J. Brower. Bulletin Am. Phys. Soc., Vol. 45, No. 1, 852, 2000.

3. "Magnetic and Transport Properties of Lanthanum Based CMR Systems." J. A. Estrada, J. Brower, V. Montgomery, M. Bleiweiss, T. Datta, E. Palm, B. Brant, and R. Tsu. Bulletin Am. Phys. Soc., Vol. 47, No. 1, Part I, 510, 2002.

4. "Correlation between Heat Treatment, Resistivity and Magnetoresistance in Polycrystalline Samples of $La_{9.7}Ca_{0.3}MnO_3$."
   J. A. Estrada, J. Brower, and V. Montgomery.
   Bulletin Am. Phys. Soc., Vol. 47, No. 1, Part I, 540, 2002.

(Reproduced from original)

HIGH-TECH MATERIALS ALERT

An intelligence service from

TECHNICAL INSIGHTS

May 19, 2000

STABLE POLYCRYSTALLINE CMR MATERIALS

Recently, there has been a renewed interest in the colossal magnetoresistance observed in manganites with the perovskite structure R1-xAxMnO3 (where R is a rare-earth element and A is Ba, Ca, or Sr). Trouble is, polycrystalline samples of these materials sometimes disintegrate after several days, making it difficult to research and to develop into devices.

Researchers at Grand Valley State University (MI), UK's Kingston University, and the University of South Carolina have been working on a modified solid-state reaction technique for the preparation of structurally sound polycrystalline samples of La0.7Ca0.3MnO3. First, the stoichiometry mixture is calcined at 1180 degrees C, in air atmosphere, for 14 hours. The resulting compound is reground, and the process is repeated once more. Then, after carefully regrinding, a pellet is pressed. The pellet is put in a high-temperature alumina crucible on a bed of powder of the same chemical composition. Using a high-temperature furnace, the crucible and its contents are rapidly heated to a temperature of 1250 +/- 4 degrees C. This temperature is manually controlled and maintained for 10 minutes. Then the pellet is left to cool to room temperature in the furnace. Finally, the sample is annealed in O2 atmosphere from 900 degrees C to 400 degrees C for four days.

The structurally sound pellet is now ready for characterization, such as X-ray diffraction, electron microscopy, transport measurements with and without applied magnetic fields, and magnetic moment measurements.

M000103

40700

Details: Jerry Brower, Javier Estrada, Associate Professor, Physics Dept., Grand Valley State University, Allendale, MI 49401. Phone: 616-895-2275. Fax: 616-895-3740. E-mail: browerje@gvsu.edu, estradaj@gvsu.edu.

Index for Appendix B

List of Abbreviations

Temp (K) or T(K)	Temperature in Kelvins
V1234+	Voltage in milli-volts. Voltage measurement taken across contacts (1,2) with current (milli-amperes) across (3,4).
V1234 -	Same contacts used with polarity reversed on (3,4).
Vavg1234	Average of voltage measurements V1234+ and V1234 -.
V1324+	Voltage in milli-volts. Voltage measurement taken across contacts (2,3) with current (milli-amperes) across (1,4).
V1324 -	Same contacts used with polarity reversed on (1,4).
Vavg1324	Average of voltage measurements V1324+ and V1324 -.

Pellet sample contact placement

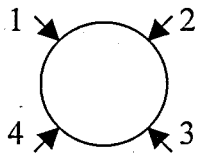

R1234 R1324	Resistance (V/I) for each contact configuration used.
X	Used with the Van der Pauw formula $X = \left(\frac{R_{(1,2,3,4)} - R_{(1,3,2,4)}}{R_{(1,2,3,4)} + R_{(1,3,2,4)}} \right)$ For calculating the correction factor for the physical dimensions of a disk-shaped sample.
Corr fact	Correction factor $f = 1 - 0.3466x^2 - 0.0924x^4$ where x is the value in the column labeled "X" (see X, above) and is used in the Van der Pauw formula $\rho = \frac{\pi d}{\ln 2} \frac{(R_{(1,2,3,4)} + R_{(1,3,2,4)})}{2} f$ to calculate the resistivity of the pellet sample.
ρ (Ω - cm)	The resistivity in ohm-centimeters of the pellet sample.

Resistance vs Temperature for YBC Sample #5

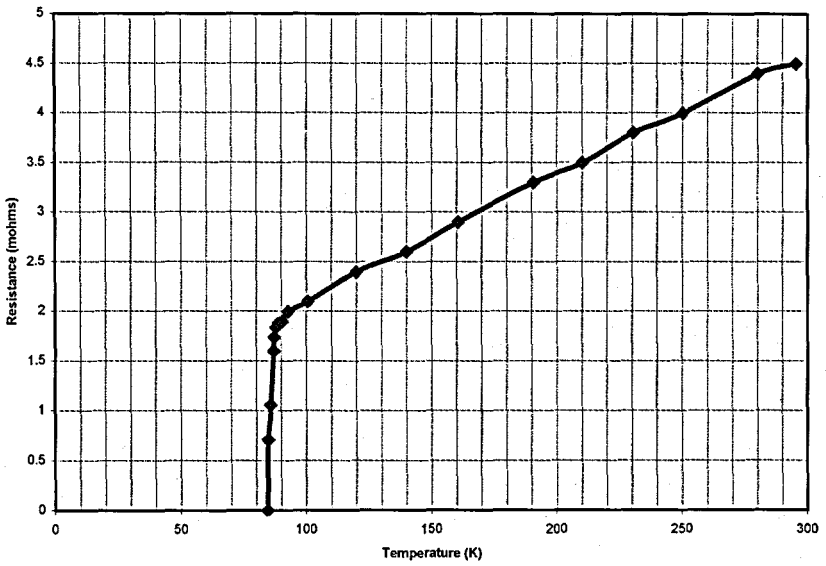

T(K)	V+ (μV)	V- (μV)	avg V(μV)	R (m-ohms)
295.4	180	182	181	4.5
280.2	164	183	174	4.4
250.2	143	176	160	4
230.5	129	170	150	3.8
210.1	118	163	141	3.5
190.6	106	155	131	3.3
160.4	89	144	116	2.9
140	79	134	106	2.6
120	69	125	97	2.4
100.5	56	115	86	2.1
92.7	49	109	79	2
90.3	46	106	76	1.9
88.8	43.3	107	75.4	1.88
87.8	42.5	104.8	73.6	1.84
87.24	38.7	100.8	69.8	1.74
86.76	33.1	94.7	63.9	1.6
85.73	11.3	73.9	42.6	1.06
84.73	-21.3	-35.5	-28.4	0.71
84.5	Extrapolated to R=0 at 84.5			0

Data for Sample #1, ref. page 77

Temp (K)	V1234 +	V1234 -	V avg1234	V1324 +	V1324 -	V avg1324	R1234	R1324	X	Corr fact	ρ (Ω–cm)
295.0	0.9140	0.9300	0.9220	1.2270	1.2380	1.2325	0.0922	0.1233	-0.1441	0.9928	0.0926
285.0	1.0570	1.0820	1.0695	1.4080	1.4180	1.4130	0.1070	0.1413	-0.1384	0.9933	0.1067
275.0	1.2190	1.2470	1.2330	1.5550	1.5710	1.5630	0.1233	0.1563	-0.1180	0.9952	0.1205
265.0	1.2700	1.2960	1.2830	1.6970	1.7180	1.7075	0.1283	0.1708	-0.1419	0.9930	0.1285
255.0	1.3000	1.3300	1.3150	1.7480	1.7610	1.7545	0.1315	0.1755	-0.1432	0.9929	0.1319
245.0	1.3020	1.3410	1.3215	1.7540	1.7700	1.7620	0.1322	0.1762	-0.1429	0.9929	0.1325
235.0	1.2750	1.3050	1.2900	1.7160	1.7350	1.7255	0.1290	0.1726	-0.1444	0.9927	0.1296
225.0	1.2140	1.2430	1.2285	1.6360	1.6500	1.6430	0.1229	0.1643	-0.1443	0.9927	0.1234
215.0	1.1300	1.1650	1.1475	1.5250	1.5330	1.5290	0.1148	0.1529	-0.1425	0.9929	0.1150
200.0	0.9830	1.0110	0.9970	1.3170	1.3320	1.3245	0.0997	0.1325	-0.1411	0.9931	0.0998
			Data	below	for With	B-field					
295.0	0.9170	0.9370	0.9270	1.2210	1.2380	1.2295	0.0927	0.1230	-0.1403	0.9931	0.0927
285.0	1.0530	1.0740	1.0635	1.4070	1.4150	1.4110	0.1064	0.1411	-0.1404	0.9931	0.1064
275.0	1.1910	1.2220	1.2065	1.5910	1.6070	1.5990	0.1207	0.1599	-0.1399	0.9932	0.1206
265.0	1.2380	1.2690	1.2535	1.6620	1.6710	1.6665	0.1254	0.1667	-0.1414	0.9930	0.1255
255.0	1.2660	1.3000	1.2830	1.7020	1.7200	1.7110	0.1283	0.1711	-0.1430	0.9929	0.1287
245.0	1.2710	1.3030	1.2870	1.7140	1.7300	1.7220	0.1287	0.1722	-0.1446	0.9927	0.1293
235.0	1.2420	1.2740	1.2580	1.6740	1.6920	1.6830	0.1258	0.1683	-0.1445	0.9927	0.1264
225.0	1.1820	1.2100	1.1960	1.5950	1.6070	1.6010	0.1196	0.1601	-0.1448	0.9927	0.1202
215.0	1.0960	1.1340	1.1150	1.4830	1.4950	1.4890	0.1115	0.1489	-0.1436	0.9928	0.1119
200.0	0.9540	0.9840	0.9690	1.2810	1.2970	1.2890	0.0969	0.1289	-0.1417	0.9930	0.0971

thickness "d"= .191cm density = 4.046g/cm^3 Voltage in mV Current I=10mA

diameter = 1.278cm Batch 14; Sample 1 Average corr Factor= 0.9930

Data for Sample #2, ref. page 78

Temp (K)	V1234 +	V1234 -	V avg1234	V1324 +	V1324 -	V avg1324	R1234	R1324	X	Corr fact	ρ (Ω–cm)
295.0	0.5120	0.5250	0.5185	0.5670	0.5670	0.5670	0.0519	0.0567	-0.0447	0.9993	0.0462
285.0	0.5670	0.5830	0.5750	0.6380	0.6320	0.6350	0.0575	0.0635	-0.0496	0.9991	0.0515
275.0	0.6370	0.6640	0.6505	0.7240	0.7260	0.7250	0.0651	0.0725	-0.0542	0.9990	0.0586
270.0	0.6530	0.6780	0.6655	0.7440	0.7460	0.7450	0.0666	0.0745	-0.0564	0.9989	0.0600
265.0	0.5710	0.5940	0.5825	0.6620	0.6590	0.6605	0.0583	0.0661	-0.0628	0.9986	0.0529
255.0	0.4320	0.4580	0.4450	0.5090	0.5100	0.5095	0.0445	0.0510	-0.0676	0.9984	0.0406
240.0	0.3490	0.3790	0.3640	0.4160	0.4180	0.4170	0.0364	0.0417	-0.0679	0.9984	0.0332
225.0	0.3010	0.3190	0.3100	0.3590	0.3590	0.3590	0.0310	0.0359	-0.0732	0.9981	0.0285
200.0	0.2360	0.2530	0.2445	0.2840	0.2770	0.2805	0.0245	0.0281	-0.0686	0.9984	0.0223
			Data	**below**	**for**	**With**	**B-field**				
295.0	0.5040	0.5190	0.5115	0.5630	0.5640	0.5635	0.0512	0.0564	-0.0484	0.9992	0.0458
285.0	0.5690	0.5840	0.5765	0.6400	0.6390	0.6395	0.0577	0.0640	-0.0518	0.9991	0.0518
275.0	0.6280	0.6470	0.6375	0.7090	0.7130	0.7110	0.0638	0.0711	-0.0545	0.9990	0.0574
270.0	0.6080	0.6300	0.6190	0.6950	0.6950	0.6950	0.0619	0.0695	-0.0578	0.9988	0.0559
265.0	0.5330	0.5530	0.5430	0.6120	0.6190	0.6155	0.0543	0.0616	-0.0626	0.9986	0.0493
260.0	0.4670	0.4920	0.4795	0.5460	0.5490	0.5475	0.0480	0.0548	-0.0662	0.9985	0.0437
255.0	0.4230	0.4430	0.4330	0.4960	0.4950	0.4955	0.0433	0.0496	-0.0673	0.9984	0.0395
235.0	0.3260	0.3460	0.3360	0.3870	0.3830	0.3850	0.0336	0.0385	-0.0680	0.9984	0.0307
200.0	0.2250	0.2420	0.2335	0.2700	0.2690	0.2695	0.0234	0.0270	-0.0716	0.9982	0.0214

thickness "d"=.188 cm density =4.308 g/cm^3 Voltage in mV Current I=10mA

diameter =1.247 cm Batch 14; Sample 2 Average corr Factor= 0.9987

Data for Sample #3, ref. page 78

Data for No B-field*

Temp (K)	V1234 +	V1234 -	V avg1234	V1324 +	V1324 -	V avg1324	R1234	R1324	X	Corr fact	ρ (Ω–cm)
295.0	0.4150	0.4270	0.4210	0.2900	0.2940	0.2920	0.0421	0.0292	0.1809	0.9886	0.0284
285.0	0.4660	0.4840	0.4750	0.3270	0.3330	0.3300	0.0475	0.0330	0.1801	0.9887	0.0321
280.0	0.4970	0.5140	0.5055	0.3490	0.3490	0.3490	0.0506	0.0349	0.1831	0.9883	0.0341
275.0	0.5360	0.5440	0.5400	0.3710	0.3690	0.3700	0.0540	0.0370	0.1868	0.9878	0.0363
270.0	0.5550	0.5770	0.5660	0.3900	0.3910	0.3905	0.0566	0.0391	0.1835	0.9882	0.0381
265.0	0.5550	0.5810	0.5680	0.3920	0.3920	0.3920	0.0568	0.0392	0.1833	0.9882	0.0383
260.0	0.5210	0.5420	0.5315	0.3630	0.3640	0.3635	0.0532	0.0364	0.1877	0.9877	0.0357
255.0	0.4590	0.4820	0.4705	0.3210	0.3230	0.3220	0.0471	0.0322	0.1874	0.9877	0.0316
250.0	0.3840	0.4050	0.3945	0.2720	0.2670	0.2695	0.0395	0.0270	0.1883	0.9876	0.0265
245.0	0.2370	0.2530	0.2450	0.1750	0.1700	0.1725	0.0245	0.0173	0.1737	0.9895	0.0167
240.0	0.1930	0.2100	0.2015	0.1440	0.1410	0.1425	0.0202	0.0143	0.1715	0.9897	0.0137
235.0	0.1810	0.1960	0.1885	0.1290	0.1350	0.1320	0.0189	0.0132	0.1763	0.9891	0.0128
230.0	0.1690	0.1840	0.1765	0.1300	0.1240	0.1270	0.0177	0.0127	0.1631	0.9907	0.0121
225.0	0.1630	0.1750	0.1690	0.1230	0.1210	0.1220	0.0169	0.0122	0.1615	0.9909	0.0116
215.0	0.1420	0.1710	0.1565	0.1080	0.1120	0.1100	0.0157	0.0110	0.1745	0.9894	0.0106
200.0	0.1290	0.1450	0.1370	0.0950	0.0920	0.0935	0.0137	0.0094	0.1887	0.9875	0.0092

*See next page for Data With B-field

Data for Sample #3, ref. page 78

Data for With B-field

295.0	0.4140	0.4310	0.4225	0.2920	0.2920	0.2920	0.0423	0.0292	0.1826	0.9883	0.0285
285.0	0.4640	0.4820	0.4730	0.3270	0.3270	0.3270	0.0473	0.0327	0.1825	0.9884	0.0319
280.0	0.4920	0.5120	0.5020	0.3500	0.3490	0.3495	0.0502	0.0350	0.1791	0.9888	0.0340
275.0	0.5220	0.5420	0.5320	0.3690	0.3660	0.3675	0.0532	0.0368	0.1829	0.9883	0.0359
270.0	0.5410	0.5590	0.5500	0.3850	0.3820	0.3835	0.0550	0.0384	0.1784	0.9889	0.0372
265.0	0.5300	0.5500	0.5400	0.3740	0.3740	0.3740	0.0540	0.0374	0.1816	0.9885	0.0364
260.0	0.4860	0.5040	0.4950	0.3400	0.3430	0.3415	0.0495	0.0342	0.1835	0.9882	0.0333
255.0	0.4250	0.4470	0.4360	0.3020	0.3020	0.3020	0.0436	0.0302	0.1816	0.9885	0.0294
250.0	0.3550	0.3710	0.3630	0.2550	0.2480	0.2515	0.0363	0.0252	0.1814	0.9885	0.0245
245.0	0.2130	0.2470	0.2300	0.1630	0.1690	0.1660	0.0230	0.0166	0.1616	0.9909	0.0158
240.0	0.1890	0.2090	0.1990	0.1420	0.1400	0.1410	0.0199	0.0141	0.1706	0.9898	0.0136
235.0	0.1730	0.1980	0.1855	0.1300	0.1340	0.1320	0.0186	0.0132	0.1685	0.9901	0.0127
230.0	0.1690	0.1810	0.1750	0.1230	0.1230	0.1230	0.0175	0.0123	0.1745	0.9894	0.0119
225.0	0.1570	0.1780	0.1675	0.1230	0.1130	0.1180	0.0168	0.0118	0.1734	0.9895	0.0114
215.0	0.1470	0.1550	0.1510	0.1120	0.1020	0.1070	0.0151	0.0107	0.1705	0.9898	0.0103
200.0	0.1270	0.1370	0.1320	0.0960	0.0870	0.0915	0.0132	0.0092	0.1812	0.9885	0.0089

thickness "d"= .178 cm density = 5.133 g/cm^3 Voltage in mV Current I=10mA

diameter = 1.174 cm Batch 14; Sample 3 Average corr. Factor= 0.9888

Data for Soft Sample, ref. page 85

DATA FOR NO B-FIELD (nB)

Temp(K)	V+(mV)nB	V-(mV)nB	Avg(mV)nB	(ohms)nB
296.2	1.130	1.104	1.1166	0.1117
285.0	1.284	1.247	1.2655	0.1266
278.0	1.388	1.349	1.3685	0.1369
277.0	1.402	1.362	1.3820	0.1382
276.0	1.420	1.379	1.3995	0.1400
275.0	1.428	1.390	1.4090	0.1409
274.0	1.438	1.402	1.4200	0.1420
273.0	1.447	1.410	1.4285	0.1429
272.0	1.449	1.414	1.4315	0.1432
271.0	1.438	1.403	1.4205	0.1421
270.0	1.403	1.368	1.3855	0.1386
260.0	1.085	1.049	1.0670	0.1067
245.0	0.983	0.952	0.9675	0.0968
230.0	0.891	0.857	0.8740	0.0874
180.0	0.581	0.553	0.5670	0.0567
130.0	0.374	0.343	0.3585	0.0359
100.0	0.290	0.256	0.2730	0.0273

DATA FOR WITH B-FIELD (wB)

Temp(K)	V+(mV)wB	V-(mV)wB	Avg(mV)wB	(ohms)wB
295.5	1.1282	1.1213	1.12475	0.1125
285.0	1.253	1.2617	1.25735	0.1257
278.0	1.324	1.3467	1.33535	0.1335
277.0	1.334	1.3536	1.3438	0.1344
276.0	1.338	1.3618	1.3499	0.1350
275.0	1.338	1.359	1.3485	0.1349
274.0	1.334	1.353	1.3435	0.1344
270.0	1.243	1.2465	1.24475	0.1245
265.0	1.125	1.107	1.116	0.1116
260.0	1.045	1.0443	1.04465	0.1045
245.0	0.96	0.9511	0.95555	0.0956
230.0	0.87	0.8577	0.86385	0.0864
180.0	0.581	0.5436	0.5623	0.0562
130.0	0.366	0.33	0.348	0.0348
100.0	0.278	0.255	0.2665	0.0267

Data for Hard Sample, ref. page 85

DATA WITH B-FIELD (wB)					DATA WITHOUT B-FIELD (nB)				
TEMP(K)	V+(mV)wB	V-(mV)wB	V avg(mV)wB	(ohms)wB	TEMP(K)	V+(mV)nB	V-(mV)nB	Vavg(mV)nB	(ohms)nB
295.5	1.97	2.08	2.025	0.068	295.5	1.41	1.4	1.405	0.047
285	2.15	2.16	2.155	0.072	285	1.5	1.52	1.51	0.050
275	2.18	2.38	2.28	0.076	275	1.67	1.62	1.645	0.055
273	2.21	2.46	2.335	0.078	273	1.66	1.66	1.66	0.055
271	2.23	2.44	2.335	0.078	271	1.69	1.69	1.69	0.056
269	2.2	2.44	2.32	0.077	269	1.72	1.7	1.71	0.057
268	2.24	2.45	2.345	0.078	268	1.75	1.74	1.745	0.058
267	2.23	2.47	2.35	0.078	267	1.76	1.74	1.75	0.058
266	2.2	2.47	2.335	0.078	266	1.78	1.74	1.76	0.059
265	2.18	2.42	2.3	0.077	265	1.8	1.76	1.78	0.059
260	2.08	2.35	2.215	0.074	260	1.78	1.76	1.77	0.059
250	1.88	2.06	1.97	0.066	250	1.51	1.55	1.53	0.051
230	1.57	1.7	1.635	0.055	230	1.45	1.33	1.39	0.046
180	1.38	1.31	1.345	0.045	180	1.21	1.11	1.16	0.039
150	1.2	1.11	1.155	0.039	150	1.09	0.98	1.035	0.035
100	0.77	0.79	0.78	0.026	100	0.69	0.66	0.675	0.023

Data for Batch #14 Sample 1, ref. page 102

Temp (K)	V1234 +	V1234 -	V avg1234	V1324 +	V1324 -	V avg1324	R1234	R1324	X	Corr fact	ρ (Ω-cm)
295.0	0.9140	0.9300	0.9220	1.2270	1.2380	1.2325	0.0922	0.1233	-0.1441	0.9928	0.0926
285.0	1.0570	1.0820	1.0695	1.4080	1.4180	1.4130	0.1070	0.1413	-0.1384	0.9933	0.1067
275.0	1.2190	1.2470	1.2330	1.5550	1.5710	1.5630	0.1233	0.1563	-0.1180	0.9952	0.1205
265.0	1.2700	1.2960	1.2830	1.6970	1.7180	1.7075	0.1283	0.1708	-0.1419	0.9930	0.1285
255.0	1.3000	1.3300	1.3150	1.7480	1.7610	1.7545	0.1315	0.1755	-0.1432	0.9929	0.1319
245.0	1.3020	1.3410	1.3215	1.7540	1.7700	1.7620	0.1322	0.1762	-0.1429	0.9929	0.1325
235.0	1.2750	1.3050	1.2900	1.7160	1.7350	1.7255	0.1290	0.1726	-0.1444	0.9927	0.1296
225.0	1.2140	1.2430	1.2285	1.6360	1.6500	1.6430	0.1229	0.1643	-0.1443	0.9927	0.1234
215.0	1.1300	1.1650	1.1475	1.5250	1.5330	1.5290	0.1148	0.1529	-0.1425	0.9929	0.1150
200.0	0.9830	1.0110	0.9970	1.3170	1.3320	1.3245	0.0997	0.1325	-0.1411	0.9931	0.0998
			Data	below	For	With	B-field				
295.0	0.9170	0.9370	0.9270	1.2210	1.2380	1.2295	0.0927	0.1230	-0.1403	0.9931	0.0927
285.0	1.0530	1.0740	1.0635	1.4070	1.4150	1.4110	0.1064	0.1411	-0.1404	0.9931	0.1064
275.0	1.1910	1.2220	1.2065	1.5910	1.6070	1.5990	0.1207	0.1599	-0.1399	0.9932	0.1206
265.0	1.2380	1.2690	1.2535	1.6620	1.6710	1.6665	0.1254	0.1667	-0.1414	0.9930	0.1255
255.0	1.2660	1.3000	1.2830	1.7020	1.7200	1.7110	0.1283	0.1711	-0.1430	0.9929	0.1287
245.0	1.2710	1.3030	1.2870	1.7140	1.7300	1.7220	0.1287	0.1722	-0.1446	0.9927	0.1293
235.0	1.2420	1.2740	1.2580	1.6740	1.6920	1.6830	0.1258	0.1683	-0.1445	0.9927	0.1264
225.0	1.1820	1.2100	1.1960	1.5950	1.6070	1.6010	0.1196	0.1601	-0.1448	0.9927	0.1202
215.0	1.0960	1.1340	1.1150	1.4830	1.4950	1.4890	0.1115	0.1489	-0.1436	0.9928	0.1119
200.0	0.9540	0.9840	0.9690	1.2810	1.2970	1.2890	0.0969	0.1289	-0.1417	0.9930	0.0971

thickness "d"= .191cm density = 4.046g/cm^3 Voltage in mV Current I=10mA

diameter = 1.278cm Batch 14; Sample 1 Average corr. Factor= 0.9930

Data for Batch #14 Sample 2, ref. page 102

Temp (K)	V1234 +	V1234 -	V avg1234	V1324 +	V1324 -	V avg1324	R1234	R1324	X	Corr fact	ρ (Ω–cm)
295.0	0.5120	0.5250	0.5185	0.5670	0.5670	0.5670	0.0519	0.0567	-0.0447	0.9993	0.0462
285.0	0.5670	0.5830	0.5750	0.6380	0.6320	0.6350	0.0575	0.0635	-0.0496	0.9991	0.0515
275.0	0.6370	0.6640	0.6505	0.7240	0.7260	0.7250	0.0651	0.0725	-0.0542	0.9990	0.0586
270.0	0.6530	0.6780	0.6655	0.7440	0.7460	0.7450	0.0666	0.0745	-0.0564	0.9989	0.0600
265.0	0.5710	0.5940	0.5825	0.6620	0.6590	0.6605	0.0583	0.0661	-0.0628	0.9986	0.0529
255.0	0.4320	0.4580	0.4450	0.5090	0.5100	0.5095	0.0445	0.0510	-0.0676	0.9984	0.0406
240.0	0.3490	0.3790	0.3640	0.4160	0.4180	0.4170	0.0364	0.0417	-0.0679	0.9984	0.0332
225.0	0.3010	0.3190	0.3100	0.3590	0.3590	0.3590	0.0310	0.0359	-0.0732	0.9981	0.0285
200.0	0.2360	0.2530	0.2445	0.2840	0.2770	0.2805	0.0245	0.0281	-0.0686	0.9984	0.0223
			Data	below	For	With	B-field				
295.0	0.5040	0.5190	0.5115	0.5630	0.5640	0.5635	0.0512	0.0564	-0.0484	0.9992	0.0458
285.0	0.5690	0.5840	0.5765	0.6400	0.6390	0.6395	0.0577	0.0640	-0.0518	0.9991	0.0518
275.0	0.6280	0.6470	0.6375	0.7090	0.7130	0.7110	0.0638	0.0711	-0.0545	0.9990	0.0574
270.0	0.6080	0.6300	0.6190	0.6950	0.6950	0.6950	0.0619	0.0695	-0.0578	0.9988	0.0559
265.0	0.5330	0.5530	0.5430	0.6120	0.6190	0.6155	0.0543	0.0616	-0.0626	0.9986	0.0493
260.0	0.4670	0.4920	0.4795	0.5460	0.5490	0.5475	0.0480	0.0548	-0.0662	0.9985	0.0437
255.0	0.4230	0.4430	0.4330	0.4960	0.4950	0.4955	0.0433	0.0496	-0.0673	0.9984	0.0395
235.0	0.3260	0.3460	0.3360	0.3870	0.3830	0.3850	0.0336	0.0385	-0.0680	0.9984	0.0307
200.0	0.2250	0.2420	0.2335	0.2700	0.2690	0.2695	0.0234	0.0270	-0.0716	0.9982	0.0214

thickness "d"=.188 cm
diameter =1.247 cm

density =4.308 g/cm^3
Batch 14; Sample 2

Voltage in mV

Current I=10mA
Average corr. Factor= 0.9987

Data for Batch #14 Sample 3, ref. page 103

Data for No B-field*

Temp (K)	V1234 +	V1234 -	V avg1234	V1324 +	V1324 -	V avg1324	R1234	R1324	X	Corr fact	ρ (Ω-cm)
295.0	0.4150	0.4270	0.4210	0.2900	0.2940	0.2920	0.0421	0.0292	0.1809	0.9886	0.0284
285.0	0.4660	0.4840	0.4750	0.3270	0.3330	0.3300	0.0475	0.0330	0.1801	0.9887	0.0321
280.0	0.4970	0.5140	0.5055	0.3490	0.3490	0.3490	0.0506	0.0349	0.1831	0.9883	0.0341
275.0	0.5360	0.5440	0.5400	0.3710	0.3690	0.3700	0.0540	0.0370	0.1868	0.9878	0.0363
270.0	0.5550	0.5770	0.5660	0.3900	0.3910	0.3905	0.0566	0.0391	0.1835	0.9882	0.0381
265.0	0.5550	0.5810	0.5680	0.3920	0.3920	0.3920	0.0568	0.0392	0.1833	0.9882	0.0383
260.0	0.5210	0.5420	0.5315	0.3630	0.3640	0.3635	0.0532	0.0364	0.1877	0.9877	0.0357
255.0	0.4590	0.4820	0.4705	0.3210	0.3230	0.3220	0.0471	0.0322	0.1874	0.9877	0.0316
250.0	0.3840	0.4050	0.3945	0.2720	0.2670	0.2695	0.0395	0.0270	0.1883	0.9876	0.0265
245.0	0.2370	0.2530	0.2450	0.1750	0.1700	0.1725	0.0245	0.0173	0.1737	0.9895	0.0167
240.0	0.1930	0.2100	0.2015	0.1440	0.1410	0.1425	0.0202	0.0143	0.1715	0.9897	0.0137
235.0	0.1810	0.1960	0.1885	0.1290	0.1350	0.1320	0.0189	0.0132	0.1763	0.9891	0.0128
230.0	0.1690	0.1840	0.1765	0.1300	0.1240	0.1270	0.0177	0.0127	0.1631	0.9907	0.0121
225.0	0.1630	0.1750	0.1690	0.1230	0.1210	0.1220	0.0169	0.0122	0.1615	0.9909	0.0116
215.0	0.1420	0.1710	0.1565	0.1080	0.1120	0.1100	0.0157	0.0110	0.1745	0.9894	0.0106
200.0	0.1290	0.1450	0.1370	0.0950	0.0920	0.0935	0.0137	0.0094	0.1887	0.9875	0.0092

* Data for With B-field on next page.

Data for Batch #14 Sample 3, ref. page 103

Data for With B-field

Temp (K)	V1234 +	V1234 -	V avg1234	V1324 +	V1324 -	V avg1324	R1234	R1324	X	Corr fact	ρ (Ω–cm)
295.0	0.4140	0.4310	0.4225	0.2920	0.2920	0.2920	0.0423	0.0292	0.1826	0.9883	0.0285
285.0	0.4640	0.4820	0.4730	0.3270	0.3270	0.3270	0.0473	0.0327	0.1825	0.9884	0.0319
280.0	0.4920	0.5120	0.5020	0.3500	0.3490	0.3495	0.0502	0.0350	0.1791	0.9888	0.0340
275.0	0.5220	0.5420	0.5320	0.3690	0.3660	0.3675	0.0532	0.0368	0.1829	0.9883	0.0359
270.0	0.5410	0.5590	0.5500	0.3850	0.3820	0.3835	0.0550	0.0384	0.1784	0.9889	0.0372
265.0	0.5300	0.5500	0.5400	0.3740	0.3740	0.3740	0.0540	0.0374	0.1816	0.9885	0.0364
260.0	0.4860	0.5040	0.4950	0.3400	0.3430	0.3415	0.0495	0.0342	0.1835	0.9882	0.0333
255.0	0.4250	0.4470	0.4360	0.3020	0.3020	0.3020	0.0436	0.0302	0.1816	0.9885	0.0294
250.0	0.3550	0.3710	0.3630	0.2550	0.2480	0.2515	0.0363	0.0252	0.1814	0.9885	0.0245
245.0	0.2130	0.2470	0.2300	0.1630	0.1690	0.1660	0.0230	0.0166	0.1616	0.9909	0.0158
240.0	0.1890	0.2090	0.1990	0.1420	0.1400	0.1410	0.0199	0.0141	0.1706	0.9898	0.0136
235.0	0.1730	0.1980	0.1855	0.1300	0.1340	0.1320	0.0186	0.0132	0.1685	0.9901	0.0127
230.0	0.1690	0.1810	0.1750	0.1230	0.1230	0.1230	0.0175	0.0123	0.1745	0.9894	0.0119
225.0	0.1570	0.1780	0.1675	0.1230	0.1130	0.1180	0.0168	0.0118	0.1734	0.9895	0.0114
215.0	0.1470	0.1550	0.1510	0.1120	0.1020	0.1070	0.0151	0.0107	0.1705	0.9898	0.0103
200.0	0.1270	0.1370	0.1320	0.0960	0.0870	0.0915	0.0132	0.0092	0.1812	0.9885	0.0089

thickness "d"= .178 cm density = 5.133 g/cm^3 Voltage in mV Current I=10mA

diameter = 1.174 cm Batch 14; Sample 3 Average corr. Factor= 0.9888

Data for Batch #14 Sample 4, ref. page 103

Data for No B-field*

Temp (K)	V1234 +	V1234 -	V avg1234	V1324 +	V1324 -	V avg1324	R1234	R1324	X	Corr fact	ρ(Ω–cm)
294.7	3.67	3.69	3.68	0.369	0.373	0.371	0.368	0.0371	0.8168	0.7276	0.1276
285	4.24	4.27	4.255	0.426	0.429	0.4275	0.4255	0.0428	0.8174	0.7272	0.1474
277	4.8	4.83	4.815	0.487	0.481	0.484	0.4815	0.0484	0.8173	0.7272	0.1668
273	5.12	5.16	5.14	0.512	0.518	0.515	0.514	0.0515	0.8179	0.7268	0.1779
271	5.28	5.32	5.3	0.529	0.535	0.532	0.53	0.0532	0.8176	0.7271	0.1836
270	5.36	5.4	5.38	0.538	0.544	0.541	0.538	0.0541	0.8173	0.7273	0.1864
269	5.44	5.48	5.46	0.547	0.553	0.55	0.546	0.0550	0.8170	0.7275	0.1893
268	5.52	5.56	5.54	0.556	0.563	0.5595	0.554	0.0560	0.8165	0.7278	0.1922
267	5.6	5.64	5.62	0.566	0.573	0.5695	0.562	0.0570	0.8160	0.7283	0.1951
265	5.8	5.85	5.825	0.585	0.592	0.5885	0.5825	0.0589	0.8165	0.7279	0.2021
251	6.87	6.92	6.895	0.656	0.671	0.6635	0.6895	0.0664	0.8244	0.7217	0.2362
250	6.8	6.86	6.83	0.657	0.67	0.6635	0.683	0.0664	0.8229	0.7229	0.2345
249	6.63	6.68	6.655	0.648	0.667	0.6575	0.6655	0.0658	0.8202	0.7251	0.2295
245	4.92	4.97	4.945	0.491	0.502	0.4965	0.4945	0.0497	0.8175	0.7271	0.1713
240			artificial	point	entered	to	smooth	curve			0.1320
230	3.6	3.64	3.62	0.318	0.326	0.322	0.362	0.0322	0.8366	0.7121	0.1215
215	3.52	3.56	3.54	0.303	0.308	0.3055	0.354	0.0306	0.8411	0.7086	0.1180
200	3.48	3.52	3.5	0.302	0.308	0.305	0.35	0.0305	0.8397	0.7097	0.1169

*Data for With B-field on next page.

Data for Batch #14 Sample 4, ref. page 103

Data for With B-field

Temp (K)	V1234 +	V1234 -	V avg1234	V1324 +	V1324 -	V avg1324	R1234	R1324	X	Corr fact	ρ(Ω–cm)
296.4	3.62	3.61	3.615	0.364	0.364	0.364	0.3615	0.0364	0.8170	0.7275	0.1253
284.8	4.27	4.28	4.275	0.429	0.43	0.4295	0.4275	0.0430	0.8174	0.7272	0.1481
275	4.97	4.99	4.98	0.499	0.5	0.4995	0.498	0.0500	0.8177	0.7270	0.1724
265	5.76	5.79	5.775	0.584	0.587	0.5855	0.5775	0.0586	0.8159	0.7283	0.2005
255	6.59	6.62	6.605	0.616	0.625	0.6205	0.6605	0.0621	0.8282	0.7188	0.2248
253	6.59	6.62	6.605	0.625	0.631	0.628	0.6605	0.0628	0.8264	0.7203	0.2255
252	6.54	6.57	6.555	0.623	0.632	0.6275	0.6555	0.0628	0.8253	0.7211	0.2242
251	6.42	6.46	6.44	0.617	0.625	0.621	0.644	0.0621	0.8241	0.7220	0.2207
247	5.18	5.21	5.195	0.517	0.521	0.519	0.5195	0.0519	0.8183	0.7265	0.1797
240	3.78	3.81	3.795	0.343	0.344	0.3435	0.3795	0.0344	0.8340	0.7142	0.1280
230	3.55	3.58	3.565	0.309	0.31	0.3095	0.3565	0.0310	0.8402	0.7093	0.1190
215	3.47	3.5	3.485	0.298	0.299	0.2985	0.3485	0.0299	0.8422	0.7077	0.1159
200	3.4	3.43	3.415	0.293	0.293	0.293	0.3415	0.0293	0.8420	0.7079	0.1136

density = g/cm^3 Voltage in mV Current I=10mA

Batch 14; Sample 4 Average corr. Factor= 0.72382

Data for Batch #15 Sample 1, ref. page 111

Data for No B-field*

Temp (K)	R1234+	R1234-	R avg1234	R2413+	R2413-	R avg2413	R1234	R2413	X	Corr fact	ρ (Ω–cm)
295.7	2.739	2.742	2.741	1.553	1.557	1.555	0.274	0.156	0.276	0.9731	0.166
285.0	3.205	3.235	3.220	1.816	1.818	1.817	0.322	0.182	0.279	0.9726	0.194
275.0	3.755	3.788	3.772	2.130	2.134	2.132	0.377	0.213	0.278	0.9727	0.228
265.0	4.442	4.480	4.461	2.530	2.533	2.532	0.446	0.253	0.276	0.9731	0.270
255.0	5.301	5.348	5.325	3.021	3.026	3.024	0.532	0.302	0.276	0.9731	0.322
245.0	6.444	6.494	6.469	3.689	3.693	3.691	0.647	0.369	0.273	0.9736	0.392
235.0	7.889	7.942	7.916	4.537	4.562	4.550	0.792	0.455	0.270	0.9742	0.482
225.0	9.767	9.817	9.792	5.624	5.642	5.633	0.979	0.563	0.270	0.9743	0.596
210.0	13.587	13.652	13.620	7.823	7.858	7.841	1.362	0.784	0.269	0.9744	0.829
190.0	21.390	21.420	21.405	12.270	12.290	12.280	2.141	1.228	0.271	0.9741	1.301
170.0	29.790	29.890	29.840	16.040	16.030	16.035	2.984	1.604	0.301	0.9679	1.761
165.0	30.390	30.510	30.450	15.920	15.970	15.945	3.045	1.595	0.313	0.9652	1.776
160.0	30.010	30.140	30.075	15.340	15.360	15.350	3.008	1.535	0.324	0.9626	1.734
155.0	28.680	28.820	28.750	14.440	14.470	14.455	2.875	1.446	0.331	0.9610	1.647
140.0	22.040	22.180	22.110	10.880	10.930	10.905	2.211	1.091	0.339	0.9589	1.256
120.0	13.660	13.750	13.705	6.740	6.740	6.740	1.371	0.674	0.341	0.9585	0.777
100.0	8.730	8.820	8.775	4.280	4.280	4.280	0.878	0.428	0.344	0.9576	0.496

*Data for With B-field on next page.

Data for Batch #15 Sample 1, ref. page 111

Data for With B-field

Temp (K)	R1234+	R1234-	R avg1234	R2413+	R2413-	R avg2413	R1234	R2413	X	Corr fact	ρ (Ω–cm)
295.2	2.823	2.825	2.824	1.560	1.562	1.561	0.282	0.156	0.288	0.9706	0.169
279.7	3.467	3.480	3.474	1.908	1.907	1.908	0.347	0.191	0.291	0.9700	0.207
265.0	4.383	4.416	4.400	2.403	2.405	2.404	0.440	0.240	0.293	0.9695	0.262
250.0	5.661	5.697	5.679	3.112	3.115	3.114	0.568	0.311	0.292	0.9698	0.338
235.0	7.498	7.544	7.521	4.151	4.152	4.152	0.752	0.415	0.289	0.9705	0.449
220.0	10.398	10.435	10.417	5.732	5.734	5.733	1.042	0.573	0.290	0.9702	0.621
205.0	14.193	14.215	14.204	7.848	7.849	7.849	1.420	0.785	0.288	0.9706	0.849
190.0	19.987	19.995	19.991	10.851	10.883	10.867	1.999	1.087	0.296	0.9690	1.186
180.0	23.755	23.821	23.788	12.790	12.816	12.803	2.379	1.280	0.300	0.9680	1.405
172.0	26.855	26.947	26.901	14.124	14.169	14.147	2.690	1.415	0.311	0.9657	1.572
170.0	27.362	27.431	27.397	14.266	14.282	14.274	2.740	1.427	0.315	0.9647	1.594
168.0	28.032	28.096	28.064	14.489	14.510	14.500	2.806	1.450	0.319	0.9638	1.627
166.0	28.428	28.516	28.472	14.499	14.522	14.511	2.847	1.451	0.325	0.9624	1.641
164.0	28.746	28.822	28.784	14.487	14.533	14.510	2.878	1.451	0.330	0.9612	1.651
162.0	28.712	28.877	28.795	14.393	14.437	14.415	2.879	1.442	0.333	0.9605	1.646
160.0	28.577	28.777	28.677	14.239	14.325	14.282	2.868	1.428	0.335	0.9599	1.636
155.0	27.850	28.023	27.937	13.724	13.777	13.751	2.794	1.375	0.340	0.9586	1.585
145.0	24.255	24.468	24.362	11.766	11.818	11.792	2.436	1.179	0.348	0.9568	1.372
130.0	17.042	17.163	17.103	8.228	8.277	8.253	1.710	0.825	0.349	0.9564	0.962
115.0	10.985	11.097	11.041	5.329	5.359	5.344	1.104	0.534	0.348	0.9567	0.622
100.0	7.691	7.755	7.723	3.755	3.774	3.765	0.772	0.376	0.345	0.9575	0.436

thickness "d"= .175cm
diameter = 1.254 cm

Mass = .8507g
Batch 15; Sample 1 (5% Fe)

Avg corr. Factor= 0.9663

Data for Batch #15 Sample 2, ref. page 111

Data for No B-field*

Temp (K)	mV1234 +	mV1234 -	mVavg1234	mV1324 +	mV1324 -	mVavg1324	R1234	R1324	X	Corr fact	ρ (Ω–cm)
295.7	0.548	0.547	0.548	0.427	0.431	0.429	0.055	0.043	0.1214	0.9949	0.0385
280.0	0.681	0.686	0.684	0.539	0.538	0.539	0.068	0.054	0.1187	0.9951	0.0482
265.0	0.864	0.879	0.872	0.687	0.690	0.689	0.087	0.069	0.1173	0.9952	0.0616
250.0	1.122	1.150	1.136	0.903	0.907	0.905	0.114	0.091	0.1132	0.9955	0.0806
235.0	1.523	1.566	1.545	1.231	1.246	1.239	0.154	0.124	0.1100	0.9958	0.1099
220.0	2.150	2.198	2.174	1.737	1.771	1.754	0.217	0.175	0.1069	0.9960	0.1552
205.0	3.199	3.256	3.228	2.569	2.625	2.597	0.323	0.260	0.1082	0.9959	0.2301
190.0	4.935	5.012	4.974	3.958	4.042	4.000	0.497	0.400	0.1085	0.9959	0.3545
177.0	6.419	6.519	6.469	5.165	5.270	5.218	0.647	0.522	0.1071	0.9960	0.4617
175.0	6.503	6.591	6.547	5.236	5.346	5.291	0.655	0.529	0.1061	0.9961	0.4677
173.0	6.483	6.586	6.535	5.235	5.335	5.285	0.653	0.529	0.1057	0.9961	0.4670
160.0	1.994	2.060	2.027	1.526	1.525	1.526	0.203	0.153	0.1412	0.9931	0.1399
145.0	1.498	1.554	1.526	1.306	1.313	1.310	0.153	0.131	0.0764	0.9980	0.1122
130.0	1.415	1.463	1.439	1.273	1.274	1.274	0.144	0.127	0.0610	0.9987	0.1074
115.0	1.373	1.418	1.396	1.267	1.269	1.268	0.140	0.127	0.0479	0.9992	0.1056
100.0	1.321	1.362	1.342	1.270	1.270	1.270	0.134	0.127	0.0274	0.9997	0.1036

*Data for With B-field on next page.

Data for Batch #15 Sample 2, ref. page 111

Data for With B-field

Temp (K)	mV1234 +	mV1234 -	mVavg1234	mV1324 +	mV1324 -	mVavg1324	R1234	R1324	X	Corr fact	ρ (Ω–cm)
295.0	0.532	0.548	0.540	0.444	0.452	0.448	0.054	0.045	0.0931	0.9970	0.0391
280.0	0.662	0.679	0.671	0.551	0.556	0.554	0.067	0.055	0.0956	0.9968	0.0484
265.0	0.840	0.872	0.856	0.702	0.715	0.709	0.086	0.071	0.0943	0.9969	0.0619
250.0	1.119	1.149	1.134	0.940	0.952	0.946	0.113	0.095	0.0904	0.9972	0.0823
235.0	1.546	1.579	1.563	1.292	1.319	1.306	0.156	0.131	0.0896	0.9972	0.1134
220.0	2.217	2.265	2.241	1.842	1.881	1.862	0.224	0.186	0.0925	0.9970	0.1622
205.0	3.300	3.356	3.328	2.722	2.776	2.749	0.333	0.275	0.0953	0.9968	0.2403
190.0	4.994	5.085	5.040	4.106	4.191	4.149	0.504	0.415	0.0970	0.9967	0.3632
185.0	5.574	5.656	5.615	4.585	4.669	4.627	0.562	0.463	0.0965	0.9968	0.4049
182.0	5.753	5.837	5.795	4.751	4.835	4.793	0.580	0.479	0.0946	0.9969	0.4186
180.0	5.788	5.860	5.824	4.766	4.853	4.810	0.582	0.481	0.0954	0.9968	0.4204
178.0	5.742	5.825	5.784	4.755	4.837	4.796	0.578	0.480	0.0933	0.9970	0.4183
175.0	5.275	5.378	5.327	4.424	4.492	4.458	0.533	0.446	0.0888	0.9973	0.3870
160.0	1.515	1.566	1.541	1.334	1.348	1.341	0.154	0.134	0.0692	0.9983	0.1141
145.0	1.407	1.454	1.431	1.273	1.288	1.281	0.143	0.128	0.0553	0.9989	0.1074
130.0	1.326	1.371	1.349	1.228	1.242	1.235	0.135	0.124	0.0439	0.9993	0.1024
100.0	1.158	1.199	1.179	1.225	1.239	1.232	0.1179	0.1232	-0.0222	0.9998	0.0956

thickness "d"= .175cm
diameter = 1.134cm

density = 5.332 g/cm^3
Batch 15; Sample 3

Voltage in mV

Current I=10mA
Avg corr. Factor= .9963

Data for Batch #17 Sample 1, ref. page 117

Data for No B-field*

Temp (K)	mV1234 +	mV1234 -	mVavg1234	mV1324 +	mV1324 -	mVavg1324	R1234	R1324	X	Corr fact	ρ (Ω–cm)
295.0	0.860	0.888	0.874	0.774	0.797	0.786	0.087	0.079	0.0533	0.9990	0.0830
280.0	1.111	1.137	1.124	0.998	1.021	1.010	0.112	0.101	0.0537	0.9990	0.1068
260.0	1.622	1.654	1.638	1.438	1.468	1.453	0.164	0.145	0.0599	0.9988	0.1546
240.0	2.490	2.450	2.470	2.280	2.250	2.265	0.247	0.227	0.0433	0.9994	0.2370
220.0	4.130	4.000	4.065	3.780	3.660	3.720	0.407	0.372	0.0443	0.9993	0.3897
200.0	7.370	7.370	7.370	6.710	6.780	6.745	0.737	0.675	0.0443	0.9993	0.7065
180.0	14.610	14.570	14.590	13.550	13.620	13.585	1.459	1.359	0.0357	0.9996	1.4106
160.0	33.640	33.820	33.730	30.740	30.990	30.865	3.373	3.087	0.0444	0.9993	3.2333
140.0	83.890	84.310	84.100	75.320	75.600	75.460	8.410	7.546	0.0541	0.9990	7.9841
125.0	174.670	175.940	175.305	157.840	158.980	158.410	17.531	15.841	0.0506	0.9991	16.7006
120.0	190.080	191.320	190.700	172.370	173.810	173.090	19.070	17.309	0.0484	0.9992	18.2071
115.0	188.610	189.870	189.240	172.360	173.660	173.010	18.924	17.301	0.0448	0.9993	18.1321
100.0	61.630	62.210	61.920	58.960	59.360	59.160	6.192	5.916	0.0228	0.9998	6.0637
80.0	10.010	10.150	10.080	9.520	9.570	9.545	1.008	0.955	0.0273	0.9997	0.9827

*Data for With B-field on next page.

Data for Batch #17 Sample 1, ref. page 117

Data for With B-field

Temp (K)	mV1234 +	mV1234 -	mVavg1234	mV1324 +	mV1324 -	mVavg1324	R1234	R1324	X	Corr fact	ρ (Ω–cm)
295.0	0.868	0.887	0.878	0.750	0.769	0.760	0.088	0.076	0.0721	0.9982	0.0818
280.0	1.099	1.120	1.110	0.960	0.977	0.969	0.111	0.097	0.0679	0.9984	0.1039
260.0	1.623	1.645	1.634	1.370	1.368	1.369	0.163	0.137	0.0882	0.9973	0.1500
240.0	2.513	2.534	2.524	2.103	2.078	2.091	0.252	0.209	0.0938	0.9969	0.2304
220.0	4.150	4.070	4.110	3.480	3.310	3.395	0.411	0.340	0.0953	0.9968	0.3747
200.0	7.460	7.400	7.430	6.170	5.980	6.075	0.743	0.608	0.1003	0.9965	0.6741
180.0	14.410	14.490	14.450	11.800	11.570	11.685	1.445	1.169	0.1058	0.9961	1.3040
160.0	30.980	31.270	31.125	24.810	24.790	24.800	3.113	2.480	0.1131	0.9956	2.7888
140.0	62.700	63.570	63.135	50.520	50.930	50.725	6.314	5.073	0.1090	0.9959	5.6796
120.0	119.700	121.400	120.550	100.500	101.900	101.200	12.055	10.120	0.0873	0.9974	11.0779
115.0	126.740	128.520	127.630	108.950	110.330	109.640	12.763	10.964	0.0758	0.9980	11.8609
110.0	121.400	123.100	122.250	110.500	112.000	111.250	12.225	11.125	0.0471	0.9992	11.6868
100.0	68.100	69.100	68.600	70.400	71.200	70.800	6.860	7.080	-0.0158	0.9999	6.9818
80.0	13.400	13.500	13.450	14.000	14.200	14.100	1.345	1.410	-0.0236	0.9998	1.3797

density = 4.31 g/cm^3

Avg corr. Factor= 0.9986

Data for Batch #17 Sample 2, ref. page 117

Data for No B-field*

Temp (K)	mV1234 +	mV1234 -	mVavg1234	mV1324 +	mV1324 -	mVavg1324	R1234	R1324	X	Corr fact	ρ (Ω–cm)
295	1.15	0.98	1.065	1.25	1.08	1.165	0.107	0.117	-0.0448	0.9993	0.0909
280	1.41	1.28	1.345	1.57	1.48	1.525	0.135	0.153	-0.0627	0.9986	0.1169
260	2.04	1.93	1.985	2.26	2.18	2.220	0.199	0.222	-0.0559	0.9989	0.1714
240	3.09	3.02	3.055	3.50	3.49	3.495	0.306	0.350	-0.0672	0.9984	0.2668
220	5.13	5.17	5.150	5.95	5.97	5.960	0.515	0.596	-0.0729	0.9982	0.4524
200	9.28	9.25	9.265	10.76	10.81	10.785	0.927	1.079	-0.0758	0.9980	0.8163
180	18.38	18.48	18.430	21.62	21.90	21.760	1.843	2.176	-0.0829	0.9976	1.6357
160	41.56	41.86	41.710	49.31	49.83	49.570	4.171	4.957	-0.0861	0.9974	3.7143
140	102.93	103.83	103.380	123.52	124.86	124.190	10.338	12.419	-0.0914	0.9971	9.2571
130	165.50	166.60	166.050	198.60	200.90	199.750	16.605	19.975	-0.0921	0.9971	14.8794
125	168.40	169.90	169.150	201.10	203.20	202.150	16.915	20.215	-0.0889	0.9973	15.1062
120	113.50	115.00	114.250	132.50	135.10	133.800	11.425	13.380	-0.0788	0.9978	10.0978
100	14.20	14.40	14.300	16.90	17.00	16.950	1.430	1.695	-0.0848	0.9975	1.2717
80	4.50	4.50	4.500	5.30	5.30	5.300	0.450	0.530	-0.0816	0.9977	0.3989

*Data for With B-field on next page.

Data for Batch #17 Sample 2, ref. page 117

Data for With B-field

Temp (K)	mV1234 +	mV1234 -	mVavg1234	mV1324 +	mV1324 -	mVavg1324	R1234	R1324	X	Corr fact	ρ (Ω–cm)
295	1.19	1.03	1.110	1.34	1.19	1.265	0.111	0.127	-0.0653	0.9985	0.0967
280	1.48	1.35	1.415	1.69	1.52	1.605	0.142	0.161	-0.0629	0.9986	0.1230
260	2.09	1.99	2.040	2.38	2.32	2.350	0.204	0.235	-0.0706	0.9983	0.1788
240	3.23	3.14	3.185	3.66	3.59	3.625	0.319	0.363	-0.0646	0.9986	0.2774
220	5.25	5.22	5.235	6.00	5.97	5.985	0.524	0.599	-0.0668	0.9984	0.4570
200	9.51	9.45	9.480	10.82	10.84	10.830	0.948	1.083	-0.0665	0.9985	0.8273
180	18.76	18.61	18.685	21.42	21.48	21.450	1.869	2.145	-0.0689	0.9984	1.6347
160	40.20	40.40	40.300	46.50	46.90	46.700	4.030	4.670	-0.0736	0.9981	3.5426
140	83.50	84.40	83.950	97.90	99.20	98.550	8.395	9.855	-0.0800	0.9978	7.4288
135	98.10	99.10	98.600	114.50	116.10	115.300	9.860	11.530	-0.0781	0.9979	8.7079
130	107.80	108.90	108.350	125.90	127.50	126.700	10.835	12.670	-0.0781	0.9979	9.5689
125	103.90	105.10	104.500	118.70	120.40	119.550	10.450	11.955	-0.0672	0.9984	9.1262
100	19.00	19.10	19.050	19.40	19.70	19.550	1.905	1.955	-0.0130	0.9999	1.5747
80	5.40	5.50	5.450	5.70	5.80	5.750	0.545	0.575	-0.0268	0.9998	0.4568

thickness "h"= .180cm

diameter = 1.155 cm

mass =.8661g

density = 4.593 g/cm^3

Batch 17; Sample 2 (7% Fe)

Avg corr. Factor= 0.9983

Data for Batch #17 Sample 3, ref. page 118

Data for No B-field*

Temp (K)	mV1234 +	mV1234 -	mVavg1234	mV1324 +	mV1324 -	mVavg1324	R1234	R1324	X	Corr fact	ρ (Ω–cm)
295.0	1.880	1.690	1.785	1.630	1.460	1.545	0.179	0.155	0.0721	0.9982	0.1236
280.0	2.380	2.280	2.330	2.100	1.950	2.025	0.233	0.203	0.0700	0.9983	0.1616
260.0	3.480	3.410	3.445	3.060	2.980	3.020	0.345	0.302	0.0657	0.9985	0.2399
240.0	5.480	5.410	5.445	4.800	4.710	4.755	0.545	0.476	0.0676	0.9984	0.3785
220.0	9.180	9.160	9.170	8.030	7.990	8.010	0.917	0.801	0.0675	0.9984	0.6376
200.0	16.930	16.810	16.870	14.580	14.550	14.565	1.687	1.457	0.0733	0.9981	1.1663
180.0	34.430	34.660	34.545	29.960	30.020	29.990	3.455	2.999	0.0706	0.9983	2.3946
160.0	75.550	76.240	75.895	65.410	65.770	65.590	7.590	6.559	0.0728	0.9982	5.2493
140.0	210.500	214.200	212.350	185.200	186.300	185.750	21.235	18.575	0.0668	0.9985	14.7745
120.0	509.500	513.400	511.450	435.700	439.200	437.450	51.145	43.745	0.0780	0.9979	35.1963
115.0	570.100	574.500	572.300	484.300	488.300	486.300	57.230	48.630	0.0812	0.9977	39.2582
110.0	582.000	587.200	584.600	496.400	500.600	498.500	58.460	49.850	0.0795	0.9978	40.1707
105.0	496.100	502.500	499.300	427.700	433.200	430.450	49.930	43.045	0.0741	0.9981	34.4932
95.0	197.600	199.500	198.550	155.100	157.600	156.350	19.855	15.635	0.1189	0.9951	13.1268
80.0	45.200	45.400	45.300	37.400	37.800	37.600	4.530	3.760	0.0929	0.9970	3.0722

*Data for With B-field on next page.

Data for Batch #17 Sample 3, ref. page 118

Data for With B-field

Temp (K)	mV1234 +	mV1234 -	mVavg1234	mV1324 +	mV1324 -	mVavg1324	R1234	R1324	X	Corr fact	ρ (Ω–cm)
295.0	1.880	1.680	1.780	1.670	1.480	1.575	0.178	0.158	0.0611	0.9987	0.1245
260.0	3.330	3.360	3.345	2.860	2.840	2.850	0.335	0.285	0.0799	0.9978	0.2298
220.0	8.390	8.830	8.610	7.150	7.540	7.345	0.861	0.735	0.0793	0.9978	0.5918
180.0	30.500	31.300	30.900	26.000	26.500	26.250	3.090	2.625	0.0814	0.9977	2.1194
160.0	61.100	62.300	61.700	51.800	52.700	52.250	6.170	5.225	0.0829	0.9976	4.2254
140.0	136.300	138.500	137.400	115.500	117.500	116.500	13.740	11.650	0.0823	0.9976	9.4153
120.0	301.500	305.100	303.300	257.200	259.900	258.550	30.330	25.855	0.0796	0.9978	20.8381
115.0	354.800	359.100	356.950	303.500	306.400	304.950	35.695	30.495	0.0786	0.9979	24.5502
110.0	386.300	390.100	388.200	335.700	339.100	337.400	38.820	33.740	0.0700	0.9983	26.9248
105.0	368.200	372.400	370.300	329.100	332.800	330.950	37.030	33.095	0.0561	0.9989	26.0371
95.0	208.200	211.300	209.750	186.100	188.200	187.150	20.975	18.715	0.0569	0.9989	14.7362

thickness "h"= .164cm

diameter = 1.19cm

mass = .8329g

density = 4.566 g/cm^3

Batch 17; Sample 3 (7% Fe)

Average corr. Factor= 0.9981

Data for Batch #17 Sample 4, ref. page 118

Data for No B-field*

Temp (K)	mV1234 +	mV1234 -	mVavg1234	mV1324 +	mV1324 -	mVavg1324	R1234	R1324	X	Corr fact	ρ (Ω–cm)
295.0	1.85	1.65	1.750	1.65	1.49	1.570	0.175	0.157	0.0542	0.9990	0.1270
260.0	3.35	3.25	3.300	3.22	3.09	3.155	0.330	0.316	0.0225	0.9998	0.2472
220.0	8.87	8.75	8.810	8.58	8.52	8.550	0.881	0.855	0.0150	0.9999	0.6649
180.0	33.60	33.60	33.600	32.20	32.50	32.350	3.360	3.235	0.0190	0.9999	2.5258
160.0	77.20	77.80	77.500	73.70	74.40	74.050	7.750	7.405	0.0228	0.9998	5.8038
140.0	209.80	211.00	210.400	197.90	199.20	198.550	21.040	19.855	0.0290	0.9997	15.6596
135.0	264.50	266.10	265.300	249.60	251.30	250.450	26.530	25.045	0.0288	0.9997	19.7493
130.0	322.90	324.80	323.850	304.50	306.60	305.550	32.385	30.555	0.0291	0.9997	24.1011
127.0	337.10	339.20	338.150	321.20	323.70	322.450	33.815	32.245	0.0238	0.9998	25.2983
125.0	328.70	330.70	329.700	317.40	319.70	318.550	32.970	31.855	0.0172	0.9999	24.8276
120.0	235.20	236.70	235.950	238.70	239.30	239.000	23.595	23.900	-0.0064	1.0000	18.1919
115.0	137.50	138.50	138.000	141.40	143.40	142.400	13.800	14.240	-0.0157	0.9999	10.7394
100.0	36.30	36.50	36.400	36.40	36.50	36.450	3.640	3.645	-0.0007	1.0000	2.7904
95.0	25.70	25.90	25.800	25.50	25.70	25.600	2.580	2.560	0.0039	1.0000	1.9688

*Data for With B-field on next page.

Data for Batch #17 Sample 4, ref. page 118

Data for With B-field

Temp (K)	mV1234 +	mV1234 -	mVavg1234	mV1324 +	mV1324 -	mVavg1324	R1234	R1324	X	Corr fact	ρ (Ω-cm)
295.0	1.85	1.70	1.775	1.59	1.45	1.520	0.178	0.152	0.0774	0.9979	0.1259
260.0	3.25	3.35	3.300	2.98	3.03	3.005	0.330	0.301	0.0468	0.9992	0.2413
220.0	8.30	9.03	8.665	7.55	8.18	7.865	0.867	0.787	0.0484	0.9992	0.6326
180.0	30.60	32.30	31.450	27.80	29.20	28.500	3.145	2.850	0.0492	0.9992	2.2944
160.0	65.60	67.60	66.600	59.20	61.20	60.200	6.660	6.020	0.0505	0.9991	4.8526
140.0	147.10	150.10	148.600	135.40	138.50	136.950	14.860	13.695	0.0408	0.9994	10.9312
135.0	169.70	172.90	171.300	159.20	162.60	160.900	17.130	16.090	0.0313	0.9997	12.7201
130.0	198.80	202.30	200.550	187.10	190.60	188.850	20.055	18.885	0.0300	0.9997	14.9107
127.0	208.80	212.80	210.800	197.20	200.80	199.000	21.080	19.900	0.0288	0.9997	15.6922
125.0	209.80	213.60	211.700	198.00	201.90	199.950	21.170	19.995	0.0285	0.9997	15.7631
120.0	186.90	190.50	188.700	177.20	180.40	178.800	18.870	17.880	0.0269	0.9997	14.0730
115.0	144.40	147.00	145.700	136.30	137.90	137.100	14.570	13.710	0.0304	0.9997	10.8287
100.0	51.00	53.30	52.150	48.50	49.20	48.850	5.215	4.885	0.0327	0.9996	3.8672
95.0	33.60	34.30	33.950	31.00	31.30	31.150	3.395	3.115	0.0430	0.9994	2.4920

thickness "h"= .169cm

diameter = 1.19cm

mass = .8523g

density = 4.534 g/cm^3

Batch 17; Sample 4 (7% Fe)

Average corr. Factor= 0.9996

Data for Batch #17 Sample 5, ref. page 119

Data for No B-field*

Temp (K)	mV1234 +	mV1234 -	mVavg1234	mV1324 +	mV1324 -	mVavg1324	R1234	R1324	X	Corr fact	ρ (Ω–cm)
295.0	1.67	1.48	1.575	1.75	1.53	1.640	0.158	0.164	-0.0202	0.9999	0.1217
220.0	8.27	8.19	8.230	8.46	8.38	8.420	0.823	0.842	-0.0114	1.0000	0.6302
180.0	31.40	31.40	31.400	31.30	31.40	31.350	3.140	3.135	0.0008	1.0000	2.3751
160.0	74.80	75.00	74.900	72.10	72.60	72.350	7.490	7.235	0.0173	0.9999	5.5728
140.0	202.00	202.10	202.050	186.90	188.50	187.700	20.205	18.770	0.0368	0.9995	14.7451
130.0	335.20	335.50	335.350	303.90	306.20	305.050	33.535	30.505	0.0473	0.9992	24.2204
125.0	415.70	416.30	416.000	372.40	375.90	374.150	41.600	37.415	0.0530	0.9990	29.8782
120.0	481.00	483.10	482.050	430.70	435.60	433.150	48.205	43.315	0.0534	0.9990	34.6061
115.0	542.00	544.00	543.000	479.70	485.10	482.400	54.300	48.240	0.0591	0.9988	38.7645
110.0	556.60	559.10	557.850	484.30	489.90	487.100	55.785	48.710	0.0677	0.9984	39.4886
105.0	476.30	479.40	477.850	405.20	410.40	407.800	47.785	40.780	0.0791	0.9978	33.4491
100.0	306.70	308.20	307.450	257.60	261.20	259.400	30.745	25.940	0.0848	0.9975	21.4018
90.0	89.40	89.60	89.500	81.60	82.40	82.000	8.950	8.200	0.0437	0.9993	6.4870

*Data for With B-field on next page.

Data for Batch #17 Sample 5, ref. page 119

Data for With B-field

Temp (K)	mV1234 +	mV1234 -	mVavg1234	mV1324 +	mV1324 -	mVavg1324	R1234	R1324	X	Corr fact	ρ (Ω–cm)
295.0	1.73	1.56	1.645	1.68	1.54	1.610	0.165	0.161	0.0108	1.0000	0.1232
220.0	7.75	8.13	7.940	7.60	7.87	7.735	0.794	0.774	0.0131	0.9999	0.5933
180.0	28.80	29.60	29.200	27.20	28.00	27.600	2.920	2.760	0.0282	0.9997	2.1493
160.0	64.50	65.70	65.100	59.50	60.60	60.050	6.510	6.005	0.0404	0.9994	4.7343
140.0	136.00	137.70	136.850	122.80	124.40	123.600	13.685	12.360	0.0509	0.9991	9.8492
130.0	202.70	204.90	203.800	180.20	182.30	181.250	20.380	18.125	0.0586	0.9988	14.5568
125.0	251.50	254.30	252.900	222.20	224.50	223.350	25.290	22.335	0.0620	0.9987	18.0020
120.0	307.30	311.10	309.200	268.10	271.50	269.800	30.920	26.980	0.0680	0.9984	21.8800
115.0	366.30	369.80	368.050	319.30	323.10	321.200	36.805	32.120	0.0680	0.9984	26.0464
110.0	384.10	388.40	386.250	335.90	341.10	338.500	38.625	33.850	0.0659	0.9985	27.3906
105.0	344.10	347.50	345.800	303.40	308.60	306.000	34.580	30.600	0.0611	0.9987	24.6388
100.0	253.40	255.50	254.450	222.20	225.70	223.950	25.445	22.395	0.0638	0.9986	18.0820
90.0	101.00	102.00	101.500	89.70	91.10	90.400	10.150	9.040	0.0578	0.9988	7.2550

thickness "h"= .167cm

diameter = 1.197cm

density = 4.636 g/cm^3

Avg corr. Factor= 0.9992

mass = .8711g

Batch 17; Sample 5 (7% Fe)

Data for Batch #17 Sample 6, ref. page 119

Data for No B-field*

Temp (K)	mV1234 +	mV1234 -	mVavg1234	mV1324 +	mV1324 -	mVavg1324	R1234	R1324	X	Corr. Fact.	ρ (Ω–cm)
200.0	13.50	13.40	13.450	12.40	12.20	12.300	1.345	1.230	0.0447	0.9993	0.9740
180.0	27.20	27.20	27.200	24.30	24.10	24.200	2.720	2.420	0.0584	0.9988	1.9432
160.0	58.60	58.90	58.750	51.30	51.40	51.350	5.875	5.135	0.0672	0.9984	4.1608
140.0	147.10	147.80	147.450	126.00	126.80	126.400	14.745	12.640	0.0769	0.9979	10.3440
130.0	242.40	244.10	243.250	209.30	211.30	210.300	24.325	21.030	0.0726	0.9982	17.1355
125.0	267.10	269.60	268.350	234.20	237.10	235.650	26.835	23.565	0.0649	0.9985	19.0486
120.0	225.70	227.50	226.600	206.30	208.60	207.450	22.660	20.745	0.0441	0.9993	16.4178
110.0	74.60	75.30	74.950	68.90	69.80	69.350	7.495	6.935	0.0388	0.9995	5.4589
100.0	29.40	29.60	29.500	26.20	26.30	26.250	2.950	2.625	0.0583	0.9988	2.1077
90.0	15.00	15.10	15.050	13.20	13.20	13.200	1.505	1.320	0.0655	0.9985	1.0677

*Data for With B-field on next page.

Data for Batch #17 Sample 6, ref. page 119

Data for With B-field

Temp (K)	mV1234 +	mV1234 -	mVavg1234	mV1324 +	mV1324 -	mVavg1324	R1234	R1324	X	Corr fact	ρ (Ω–cm)
200.0	13.10	12.20	12.650	10.90	9.90	10.400	1.265	1.040	0.0976	0.9967	0.8696
180.0	25.10	24.20	24.650	21.00	20.00	20.500	2.465	2.050	0.0919	0.9971	1.7039
160.0	51.80	50.80	51.300	44.00	42.80	43.400	5.130	4.340	0.0834	0.9976	3.5757
140.0	105.30	104.80	105.050	91.80	90.50	91.150	10.505	9.115	0.0708	0.9983	7.4133
130.0	144.50	144.20	144.350	126.80	126.10	126.450	14.435	12.645	0.0661	0.9985	10.2343
125.0	160.80	161.60	161.200	143.80	144.40	144.100	16.120	14.410	0.0560	0.9989	11.5431
120.0	145.60	146.60	146.100	131.80	132.70	132.250	14.610	13.225	0.0498	0.9991	10.5265
110.0	85.20	85.70	85.450	78.20	78.50	78.350	8.545	7.835	0.0433	0.9993	6.1958
100.0	37.60	37.90	37.750	34.30	34.30	34.300	3.775	3.430	0.0479	0.9992	2.7249
90.0	21.30	21.50	21.400	19.50	19.40	19.450	2.140	1.945	0.0477	0.9992	1.5450

thickness "h"= .158cm

diameter = 1.193cm

mass = .8731g

density = 4.636 g/cm^3

Batch 17; Sample 6 (7% Fe)

Average corr. Factor= 0.9985